Version of Record: https://www.sciencedirect.com/science/article/pii/S0967064518300730
Manuscript_4429093893c93bfa5433a25e25cf813c

Modeled spatial-temporal distribution of productivity, chlorophyll, iron and nitrate on the northern Gulf of Alaska shelf relative to field observations

K. O. Coyle[a,*], A. J. Hermann[b,c], R. R. Hopcroft[a]

[a]*College of Fisheries and Ocean Sciences, University of Alaska Fairbanks, Fairbanks, AK 99775-7220, USA*

[b]*Joint Institute for the Study of the Atmosphere and Ocean, University of Washington, Seattle, WA 98195, USA*

[c]*Ocean Environment Research Division, NOAA/PMEL, Seattle, WA 98115, USA*

Abstract

The northern Gulf of Alaska (GOA) shelf is dynamic spatially and temporally. With two major current systems and numerous eddies and meanders, interpretation of field data from ship-based observations at specific times and locations is complicated. We used the Regional Ocean Modeling System (ROMS) with an embedded nutrient-phytoplankton-zooplankton (GOANPZ) model to aid in understanding spatial-temporal patterns of productivity, chlorophyll concentration and biomass over the GOA shelf between 132°W and 160°W from 2000 - 2013. Carbon chlorophyll ratios in the model were varied in response to light to alter production-irradiance curves by season to conform to field measurements. Simulations reveal regions of high productivity in March-May on the southeast Alaskan Shelf, and the western inner shelf between Prince William Sound (PWS) and the Shumagin Islands, but with lower productivity on the outer shelf between PWS and western Kodiak. The model produced regions of elevated productivity on the outer shelf of the western GOA during summer and fall. This pattern is driven by circulation affecting the distribution of iron on the western shelf. Simulated productivity on the shelf between 2000 and 2006 was elevated relative to 2007-2013, apparently due to changes in the simulated iron concentration. Correlations indicate that simulated production on the western GOA shelf during March-May can explain up to 65% of the variance in the mean biomass of large copepods from net tows during spring. Simulations suggest that detailed temporal-spatial data on iron concentration and the processes affecting iron are crucial to understanding interannual spatial-temporal differences in magnitudes of production and biomass at lower trophic levels on the GOA shelf.

Keywords: Gulf of Alaska, Modeling, Production, Iron, Chlorophyll, Zooplankton

*Corresponding author.

E-mail address: kocoyle@alaska.edu (K.O. Coyle)

1. Introduction

The Gulf of Alaska (GOA) includes about 13% of the United States continental shelf and supports some of the largest fisheries in the US. The high production required to sustain these fisheries seems paradoxical due to the strong persistent downwelling conditions and the nitrate-poor coastal freshwater discharge (Weingartner et al., 2002). The GOA is dominated by two major current systems: the Alaska Coastal Current, which runs westward along the coast and is characterized by low salinity due to freshwater runoff (Stabeno et al., 2004; Royer et al., 1988), and the Alaska Current-Alaskan Stream, a cyclonic boundary current at the shelf break (Reed, 1984). These current systems generate eddies and meanders that mix high nitrate-low chlorophyll iron-depleted (HNLC) oceanic water with nitrate-depleted iron-rich coastal water, resulting in localized patches of high productivity (Stabeno et al., 2004). Since these physical features are always in motion and shipboard observations are primarily point samples in space and time, interpretation of field observations to spatial scales of the whole shelf in timeframes of seasons, years and decades is complicated. Nevertheless, estimates of production are essential to data-driven fisheries management, to ensure that total biomass removal does not exceed system production, which could degrade ecosystem resilience, potentially resulting in irreversible changes (Pikitch et al., 2004).

Although the productivity on the GOA shelf is assumed to be high, annual estimates are primarily limited to extrapolation of discrete ship measurements to an entire year (Sambroto and Lorenzen, 1986). While satellite estimates are spatially broad, persistent cloud cover can result in missing data for periods of 1 to 10 weeks (Waite and Mueter, 2013). In addition, the depth penetration of the satellite measurements is probably about 10 m (Waite and Mueter, 2013), so it does not detect the deep chlorophyll maximum typically located at about 15-25 m depth (Strom et al., 2006). We therefore developed a nutrient-phytoplankton-zooplankton numerical model (GOANPZ) embedded in the Regional Ocean Modeling System (ROMS) circulation model (Hinkley et al., 2009; Coyle et al., 2012, 2013) to provide a formal mathematical tool as an additional aid in interpreting field measurements on a spatial scale of the whole shelf at time scales of years to decades. The GOANPZ is simplified to include only those state variables that are essential to simulating productivity on the GOA shelf (Coyle et al., 2012), so that the model studies could be done with the computer resources available to the project. Here we present a summary of the results of model runs from 2000 to 2013 as part of the Gulf of Alaska Integrated Ecosystem Research Program (GOAIERP; Dickson and Baker, 2016), highlight the broad-scale geographic, seasonal and annual production on the GOA shelf, and relate the production to copepod biomass measured on the Seward Line, a long-term sampling transect running from the mouth of Resurrection Bay across the shelf and into the Alaskan Stream (Fig. 1C). A movie of important state variables for 2000-2013 can be accessed with the following links: https://nga.lternet.edu/research/ or on YouTube at https://www.youtube.com/watch?v=rPfOfbt8u-A.

2. Materials and methods

2.1. Environmental Description

The simulations covered the northern GOA from southeast Alaska in the east to the Shumagin Islands in the west, a distance of roughly 2780 km. The shelf width varies from a few kilometers to over 200 km, with a rugged topography characterized by numerous fjords, inlets and submarine canyons. The GOA has two major current systems, the Alaskan Stream, which flows westward at or near the shelf break (Reed, 1984; Stabeno et al., 2004), and the Alaska Coastal Current (ACC), a low-salinity current flowing westward within 20-30 km of shore (Royer, 1998; Weingartner et al., 2005). Wind is the primary forcer of the ACC (Stabeno et al., 2004). Fresh water discharge is a major source of iron to the coastal GOA (Lippiatt et al., 2010). The GOA is characterized by two major phytoplankton communities, the coastal community with intense spring diatom blooms and nitrate limitation during summer (Strom et al., 2006), and an oceanic community that is iron limited (Martin et al., 1989) and consists primarily of small flagellates (Strom et al., 2006). The currents generate eddies and meanders that mix the two communities to varying degrees, causing substantial spatial and temporal variations in the phytoplankton composition. The 3-km grid used in the ROMS model provides sufficient resolution to capture much of the variability imposed by these physical oceanographic features. Persistent downwelling favorable winds during winter and spring promote transport of high-nitrate low-iron oceanic water in the Ekman layer onto the shelf, confining much of the freshwater discharge to the coastal zone and the ACC (Stabeno et al., 2004). Oceanic zooplankton species in the Ekman layer are transported shoreward; oceanic species that are most abundant below the Ekman layer tend to dominate populations on the outer shelf and in oceanic regimes but are minor constituents of populations in the near-shore environment (Coyle and Pinchuk, 2005).

2.2. Physical model

ROMS is a terrain-following (s-coordinate), finite difference (Arakawa C-grid) model with high-order, weakly dissipative algorithms for tracer advection and unified treatment of surface and bottom boundary layers, based on the Large *et al.* (1994) and Styles and Glenn (2002) (bottom boundary layer) algorithms. Numerical details can be found in Haidvogel et al. (2000), Moore *et al*. (2004) and Shchepetkin and McWilliams (2004), and on the ROMS web site.

The hydrodynamic model is based on ROMS version 3 (Shchepetkin and McWilliams, 2004; Haidvogel *et al*., 2008). The model was run using two domains: a 3-km resolution grid of the CGOA (Coastal Gulf of Alaska), embedded within an 11-km resolution grid of the Northeast Pacific (NEP) (Fig. 1A). The CGOA grid encompasses the eastern, central and western Gulf of Alaska; it extends from Haida Gwaii in British Columbia to the Shumagin Islands off the Alaska Peninsula, from the coast to approximately 1200 km offshore, with 482 x 482 grid points. The NEP domain stretches from Baja California to the Chukchi Sea, from the coast to approximately

2000 km offshore, with 226 x 642 grid points. The time step for the CGOA grid had to be reduced to 100 seconds to maintain numerical stability of the physical model for the 2000-2013 model run. Fine-scale bathymetry is based on ETOPO5 and supplementary data as described in Danielson et al. (2016); smoothing of bathymetry was applied for numerical stability. Both model domains utilized 42 vertical layers, with refinement for tighter spacing to resolve the surface boundary layer. Any regions shallower than 10 m were set to 10 m deep. Vertical mixing is based on the algorithms of Large et al. (1994). Tidal dynamics are included in the CGOA model (Egbert et al., 1994; Egbert and Erofeeva, 2002); the explicit inclusion of tidal flows allows tidally-generated mixing and tidal residual flows to develop.

Surface forcing for outer (NEP) and inner (CGOA) model runs came from 6-hourly atmospheric output from NOAA's CFSR (Climate Forecast System Reanalysis) climate products (Saha et al. 2012) and NEP initial and boundary conditions were generated from CFSR monthly oceanic reanalysis output spanning 1995 to 2013. Horizontal resolution of the CFSR ocean model is ~ 40 km. CGOA boundary conditions were interpolated from our NEP output, which has ~10 km resolution (one-way nesting from outer to inner grids). Bulk forcing, based on the algorithms of Large and Yeager (2008), were used to relate the 6-hourly CFSR variables (wind velocities, air temperature, rainfall rate, absolute humidity, downward shortwave and longwave radiation) to surface stress and the net transfers of sensible heat, latent heat, shortwave and longwave radiation through the sea surface, as well as surface freshening by rainfall.

2.2.1. Runoff

Freshwater runoff was applied to the northern Gulf of Alaska simulations by freshening surface salinity within a few grid points of the coastline using an exponential taper based on squared distance from the coastline, with an e-folding distance of ~30 km. The above technique minimized the runaway stratification artifact, which has been observed using continuous horizontal input of freshwater along broad stretches of the coastline (Dobbins et al., 2009; Vaz and Simpson, 1994). The alongshore spatial pattern of the runoff for the NEP grid for 1995 – 2007 was obtained from Dai et al. (2009). After 2007 a climatology based on Dai et al. (2009) was used to set the NEP grid runoff. Runoff for the CGOA grid was generated by a high-resolution freshwater discharge model for the Gulf of Alaska (Hill et al., 2015; Beamer et al., 2016). The high-resolution model generated daily estimates of runoff along the coastline for all major drainage basins between the British Columbia-Alaskan boundary and the west end of Kodiak Island (Fig. 2). The coastal runoff was mapped to the nearest coastal grid point and introduced as outlined above. Freshwater between the west end of Kodiak and the Shumagin Islands was introduced by averaging runoff each day in Shelikof Strait, mapping the resulting mean to each coastal grid point west of Kodiak and freshening the salinity as described above.

2.3. Biological model

The biological model was designed to capture the major dynamics of the ecosystem in the northern GOA, while minimizing complexity, which increases the number of parameters, computational requirements and output storage requirements (Hinckley et al., 2009). The large and small phytoplankton cell components (Fig. 1B) differ in their tolerance to iron limitation, growth rate and nutrient uptake rates. The large cell and small cell components also differ in predation losses. Small cells are consumed primarily by large and small microzooplankton, secondarily by small and large copepods. In contrast, large cells are consumed by large microzooplankton, small copepods, large copepods and euphausiids equally. The large and small microzooplankton differ primarily by predation losses. The small microzooplankton are consumed primarily by the large microzooplankton and secondarily by the small and large copepods, while the large microzooplankton are consumed by small and large copepods and euphausiids equally. The large and small copepods consume mostly the large phytoplankton and microzooplankton, and secondarily the small microzooplankton. Euphausiids consume the large phytoplankton and large microzooplankton equally, but also take small amounts of copepods. These feeding preferences are set in the parameter list (Appendix Table 2). The large copepods (*Neocalanus*) differ from the small copepods primarily by their vertical migration behavior. At the start of each year of simulations (January), the large copepods occur at 500-1000 m depth, migrate to the surface in January-February, reside in the surface through mid-June, after which they descend to over-wintering depths at 500-1000 m. This behavior simulates the ontogenetic migration behavior of the *Neocalanus* species (Tsuda et al., 1999; Kobari and Ikeda, 2001a, 2001b, Mackas and Tsuda, 1999). The small copepod component remains in the upper mixed layer for the entire simulation. The large and small phytoplankton can consume nitrate and ammonium but nitrate uptake and growth is severely limited by iron concentrations, particularly in the large phytoplankton. This restriction essentially constrains the large phytoplankton community to the shelf. Current setting for model parameters and GOANPZ model equations are listed in appendix Tables 1 and 2.

2.3.1. Initial conditions

Initial conditions for the GOANPZ were generated using a series of algorithms to provide values of carbon biomass of state variables similar to GLOBEC (Global Ocean Ecosystem Dynamics program, Weingartner et al., 2002) field observations in March (Coyle et al., 2012). Nitrate concentrations were set at 15 μM above 50 m depth and gradually increased to about 45 μM below 500 m, and ammonium was set close to zero. Initial conditions for the phytoplankton and zooplankton were set to observations of carbon biomass in April and March respectively. Phytoplankton concentrations were set at 20 mg C m^{-3}, microzooplankton concentrations were set at 10 mg C m^{-3}, and copepod concentrations were 25 mg C m^{-3} above 50 m depth and all were close to 0 below 50 m depth. Offshore iron concentration was initially set to 0.05 nM in the upper 100 m and 0.6 nM below 100 m, with a transition from oceanic to shelf values occurring between the 1500 and 200 m isobaths, and shelf concentrations of 2 nM (Martin et al., 1989). The system was allowed to evolve during 3D simulations without nudging the iron

concentration back to a climatological mean, but iron was added at a rate of 0.36 X 10^2 nM per kg of freshwater discharge per second at each location where fresh water was added along the coast. Addition of iron with freshwater at the above rate resulted in iron concentrations approximately equal to the dissolved iron concentrations reported by Wu et al. (2009) at Station GAK1 for May and July. The CGOA run was started in January 1996 and run through 2013; 1996-1999 were spin-up years.

2.3.2. Photosynthetically available radiation (PAR)

Comparisons of PAR computed from shortwave radiation and measured from ship-mounted PAR sensors indicated that the shortwave radiation from the CSFR files was not reproducing the magnitude of daily changes in PAR amplitude due to clouds. We therefore used daily averaged measurements of PAR from the SeaWiFS satellite for 1998 through 2004, and the MODIS satellite for 2005 - 2013, which have daily amplitudes similar to ship-board measurements. The satellite PAR data was downloaded, regridded and converted to NetCDF (Network Common Data Form) as outlined in Coyle et al. (2012).

2.3.3. Phytoplankton component

The photosynthetic efficiency (α) in the original model (Coyle et al., 2012) was based on values measured along the Seward Line in July (Strom et al., 2010), 2.1 and 5.6 mg C (mg Chl)$^{-1}$(E m^{-2})$^{-1}$. Subsequent field measurements in April-May revealed marked differences in α, apparently due to lower PAR values in spring (Strom et al., 2016). The model was therefore modified as follows to alter α relative to light levels by altering the C-Chl ratios in response to light as outlined in Geider et al. (1997). This modification altered the response of phytoplankton to light levels, requiring us to raise the extinction coefficient k_{ex} and k_{chl} from 0.035 to 0.08 and 0.045 to avoid unrealistically high chlorophyll concentrations below the pycnocline (Coyle et al., 2012). The extinction coefficients due to phytoplankton (k_{chl}) were computed for each depth according to Morel (1988).

2.3.3.1. Carbon chlorophyll ratios

The ratio of chlorophyll *a* to carbon (Chl-C) was defined as

$$\theta = \frac{\theta_m}{1+\left(\frac{\theta_m \alpha^{chl} I}{2P_m^C}\right)} = \frac{\theta_m}{1+\left(\frac{I}{2K_I}\right)} \text{ where } K_I = \frac{P_m^C}{\alpha^{chl}\theta_m} = \text{the irradiance at which growth is light}$$

saturated; I is the incident radiation (E m^{-2} d^{-1}), P_m^C is the light-saturated rate of photosynthesis normalized to carbon (s^{-1}), α^{chl} is the initial slope of the PI curve normalized to chlorophyll *a* (mg C (mg Chl)$^{-1}$ (E m^{-2})$^{-1}$) and θ_m is the maximum Chl-C ratio as defined by Geider et al., (1997).

Since the large phytoplankton component in the model represents primarily diatoms, we computed α^{chl} from values of P_m^C, θ_m and K_I for diatoms from Gieder et al. (1997, see their Table 2). However, if all of Gieder's diatom values are averaged, the minimum C-Chl ratio is 40 that is about twice the minimum values from field measurements (Coyle et al., 2012). We therefore computed the α^{chl} value using measurements of K_I, P_m^C and θ_m from the highest five θ_m values in Geider's Table 2. P_m^C, α^{chl} and θ_m for the small phytoplankton component were computed as the mean of values for Chrysophyceae, Cyanophyceae, *Gyrodinium aureolum* and Prymnesiophyceae in Geider et al. (1997, see their Table 2) and resulted in C-Chl ratios roughly within the range of field measurements during summer (Coyle et al, 2012). This technique resulted in minimum and maximum mean C-Chl ratios of 19 to 45 and 45 to 97 for the large and small phytoplankton components respectively, in the upper 25 m for the period from March through October. Parameters used in the model are listed in Table 1.

The effect of light limitation on the photosynthetic rate was a modification of the hyperbolic tangent function (Jassby and Platt, 1976): $Light_{Lim} = \left(\tanh\left(\frac{\alpha' PAR}{P_{\max}} \right) \right)$, where $\alpha' = \frac{\alpha}{\theta}$, θ is the Chl-C ratio as defined by Geider et al (1997) and P_{max} is the maximum carbon specific photosynthetic rate.

Application of Geider's equations can generate photosynthesis-irradiance curves (Fig. 3B) that are similar to those for the GOA (Fig. 3A) (Strom et al., 2016). The upper axis (Fig. 3B) shows the approximate model equivalent light intensity per day. Light modifies the slope of the curve and nutrient limitation sets the magnitude of P_{max}, the maximum photosynthetic rate at a given nutrient concentration in space and time in the simulations. The data reported in Strom et al. (2016) had a broad range (1.28 to 21.75 µg C (µg Chl^{-1}) hr^{-1})), suggesting that the resulting curves are representative, not fixed relationships. The left side of the plot with light levels from 0-30 E m^{-2} d^{-1} (equivalent to ~350 µmol m^{-2} s^{-1}) is the portion of the curves relevant to the GOA during spring. The photo-inhibition expressed by the right side of the curve is probably rarely experienced by phytoplankton on the GOA shelf during spring (Strom, personal communication). Note that the model computes the C-Chl ratio for each time step for each depth interval and outputs an average for each day. Phytoplankton in the ocean are probably responding to the average light intensity they experience as they are advected within the euphotic zone.

2.3.3.2. Nutrient limitation

Nitrate limitation was computed using a Michalis-Menton relationship with a term for ammonium suppression $NO_3^{\lim} = \left(\frac{[NO_3]\exp(-\psi[NH_4]}{d_1 + [NO_3]} \right)$ where ψ is a coefficient for ammonium suppression of nitrate uptake and $d_{1(PS \text{ or } PL)}$ is the nitrate half saturation constant for small and

large phytoplankton respectively. Iron limitation is also a Michalis-Menton expression $Fe_{\lim} = \left(\frac{[\mathrm{Fe}]}{d_{fePS;PL} + [\mathrm{Fe}]} \right) \left(\frac{d_{fePS;PL} + 2}{2} \right)$ where $d_{fePS;PL}$ is the half saturation constant for iron uptake for small and large phytoplankton and the model code changes any number for Fe_{lim} above 1 to 1. The nitrate uptake differs from that in Coyle et al. (2012, 2013) in that the nitrate uptake is the minimum of light limitation or nitrate limitation modified by iron limitation rather than the product of the three: $NO_3^{Uptake} = \min(NO_3^{\lim} Fe_{\lim}, Light^{\lim})$. The ammonium uptake is also the minimum of light limitation or ammonium limitation but ammonium uptake in these simulations is not iron limited. Nitrate in the simulations is not introduced with freshwater.

The use of the minimum option permitted us to lower the growth rate parameter for large and small phytoplankton (*DiL*, *DiS*) from 1.6 for both to 1.55 and 0.849 for large and small phytoplankton, respectively. The ability of the simulated large phytoplankton component to generate a spring bloom and exhaust nitrate from coastal surface waters as field observations indicate (Strom et al., 2006), is sensitive to the growth rate parameters.

2.3.4. Zooplankton component

The zooplankton model components were essentially unchanged from Coyle et al. (2013). Simulated zooplankton growth was governed by a six-term equation involving assimilation efficiency, the maximum specific ingestion rate, a temperature correction and feeding preferences, decremented by respiration, excretion and mortality, which is a closure term. The mortality parameters were adjusted to produce zooplankton concentrations approximately equal to values measured by coarse and fine mesh zooplankton collections during GLOBEC (Coyle and Pinchuk, 2003, 2005). Zooplankton were collected and analyzed as outlined in Section 2.6.

2.4. Model validations

Validation studies and descriptions of related versions of the NEP model are available in Danielson et al. (2011) and Hermann et al. (2009a); validation studies and descriptions of related versions of the CGOA model can be found in Hermann et al. (2009b), Hinckley et al. (2009), Dobbins et al. (2009), and Coyle et al. (2012, 2013). The above studies demonstrated that the model generates a good representation of the main circulation and spatial-temporal patterns.

2.5. Analysis methods

Model output was characterized by season and location by computing mean values for model variables within analysis polygons (Fig. 2). Polygon 1 (P1) covered the entire western shelf from the coast to the shelf break and from the western grid boundary east to 147° W (PWS). Polygon 2 (P2) characterized conditions off shore of the shelf south of P1. Polygons 4 and 5 (P4, P5) covered the coast from the Canadian boundary west to 147° W, on and off the

shelf respectively. Polygon 7 (P7) covers that region of P1 with simulated low iron concentration from west of Kodiak east to 145°W, and from the shelf break to the Kenai Peninsula.

The mean simulated primary production in the upper 30 m, mean concentrations of iron and nitrate in the upper 25 m, the mean s-coordinate (~vertical) momentum flux (omega) in the upper 100 m, the mean PAR, and the mean simulated copepod biomass in the upper 25 m for P1 – 7 and the mean runoff for P1, P7 and P4 were computed for each season and year. One hundred meters is the depth of the permanent halocline, 25 m is the maximum depth of the seasonal pycnocline, and 30 m is the integration depth of GLOBEC primary production data. Multiple regression was used to characterize the variables that influenced production and iron concentration in spring and fall. Since iron concentration in the coastal regions of P1 and P4 is supersaturated relative to phytoplankton uptake in summer and fall, the mean iron concentration inside the polygons may not be the best representation of iron availability for phytoplankton. Therefore, the fraction of the polygon area with iron concentration above 0.75 nM was computed for shelf polygons (P1, P4 and P7); the fraction with iron concentration above 0.5 nM was computed for basin polygons (P2 and P5). The iron concentrations were selected to generate representative fractions of the mean polygon areas; use of 0.75 nM for basin polygons resulted in a zero fraction for the most days of simulation so the iron concentration boundary was lowered to 0.5 nM. These fractions are referred to as the "iron area". The adjusted R^2 (R_a^2) in the multiple regression tables adjusts the R^2 for the number of predictors; it increases if the added predictor improves the prediction by more than would be expected by chance and decreases if the predictor increases the prediction by less than would be expected by chance. The variables used in the regression analysis included the average values for the polygons during the specified season: primary production in the upper 30 m (g C m^{-2}), runoff in coastal polygons (kg s^{-1} m^{-2} X 10^{-4}), the mean s-coordinate (~vertical) momentum in the upper 100 m (omega, m^3 s^{-1}), nitrate concentration (μM), and PAR (E m^{-2} d^{-1}). Additional flux variables computed for Polygon 7 included: horizontal flux of water across the outer boundary of the polygon (m^3 s^{-1}), horizontal flux of nitrate and iron in the upper 25 m across the outer polygon boundary (μM s^{-1}), vertical advective and diffusive flux of nitrate and iron into the upper 25 m (μM s^{-1}). The vertical velocities (w) used to calculate the vertical advective fluxes were derived from the divergence of the stored horizontal velocities; these are in fact very strongly correlated with the stored sigma-coordinate velocities (omega) on the CGOA shelf.

2.6. Observational zooplankton data

Simulated production in P7 was also compared with net sampled copepod biomass along the Seward Line during spring and fall. Zooplankton were collected during May and August-October along the Seward Line (Fig. 1) from 2000 to 2013 as part of the northern Gulf of Alaska long-term observation program. Large zooplankton were collected at night with a 1 m^2 MOCNESS system (2000 - 2004) and a 0.5 m^2 Multinet system (2005 - 2013) fished in 20 m depth increments from 100 m to the surface using 505 μm mesh nets. Small zooplankton were

collected with a CalVET net fished vertically during the day from 100 m depth to the surface using 150 μm mesh nets. The CalVET nets were equipped with General Oceanics flowmeters to measure volume filtered. Samples were processed as outline in Coyle and Pinchuk (2003, 2005). Biomass was converted from wet weight to carbon using conversions from Parsons et al (1988) (dry weight = 0.2155 wet weight; carbon = 0.525 dry weight). During May only the coarse mesh samples were used in the analysis because biomass in spring is overwhelmingly dominated by large copepods. In addition, samples from the upper 20 m only were used because most phytoplankton production and copepod biomass occurs in the upper 20 m (Coyle and Pinchuk, 2005). Fall copepod biomass is dominated by the smaller size fractions so both the coarse and fine mesh samples were used. For fall species and stages < 0.3 mg wet weight were taken from the CalVET nets, larger specimens were from the MOCNESS-Multi net samples, which were integrated to 100 m depth to correspond with CalVET net values. The coarse and fine biomass values extracted as described above were summed to characterize the copepod carbon biomass at each station. All zooplankton data were power transformed ($X^{0.15}$) to remove heteroscedasticity.

3. Results

The results from this study focus primarily on the western shelf and basin because most of the available field observations occur in the western sector. The eastern GOA is included because zooplankton, eddies and currents influencing the western shelf and basin often originate in the eastern sector. Most measures of phytoplankton biomass consist of chlorophyll concentration or ocean color from satellites so these measurements are covered in some detail for model validation. The published phytoplankton indices often have broad confidence intervals due to patchy distributions; they are therefore reported as medians and ranges (Strom et al., 2016). The model indices from the polygons consist of mean or median daily values for the depth interval, season and years, the ranges consist of the maximum and minimum individual values or the maximum and minimum mean or median values from the polygon, depending on the comparison. Comparisons of model output with field observations follow the descriptions of model results in each section.

3.1. Runoff and salinity

The annual cycle of runoff oscillates between minimum values in April, rapidly increases in May followed by maximum values in summer and fall (Fig. 4). The mean runoff in P1 during April is relatively consistent between years at around 0.1 X 10^{-4} kg m^{-2} s^{-1} (~1150 m^3 s^{-1}), but annual means for May varied between 0.3 and 0.6 X 10^{-4} kg m^{-2} s^{-1} (~3500-6900 m^3 s^{-1}), suggesting interannual differences of about two-fold in the onset of the spring runoff. The climatology of simulated salinity on the inner shelf of the Seward Line is maximal in April and early May, declines in late May to October and gradually increases after October (Fig. 5A). The seasonal decline in simulated salinity is greatest at the inner end of the Seward Line (GAK1), salinity gradually increased with distance from shore, and seasonal declines are less than 0.5 PSU at GAK4 and GAK5 (Fig. 5A). Thus much of the freshwater discharge in the simulation is

confined to the coastal region on average, with very little moving out beyond GAK4. During 2001, when mean runoff in May was minimal, simulated salinity at GAK1 followed an upward trend until late May-June (Fig.5B), but in 2005, when mean runoff in May was highest, simulated salinity began its seasonal decline in April (Fig. 5C). During individual years changes in simulated salinity occur as sharp peaks and valleys in response to propagation of small eddies and meanders past the station (Fig. 5B, C). The magnitude of freshwater discharge used in previous model versions (Royer, 2019) is similar to the volume discharge in Hill et al. (2015), but the Hill version had higher and deeper seasonal peaks and valleys due to its higher spatial and temporal resolution; the Royer runoff consisted of monthly average values for the whole northern Gulf region.

Seasonal changes in the climatology of simulated salinity on the outer half of the Seward Line were much less than on the inner shelf; salinity varied by about 0.6 PSU, from 32.5 to 33.1 (Fig. 6A); a distinctive decline was apparent between May and October, followed by a gradual increase from October through December.

3.1.1. Comparison of simulated salinity with measurements

Comparison of simulated salinity climatology for the inner Seward Line stations with salinity measured by CTDs (conductivity temperature depth probe) indicates that the model consistently overestimates salinity at stations GAK1 and commonly at GAK2 (Fig. 5A), where simulated salinity overestimated measured salinity by as much as 3 PSU in August-October. The discrepancy between measured and modeled salinity declined with distance from shore, but increased during summer and fall, and appears to be the result of our technique for incorporating runoff (Section 2.2.1). However, many of the field measurements are scattered among simulated measurements in February-May, indicating that the model was not consistently biased at GAK1-GAK3; measured values at GAK4-5 were consistently above simulated values throughout the simulation, and also appear to be caused by our technique to prevent the runaway stratification artifact.

Simulated salinity consistently overestimated measured salinity by up to 2 PSU on the outer shelf (Fig. 6A); this bias is probably inherited from the initial conditions, which were derived from CFSR oceanographic output for the North Pacific. When periods of lower salinity are observed in outer shelf surface waters, simulated and measured salinities can be similar (Fig. 6C). Low salinity is sometimes related to anticyclonic eddies propagating westward along the shelf break; eddies are stochastic features (Ladd et al., 2016; Okkonen et al., 2003) and are not precisely replicated by the model at specific times and places, because we do not explicitly assimilate altimetry or other data into the regional model. Therefore, some of the discrepancies in measured versus simulated salinity on the outer shelf are probably due to temporal-spatial discrepancies in measured versus simulated eddies and meanders along the shelf break.

Earlier model experiments indicate that doubling the magnitude of the winds increases transport in the ACC, however doubling the magnitude of runoff does not significantly increase transport (Hermann and Stabeno, 1996). Flow through Shelikof Strait for model runs with Hill

versus Royer runoff showed a similar temporal pattern, confirming the observations from earlier model experiments, that salinity has little effect on large scale flow patterns in the ACC (Fig. 7).

3.2. *Dissolved iron concentration*

Since differences in dissolved iron concentration (DFe) appear to be the major factor affecting interannual differences in simulated primary production, processes that can potentially affect DFe in spring and fall are presented below for the Seward Line and for each polygon. The processes include vertical momentum flux (omega) and runoff; advection from the basin onto the shelf, vertical diffusion and iron flux are included for P7. The section concludes with a brief summary of the major findings.

3.2.1. DFe along the Seward Line

Since DFe is introduced mainly by fresh water in this model, the climatology of simulated DFe at the inner Seward Line stations undergoes marked increases with declining salinity (Fig. 5D); this is particularly evident at GAK1 and GAK2 where iron concentration peaks in October, followed by a gradual decline as salinity increases after October. Changes in DFe at GAK1-GAK3 are characterized by sharp peaks in individual years, as different water masses propagate westward along the coast (Fig. 5E, F). The climatology indicates that DFe uptake by phytoplankton is saturated ($\geq$ 2 nM) on the inner shelf, especially during late summer and fall. DFe changes off shore at GAK4 and GAK5, but high amplitude peaks are generally absent. Simulated DFe climatology on the outer shelf along the Seward Line was consistently under-saturated with respect to DFe uptake; maximum mean DFe never exceeded 2 nM (Fig. 6D). During individual years, DFe above 2 nM occurred as distinct peaks, in response to propagation of low-salinity water masses through the station (Fig. 6B, C, E, F).

3.2.2. Geographic distribution of DFe

The geographic distribution of DFe along the shelf during March-May declines in response to elevated primary production with increased light availability in the simulation. DFe injection with runoff is minimal in March-May as much of the precipitation remains sequestered on the continent as snow and ice. Thus, DFe climatology remains under 1 nM on the outer shelf between the Canadian border and 156° W (Fig. 8B). DFe markedly increases on the inner shelf during June-August, as runoff increases due to melting of snow and ice on the western slopes of the coastal range (Fig. 8C). However, iron concentrations on the outer shelf off the Kenai Peninsula and Kodiak are under 1 nM due to intrusion of oceanic surface water onto the shelf; the seasonal DFe in the basin is minimal, due to removal by phytoplankton. The only sources of DFe to basin surface waters in these simulations are offshore transport from eddies and upwelling from below the pycnocline. Simulated DFe remains high on the shelf during September-October because elevated runoff continues through fall (Fig. 8D). The region of lower iron concentration on the outer shelf off Kodiak and the Kenai Peninsula remains, although periodic offshore advection of DFe-rich water is observed out to the shelf break.

3.2.3. Processes influencing DFe on the western and eastern shelf

Simulated DFe was significantly higher on the western shelf (P1) during spring 2000-2006 relative to spring 2007-2013 (Table 2B, P1). As runoff increases in summer and fall, the differences in DFe between year groups remained significant over the western shelf. Multiple regression and correlation revealed no significant relationship between DFe and omega or runoff during spring or fall (Table 3A, C, P1). DFe in P1 during spring and fall was highly correlated to DFe during other seasons, suggesting seasonal consistency with respect to DFe in P1 (Table 3B, D, P1).

The Seward Line Polygon (P7), that characterizes the portion of the western shelf with low DFe, had significantly higher simulated DFe in 2000-2006 relative to 2007-2013 during both spring and fall (Table 2B). DFe in March-May was significantly negatively correlated to advection of water from the basin into P7 during fall only, and positively correlated to horizontal flux of iron into the polygon from the basin in spring (Table 4A). DFe in P7 in March-May was unrelated to onshore advection during spring, summer and winter. R_a^2 for spring DFe increased substantially with addition of horizontal advection of water onto the shelf during fall and iron flux onto the shelf in spring (Table 4A). DFe in P7 was significantly correlated to DFe in P7 during other seasons (Table 4B). In contrast to spring, the multiple regressions for P7 indicated that interannual differences in DFe in fall were influences by a number of variables including: omega on the shelf and in the adjacent basin, advection of water from the basin onto the shelf, vertical diffusion of iron into the surface layer and horizontal advections of iron onto the shelf (Table 4A). DFe was significantly correlated to omega on the shelf in fall only (Table 4A), suggesting that conditions that weaken downwelling on the shelf promote higher DFe in P7 in fall. Correlations of DFe in P7 with omega in the adjacent basin and with advection onto the shelf were negative during fall, suggesting that stronger downwelling in the basin and weaker onshore flow promoted higher DFe on the shelf in fall. DFe in fall was significantly correlated to horizontal flux of iron into P7 and vertical diffusion of iron into the surface layer. DFe in P7 during fall was significantly correlated to DFe in winter and spring, but uncorrelated to DFe in summer (Table 4B). Horizontal advection and vertical diffusion of iron into the surface layer in P7 were not significantly different between year groups.

Simulated DFe in the eastern shelf polygon (P4) was not significantly different between year groups during spring and fall (Table 2B). Mean DFe during March-May was significantly correlated to runoff in March-May and to omega in the adjacent basin polygon in fall (Table 3, P4). R_a^2 in the multiple regressions increased with addition of runoff in winter, spring and summer, suggesting that runoff influenced DFe on the eastern shelf more than the western shelf. DFe in March-May was correlated to DFe in winter only (Table 3B), suggesting that currents were more likely to produce significant seasonal differences in DFe on the eastern shelf than on the western shelf. Interannual differences in simulated DFe in P4 during fall were correlated to omega in fall and runoff in summer (Table 3C, P4), however R_a^2 in the multiple regressions increased when runoff in fall, summer and winter, and omega in winter were added to the

regressions. These results suggest that DFe on the eastern shelf in fall is influenced primarily by runoff and omega on the shelf. DFe on the eastern shelf in fall was not significantly correlated to DFe in other seasons (Table 3D, P4).

3.2.4. Processes influencing DFe in the western and eastern basin

The multiple regressions indicated that DFe in the western basin (P2) during spring was related primarily to DFe in the basin polygon during other seasons (Table 5B). DFe in spring was significantly correlated to omega on the adjacent shelf during winter (Table 5A); the correlation was positive suggesting that weaker downwelling on the shelf during winter promoted higher DFe in the adjacent basin. Although the maximum R_a^2 value relating DFe in the basin during spring to omega in the basin and adjacent shelf was almost 0.89 and the P values for the regression were significant, the relationship was dominated by the single strong positive correlation of basin DFe to omega on the shelf in winter. Addition of advection from the basin into P7 during spring, fall and summer increased R_a^2 to 0.981 (P declined to 0.015). Only the March-May advection was significantly correlated to DFe in P2. Correlations of DFe in P2 to advection were negative, suggesting that less advection onto the shelf from the basin during spring and summer led to higher DFe in the basin in March-May. None of the correlations relating DFe to omega in P2 during fall were significant (Table 5C). The greatest increment in R_a^2, from 0.218 to 0.607, occurred with addition of omega on the shelf in winter. Addition of advection from the basin onto the shelf during summer and spring increased R_a^2 to 0.932, but none of the correlations relating DFe in P2 to advection were significant. The correlations were negative, indicating that weaker advection onto the shelf increased DFe in the adjacent basin during fall. All the correlations of DFe in P2 during fall to DFe in other seasons were significant; R_a^2 for the multiple regression was essentially unchanged (Table 5D), suggesting that DFe in other seasons could account for somewhat less than half of the variance in DFe in P2 during fall.

Simulated DFe was significantly higher in the eastern basin polygon (P5) in 2000-2006 relative to 2007-2013 in spring only (Table 2B). Multiple regressions produced no significant relationships between DFe and omega (Table 6A, C) in spring or fall. Correlations of DFe in March-May and September with DFe in other seasons were only significant for winter and summer respectively, suggesting that DFe in the eastern basin polygon was changing rapidly seasonally (Table 6B, D). Failure of the multiple regressions to produce significant relationships between DFe and omega suggests that stochastic processes in the model, such as eddy activity, were probably influencing DFe in P5.

3.2.5. Comparison of iron concentration with measured values

Measured DFe in the ACC were 0.5-4 nM with a mean of ~2 nM between Yakutat and the Kenai Peninsula in August and September 2007 (Lippiat et al., 2010). DFe enters the coastal

ocean with freshwater and rapidly decreases outside the ACC (Lippiat et al., 2010; Wu et al., 2009). Dissolved iron concentration along the Seward Line in September 2011 was 5 nM at GAK1, but declined rapidly with distance from shore and was < 1 nM beyond GAK4 (Agilar-Islas et al., 2016, see their Fig. 8b). The cross-shelf pattern of simulated DFe along the Seward Line (Fig. 5-6, D, E, F) is similar to observations, suggesting that the model is accurately simulating the pattern of cross-shelf advection. Although the salinities at GAK1 and 2 are overestimated by the model, the simulated DFe was not underestimated because DFe entering with freshwater was adjusted to produce coastal DFe concentrations approximating measured values.

3.2.6. DFe summary

The annual cycle of runoff generates strong seasonal changes in the coastal DFe, with lowest values in late winter and spring, and highest values in summer and fall when runoff is greatest. Consistent downwelling pushes DFe depleted HNLC surface water shoreward on the western shelf and confines most of the DFe entering with runoff to the coastal zone, where DFe is saturated with respect to phytoplankton uptake through much of summer and fall. DFe on the central western shelf (P7) was negatively correlated to onshore advection in spring and fall and positively correlated to omega and vertical diffusion in fall but not in spring, indicating a greater influence of vertical transport sources of DFe in fall relative to spring. DFe in the western basin in March-May was positively correlated to omega in winter and negatively correlated to flux from the basin onto the shelf, suggesting that vertical flux is a major source of DFe to basin surface waters; DFe in surface waters of the eastern basin was not strongly correlated to vertical mixing and may be more influenced by stochastic processes such as eddies and meanders.

3.3 Nitrate concentration

Peak simulated nitrate concentrations in the upper 25 m of coastal waters were 14-18 μM in late winter and spring (Fig. 9A, B), with values of over 25 μM in the western basin where upwelling is strongest. DFe injection with runoff in spring elevates coastal production; nitrate becomes the limiting nutrient and is quickly consumed from the Ekman layer, resulting in concentrations close to 0 μM in the upper 25 m on the western inner shelf during summer and fall (Fig. 9C, D). Nitrate is also limiting in the simulations on the eastern shelf and the shelf west of Kodiak, where DFe uptake by the phytoplankton is saturated. Simulated nitrate concentration in the western basin declines to 14-17 μM during summer due to iron-limited summer production, and is under 10 μM in the eastern basin where eddies commonly advect DFe offshore (Fig. 9C, D); the eastern basin water mass is analogous to transition waters off British Columbia (Burt et al., 2018).

Simulated nitrate concentration was compared with nitrate concentration measured from FOCI (Fisheries Oceanography Coordinated Investigations) stations in the northern Gulf of Alaska (Fig. 10A). Nitrate from simulations was taken at the same time, depth and location as the FOCI samples to provide a direct point to point comparison. The black points represent

individual comparisons (Fig. 10B). The broad scatter around the identity line reflects stochastic processes in the model and the environment but the slopes of the regression and identity lines were not significantly different ($P < 0.05$), suggesting little statistical bias in the simulation relative to actual data points. Nevertheless, a higher number of data points between about 25 and 40 μM were above the identity line. This discrepancy seems to be caused by mixing in the model leading to elevated nitrate concentration in the upper water column over the basin relative to the long-term climatology (Fig. 10C, D). The general pattern of simulated nitrate distribution conforms to the World Ocean Atlas climatology (https://www.nodc.noaa.gov/OC5/woa13/woa13data.html). Simulated nitrate concentration over the shelf along the Seward Line was similar to published values (Childers et al., 2005). Simulated and measured nitrate concentration in the upper 10 m at shelf stations along the Seward Line in April and May was ~5 μM, but declined to zero in June-July and began a gradual increase to ~15 μM by October. The climatology of simulated mean nitrate concentration in the upper 25 m at the outer end of the Seward Line did not decline below 10 μM during June-October; measured values were zero near the surface and 15 μM at 25 m depth in July (Childers et al., 2005).

3.4. Chlorophyll concentration

Although the climatology of simulated productivity for the shelf as a whole along the Seward Line was relatively constant during the production season (Fig. 11A), chlorophyll peaks were confined primarily to March-May (Fig. 11D). The climatology of simulated chlorophyll peaks during summer was suppressed by high C-Chl ratios, but low chlorophyll peaks were produced in the climatology plot in fall, as declining light levels lower the C-Chl ratio. Distinct simulated chlorophyll peaks were produced during March-May in individual years; distinct, narrow peaks were produced on the outer shelf and off the shelf break in summer and fall (Fig. 11E, F). As the simulated chlorophyll concentration in the water column increased, the fraction of the total chlorophyll contained in the large phytoplankton component increased (Fig. 12). The maximum mean water-column chlorophyll concentration at any location in Polygon 1 was about 45 mg m^{-3} during March-May of 2006, a year of high spring production, but dropped to about 11 mg m^{-3} during September-October (Fig. 12A, B). Maximum mean simulated water-column chlorophyll concentrations in 2010, a year of low simulated low production, were about 24 and 15 mg m^{-3} in spring and fall respectively (Fig. 12D, C). Most chlorophyll concentrations were between 0 and 15 mg m^{-3} in spring and 0 and 8 mg m^{-3} in fall of 2006 (Fig. 12A, B), and in 2010 they were between 0 and 15 mg m^{-3} in spring and 0 and 5 mg m^{-3} in fall (Fig. 12C, D).

The simulated chlorophyll depth profiles were not an accurate reflection of the depth profiles of phytoplankton carbon biomass (Fig. 13A, B), because the C-Chl ratio of the phytoplankton decreases with depth in response to decreasing PAR. While phytoplankton carbon biomass was constant to ~10 m depth (Fig. 13B), the chlorophyll concentration increased from the surface to 10 m depth, followed by a gradual decline at depths below the chlorophyll maximum (Fig. 13A).

3.4.1 *Comparison of model chlorophyll concentration with published values*

A subsurface chlorophyll maximum with chlorophyll concentrations of 0.63-1.33 mg m^{-3} at 15-25 m depth has been reported on the western GOA shelf in May and July (Table 7A). The simulated mean chlorophyll concentration in the chlorophyll maximum layer during April-May in P1 varied from 0.8 mg m^{-3} in 2003 and 2013 to about 2.2 mg m^{-3} in 2007 (Fig. 13A).

Most field measurements of chlorophyll concentration in 2011 and 2013 were under 2 mg m^{-3}, with maximum values of over 10 mg m^{-3} in the large size fraction (Strom et al., 2016; see their Fig. 3). The simulated size fraction of large phytoplankton chlorophyll to total phytoplankton chlorophyll (Fig. 12) followed a similar pattern to that of field observations (Strom et al., 2016); samples with the highest fraction of large cells had the highest chlorophyll concentrations. The preponderance of maximum water-column averages of simulated chlorophyll concentrations were within the range of measured values (0 – 10 mg m^{-3}); each dot in Fig. 12 represents one of 19327 grid points in P1. The maximum simulated chlorophyll integrated to 50 m depth during March-May for P1 was 86-2568 mg m^{-2} depending on the day and location, with a median of 25.5 mg m^{-2}; measured median chlorophyll values were 11-302 mg m^{-2} (Table 7F).

3.4.2. Seasonal distribution of chlorophyll

Simulated phytoplankton growth as indicated by chlorophyll is limited to the very nearshore regions in lower Cook Inlet and east of PWS during January and February (Fig. 14A). The simulated phytoplankton blooms in the nearshore environment begin in late March and early April and blooms are present along the entire coast from the Canadian border to the Shumagin Islands (Fig. 14B). During April and May the blooms spread across the shelf in the eastern and western portions of the grid, but are much weaker on the outer shelf of the central GOA (Fig. 14B, 15B). Blooms continue during summer on the shelf at the eastern edge of the grid, in lower Cook Inlet and on the outer shelf west of Kodiak (Fig. 14C, 15C). Fall blooms occur at the eastern grid boundary, off PWS, in Lower Cook Inlet and in Shelikof Strait (Fig. 14D. 15D).

3.4.3. Comparison of satellite and model chlorophyll distribution

Both satellite observations and simulations revealed high concentrations of chlorophyll around Kodiak Island and northeast of Haida Gwaii in April. The satellite detected blooms across the entire western shelf in May (Waite and Mueter, 2013), but simulations indicated low values on the outer shelf between 151° W and 144° W. The low simulated values on the outer shelf relative to satellite observations are due to circulation restricting iron-rich waters to the ACC on the inner shelf during March-May. Blooms in summer and fall in Lower Cook Inlet (Fig. 14C, D) have been attributed to tidal mixing (Henson, 2007). Satellite images indicate elevated chlorophyll on the outer shelf west of Kodiak in June (Waite and Mueter, 2013); simulations indicate that these blooms are due to transport of iron-rich water out of Shelikof Strait and across the shelf to the outer shelf and shelf break. Satellite observations detected

blooms in August-September in Shelikof Strait and off the east coast of Kodiak (Waite and Mueter, 2013). Both satellite observations and simulations showed high chlorophyll concentration during summer and fall north of Haida Gwaii, suggesting that processes affecting production in the simulations were mimicking reality. A March bloom off the Kenai Peninsula was observed in the simulations but was absent from the satellite data; this simulated bloom may be related to a lack of wave mixing in the physical model, resulting in earlier declines in vertical mixing than is observed in field data.

Satellite and simulated chlorophyll in the upper 10 m are summarized in Table 8. Simulated values in the upper 10 m were averaged because the satellite could detect chlorophyll to a maximum depth of about 10 m (Waite and Mueter, 2013). All satellite values fall within the range of simulated values for the coastal polygons and for offshore P2. However, the maximum and minimum daily mean simulated values for entire polygons for any given season and year were occasionally outside the corresponding mean satellite value (Table 8). The mean daily simulated bloom peak in May was above the satellite measurement in P4, while the satellite measurement was above the mean daily simulated bloom peak in P1 in May. While satellite measures of chlorophyll concentration usually fall within the range of simulated values, the actual magnitudes of simulated productivity in space and time are a function of circulation patterns at various scales that are stochastic and do not always correspond in space and time to satellite measures of chlorophyll concentration.

3.4.4. Carbon chlorophyll ratios

The climatology of simulated C-Chl ratios in the upper 25 m of the water column followed the annual light cycle, with maximum C-Chl ratios for each depth occurring in June. Simulated C-Chl ratios for large phytoplankton varied from about 20 in March and October to about 60 in June-July, depending on depth; C-Chl ratios for the small phytoplankton varied from about 50 to 140. Measured C-Chl ratios range from about 15 to 311 with reported medians of 41-76 (Table 7C, D, E). The model is therefore producing C-Chl ratios within the range of measured values. Recent measurements in the subarctic eastern North Pacific indicate that about two-thirds of the variation in C-Chl ratios can be attributed to light acclimation, while the remaining variation is due to nutrient limitation and species composition (Burt et al., 2018).

3.5. Primary productivity

Although simulated primary productivity events vary in space and time, climatologies suppress discrete peaks commonly observed at specific stations during individual years (Fig. 11). Periods of elevated productivity occurred from March to May near the coast, they occur from March through October near the outer ACC boundary (GAK4), and from June to October at the outer shelf stations (GAK6-8, Fig. 11A). The climatology of simulated seasonal productivity off the shelf break occurs as a broad low curve with maximum values of about 0.5 g C m^{-2} d^{-1} in July-September followed by a gradual decline. During a high productivity year (2006), peaks occurred along the Seward Line in March, May, July, August and October (Fig. 11B, E). During

a low productivity year (2010) peaks occurred in the ACC at GAK1 during March, at the outer ACC boundary in April, and a number of post-bloom peaks occurred at all Seward Line stations, including stations off the shelf break, for the remainder of the production season (Fig.11C). Average productivity during 2010 on the inner shelf was about 74% of productivity during 2006, suggesting that interannual differences in productivity are affecting primarily the inner shelf. Productivity on the outer shelf was marginally higher during 2010 relative to 2006.

Simulated mean primary production was minimal during winter, with maximum production around 10 g C m^{-2} in the fjords and coastal zones on the western shelf and 10-15 g C m^{-2} in the fjords on the eastern shelf (Fig. 15A). Mean production rates accelerated during spring, with production averaging 80-120 g C m^{-2} along the coast on the eastern shelf, in PWS and off the Kenai Peninsula, in Shelikof Strait and on the shelf west of Kodiak (Fig. 15B). Production was 100-150 g C m^{-2} in June-August north of the Canadian border, on the outer shelf off PWS and the Kenai Peninsula, in lower Cook Inlet and on the outer shelf south and west of Kodiak (Fig. 15C). Production was under 100 g C m^{-2} where DFe was above 2 nM and nitrate was limiting at < 5 μM (Fig. 8C; Fig. 9C). Simulated production during fall was 80-100 g C m^{-2} in the coastal zone north of the Canadian border, on the outer shelf east of the Seward Line off PWS and in lower Cook Inlet (Fig. 15D). Patches of elevated production also occurred in Shelikof Strait and on the outer shelf west of Kodiak.

3.5.1. Phytoplankton growth rate:

An estimate of the simulated phytoplankton growth rate was computed by dividing the daily production by the daily carbon biomass estimate of the large and small phytoplankton components. The median growth rate in P1 during March-May 2000 was 1.07 and 0.79 d^{-1} (range: 0.51-1.43 and 0.40-1.10 d^{-1}) for large and small phytoplankton, respectively. The minimum, median and maximum simulated values for 2013 were 0.33, 1.05, 1.34 and 0.24, 0.83, 1.05 d^{-1} for large and small phytoplankton respectively. The field estimates of median growth rates from 2011 and 2013 were 0.18 and 0.65 d^{-1}; maximum values were 0.6 and 1.3 d^{-1}, respectively (Table 7H) (Strom et al., 2016).

3.5.2. Factors influencing primary production

ANOVA tests showed that simulated production during March-May was significantly higher for 2000-2006 by about 15% relative to 2007-2013 in all polygons (Table 2A). However, primary productivity during September-October was not different between year groups in three of the five polygons (P1, P2, P5). Successive stepwise multiple regressions indicated that primary production was most influenced by iron area and iron concentration during spring. Iron concentration and iron area, representing a nutrient source, generated consistently significant P values for the multiple regressions with primary production in coastal polygons (Table 9A). During fall, when runoff is highest, iron concentration was an insignificant contributor to multiple regressions in the shelf polygons (Table 9B), but was significantly correlated to interannual productivity in P7. The nitrate and iron flux variables did not improve the multiple

regression for productivity during May; only the horizontal flux of nitrate into P7 increased R_a^2 during fall but the regression remained statistically insignificant (Table 9B). Addition of PAR increased the R_a^2 for P4 during fall (Table 9B) but had little influence in other coastal polygons. Addition of nitrate concentration had little effect on R_a^2 in coastal polygons, and nitrate concentration was significantly negatively correlated to primary production in P7 only. In contrast, nitrate concentration was significantly negatively correlated to primary production in both basin polygons during fall (Table 10B), indicating that nitrate was being removed by seasonal production at a faster rate than its replenishment. Iron concentration remained a significant contributor to the multiple regressions in the basin polygons (Table 10).

3.5.3. Comparison of model productivity with published values

The simulated maximum primary productivity on the western shelf (P1) for each day during March-May 2000 was 0.6 to 14.8 g C m^{-2} d^{-1} with a median of 6.7 g C m^{-2} d^{-1}, the median of all values for March-May was 0.43 g C m^{-2} d^{-1}; the medians of measured values for May 2011 and April 2013 were 0.9 and 2.5 g C m^{-2} d^{-1} (range: 0.36 - 4.87 g C m^{-2} d^{-1}**;** Table 7I).

3.6. Productivity and copepod biomass

Interannual differences in simulated primary production divided into two distinct periods: 2000-2006, when production in P7 was consistently above the long-term mean, and 2007-2013, when production was below the mean (Fig. 16A, B). The carbon biomass of calanoid copepods in the upper 20 m from 505 μm mesh nets taken during May along the Seward Line followed a similar pattern (Fig. 16C, D). A Mann Whitney test revealed that the calanoid biomass was significantly higher ($p < 0.05$) during 2001-2006 relative to 2007-2013 (Table 11A). The equivalent parametric test revealed that the calanoid and *Neocalanus* biomasses were both significantly different (Table 11B). Calanoid and cyclopoid biomass in fall was not significantly different between year groups (Table 11C, D). Regression analysis comparing simulated primary production and simulated calanoid production against mean calanoid carbon biomass from net tows during May had R^2 values of 0.65 and 0.51, respectively, suggesting that model production for March-May could explain roughly 50-65% of the variance in measured calanoid biomass along the Seward Line. The P levels for the primary productivity regressions were both under 0.05 (Table 12).

The climatology of simulated chlorophyll concentration to 25 m depth on the western GOA shelf (P1) shows a distinct dip corresponding to the period when *Neocalanus* carbon biomass was maximal in the upper 25 m (Fig. 17A, bold line). This dip is due to consumption of phytoplankton by large microzooplankton and calanoid grazers in this simulation. The solid bar (Fig. 17A) is the climatology of *Neocalanus* carbon biomass as measured by net tows along the Seward Line in P7 during early May from 2000 to 2013. A similar dip in chlorophyll concentration followed by a minor rebound is also observed in P4 (Fig. 17B). During the GLOBEC years (1998-2003) mean *Neocalanus* biomass in the upper 20 m along the Seward

Line grew from 4.85 mg C m^{-3} in early April to 58.5 mg C m^{-3} in early May; biomass of all calanoids grew from 10.39 mg C m^{-3} in April to 80.7 mg C m^{-3} in May; these are increases in biomass of about 12 and 8 times, respectively (Coyle and Pinchuk, 2003). The energy for this growth came from phytoplankton production through direct consumption by the copepods and consumption by the copepods of microzooplankton, which feed on the phytoplankton. The *Neocalanus* in the simulations migrate to depths greater than 500 m and therefore disappear from the upper layers in June, resulting in a minor rebound in the simulated chlorophyll concentration (Fig. 17A, B).

Copepod biomass in fall was significantly below the long-term mean in 2003 and 2004 and was significantly higher than the long-term mean in 2011 (Fig. 18), however there was no evidence of any relationship between observed copepod biomass along the Seward Line during August-October and simulated production for August-October (Table 13).

4. Discussion

The modeling results indicate that the climatology of seasonal production on the western GOA shelf in the Seward Line region is relatively constant throughout the production season (Fig. 11A). This observation contradicts the paradigm from chlorophyll measurements that production is concentrated in spring primarily and autumn secondarily. The simulations indicate that chlorophyll is not an accurate measure of phytoplankton carbon biomass because the C-Chl ratios vary throughout the production season, primarily in response to light availability. Thus, summer and fall productivity episodes on the GOA shelf do not produce the high chlorophyll peaks characteristic of spring blooms.

Equating chlorophyll with phytoplankton carbon biomass can influence ecological interpretations of the data. The commonly held assumption that total annual production of the North Pacific HNLC waters is lower than production in the North Atlantic is based on low chlorophyll values in the Pacific relative to the Atlantic and exhaustion of nitrate in North Atlantic surface waters by midsummer. Recent observations indicate that nitrate drawdown in the North Pacific is similar to or higher than in the North Atlantic, suggesting that annual production is similar (Westberry et al., 2016). The higher nitrate concentration in North Pacific surface waters during midsummer was attributed to higher winter nitrate concentration in the North Pacific (~15 μM versus ~8 μM in the North Pacific and North Atlantic respectively). Although seasonal nitrate utilization suggests similar annual primary production, iron limitation clearly suppresses diatom blooms and alters the phytoplankton species composition (Boyd et al., 2005), thereby influencing productivity rates and energy transfer through the food web.

With iron concentration appearing to be the most important variable influencing primary production in the simulations, factors affecting iron concentration are discussed in some detail (Section 4.1). The calanoid biomass from Seward Line net tows is related to simulated production during spring so observations relating production to copepod biomass are discussed (Section 4.2). Finally, the change in the simulated production anomalies from positive to

negative in 2006-2007 may be related to decadal shifts in climate indices and these shifts may influence fisheries (Section 4.3). If future model refinements and simulations can verify these relationships, the model may eventually become a useful quantitative tool to aid in fisheries management.

4.1. Iron as a nutrient

The multiple regressions on simulated primary production indicated that DFe controlled interannual differences in primary production, but DFe in the model is not well constrained. The only DFe sources in the model are input with runoff at the coastline and input through the southern and western boundaries. Flux of iron through the Alaskan-British Columbian grid boundary is similar in magnitude to flux into P7; it varies temporally from 0 to 4 X 10^5 μM s^{-1}. The mean simulated DFe profile below 200 m in Polygon 2 had a maximum of about 0.6 nM in 1996, in conformity with initial conditions, but declined to a minimum of 0.58 nM by 2010, which indicates that DFe below 200 m depth was gradually disappearing from the simulation at a rate of roughly 0.2% per year. The loss is caused by mixing of DFe into the euphotic zone, followed by uptake and sinking by phytoplankton out of the water column. The carbon-iron ratio of phytoplankton (f_{ec}) in the model was constant at 2 μM M^{-1}, the value reported for HNLC regions of the Pacific (Fennel et al., 2003). However f_{ec} is dependent on growth rate and varies in the North Pacific in the range of 2.5-11.4 for growth rates of 0.67-1.55 d^{-1} (Sunda, 1997). Elevating f_{ec} in the model will cause the iron to cycle faster during phytoplankton growth and degradation. Field measurements of the sinking rate of phytoplankton in the GOA and the iron concentration in the phyto-detritus would aid in quantifying the cycling rate of iron in the water column. However, as the particles aggregate and sink, the iron is released into soluble and colloidal components and partially resorbed in a process called scavenging (Bruland and Lohan, 2003; Boyd and Ellwood, 2010), complicating development of robust quantitative rates of change in iron concentration due to particle sinking and degradation.

Iron enters the GOA in the dissolved and particulate phases; the latter occurs as leachable and refractory components (Agilar-Islas et al., 2016**).** The dissolved component is available for biological uptake (Morel et al., 2003), but leachable particulate iron may require days to weeks to become available. If the leaching rate of iron from particles and the supply rate of dissolved iron is less than the iron uptake rate required for a bloom to occur, then iron will be limiting (Morel et al., 2003). Modeled and measured iron along the Seward Line follow the distribution of the dissolved component (Agilar-Islas et al., 2016**,** see their Fig. 8b), with values above 2 nM within 50 km of the coast and under 1 nM from 50 km outward to the shelf break (Fig. 5-6). Although dissolvable iron concentrations exceed 10 nM along the entire Seward Line, elevated nitrate concentrations suggested that iron was probably limiting production during fall 2011 (Agilar-Islas et al., 2016, see their Fig. 8a,c**)**. Thus, the available measurements indicate that phytoplankton on the GOA shelf seaward of 50 km from the coast were responding to the availability of dissolved iron rather than leachable iron.

DFe near the shelf break below 200 m is probably underestimated by the simulation. Recent measurements indicate DFe on the order of 1-1.5 nM near the shelf break from 200-1000 m depth (Agilar-Islas et al., 2016). Iron leaching from slope and shelf sediments and offshore advection is a probable source of DFe to epibenthic layers (Lam and Bishop, 2008), but actual rates of iron input from shelf and slope sediments remain uncertain. Crusius et al. (2017) were able to reproduce measured DFe on the shelf off the Copper River delta for spring using a model that assumed that iron leaching from sediments was the sole source. The authors did not elaborate on the bottom type or the oxygen concentration. Oxygen in seawater causes DFe to form oxyhydroxide polymers of very low solubility. Therefore, the concentration of dissolved iron in pure oxygenated seawater is probably not greater than 10^{-18} M at biological pH but micromolar concentrations are required for optimal phytoplankton growth (Neilands, 1995). To survive, organisms must produce ligands, organic molecules that can effectively compete with hydroxyl ions for the available DFe. Therefore, in the absence of hypoxia the availability of Fe-binding ligands caps the concentration of DFe in the euphotic zone and the benthic boundary layer (Biller et al., 2013; Lippiatt et al., 2010; Agilar-Islas et al., 2016) so the amount of DFe does not the exceed the concentration of the strong-binding ligands. The concentration of the ligands in the GOA water column was in excess of DFe during spring and summer of 2011, indicating that the ligands were not iron-saturated (Agilar-Islas et al., 2016). Measurements from the central California Current upwelling region indicate that DFe in the benthic boundary layer is not only a function of ligand concentrations, but also a function of the width of the benthic mud band and the oxygen concentration: the narrower the band, the lower the DFe, but the lower the oxygen concentration, the higher the DFe (Biller et al., 2013). Further refinement of production models on the GOA shelf will probably require mapping of the DFe and oxygen concentration in the bottom layer relative to the area of underlying sediment types.

Atmospheric dust deposition on the order of 1-10 X 10^6 M of soluble iron yr^{-1} in the northern Gulf of Alaska is another potential iron source (Brown et al., 2012; Boyd and Ellwood, 2010). If one assumes an area for the GOA equal to the oceanic area of the CGOA grid, the annual input would be on the order of 3.5-35 pM m^{-2} d^{-1} (1.3-13 nM m^{-2} yr^{-1}) but it is unclear how this input varies by region and year. In addition, only about 1-10% (mean of ~2%) of the iron in dust is soluble in seawater (Bruland and Lohan, 2003). Eddies propagating westward from the eastern boundary is another source of iron to the interior (Ladd et al., 2009). Roughly 50-80% of the chlorophyll observed by satellite over the ocean basin occurs in eddies (Crawford et al., 2007). Sitka and Yakutat eddies are observed in the simulations as regions of elevated iron and chlorophyll concentration relative to the surrounding basin (Coyle et al., 2012). Episodic gap winds occur occasionally along the northern Gulf of Alaska coast, particularly during fall (Ladd et al., 2016; Ladd and Cheng, 2016). If gale force winds blow over exposed glacial sediments, dust plumes can occur up to 400 km from the coast and may supply an amount of soluble iron equivalent to the amount delivered by eddies (Crusius et al., 2011). It is estimated that about 90% of the Copper River discharge is transported westward, 30% enters Prince William Sound, of which 30% exits the sound through Montague Strait (Wang et al., 2014), thus

it represents a large potential source of iron to the western shelf and basin. Measurement of DFe in freshwater entering the ocean might aid in quantifying the amount of iron from runoff, however, flocculation and sedimentation of iron in the estuary may remove much of the iron entering with freshwater (Bruland and Lohan, 2003, Schroth et al., 2014). While these processes are potential sources of interannual differences in iron concentration on the shelf, it is unclear how to convert this information into reliable algorithms expressing the amount of iron sources and sinks and its cycling in the GOA at space and time scales relevant to phytoplankton production. However, the close agreement in cross-shelf distribution between simulated and measured DFe along the Seward Line suggests that runoff is the most important source of DFe on the western GOA shelf.

4.2. Production and copepod biomass.

Based on extrapolation of ^{14}C measurements, primary production on the GOA shelf was estimated at 145-300 g C m^{-2} y^{-1}, with highest values in lower Cook Inlet and off the Kenai Peninsula (Sambrotto and Lorenzen; 1986). Mean simulated annual primary production in each shelf polygon from March through October was 191- 209 g C m^{-2}, with the highest production in P7, lowest in P4. Simulated primary production for March-October in the basin polygons was 134-142 g C m^{-2} with the highest value in P5, caused by higher eddy activity relative to the western basin (P2). Primary production in the upwelling region of the Northern California Current was estimated at 650 and 300 g C m^{-2} y^{-1} for the shelf and slope respectively (Perry et al., 1989). Primary production over the southeast Bering Sea shelf was estimated at 166-172 g C m^{-2} y^{-1} (Walsh and McRoy, 1986; Cross et al., 2014). The simulated primary production on the GOA shelf falls within the range of extrapolated estimates, and is intermediate between that of the southeastern Bering Sea shelf and the Northern California Current system.

Simulated mean production during March-May in P7 accounted for 50-65% of the variance in the annual means of measured biomass of large calanoids along the Seward Line, suggesting a tight coupling between phytoplankton production and calanoid biomass during spring. Temperature-copepod production measurements from Seward Line process studies (Liu and Hopcroft, 2006a, b) were used to calibrate the model (Coyle et al., 2013), thus close agreement between the simulated and measured large copepod carbon biomass climatology in the upper 20 m during May (Fig. 17A) is expected. Process studies on the shelf revealed no differences in size and lipid storage relative to measured mesoscale differences in ambient chlorophyll concentration and ingestion rates of phytoplankton by *Neocalanus* during GLOBEC process cruises, suggesting that phytoplankton production was not limiting *Neocalanus* growth (Dagg et al., 2006). However, chlorophyll concentrations are highly variable temporally as well as spatially (Waite and Mueter, 2013, this simulation), so chlorophyll concentration during any given cruise does not necessarily reflect the feeding history of the experimental animals. In addition, these copepods in the simulation and in nature consume both large phytoplankton and large microzooplankton, indicating that they can modulate their diets to conform to phytoplankton availability, especially in iron-limited environments (Dagg et al., 2009). The

biomass of *Neocalanus* in net tows from the Seward Line in May 1998-2010 is negatively correlated to salinity (Coyle et al, 2013, see their Fig. 18A), suggesting that over time, productivity is stimulating *Neocalanus* growth and survival in coastal regions relative to basin populations. The model is currently parameterized so that *Neocalanus* take large microzooplankton and large phytoplankton in proportion to their carbon biomass.

Recent developments in transcriptomics have permitted a more detailed analysis of the physiological condition of *Neocalanus* across the shelf (Roncalli et al., 2018). Samples were collected during early May (2015) in PWS and at Seward Line stations spanning the inner shelf to the Alaskan Stream beyond the shelf break (GAK1, 4, 9 and GAK14). The analysis indicated that genes involved in fatty acid synthesis, lipid transport and developmental processes were up-regulated in animals from PWS, while genes involved in lipid catabolism were down-regulated (Roncalli et al., in review). In contrast, genes involved in lipid catabolism and proteolysis were up-regulated while genes involved in development were down-regulated in animals from GAK9 and GAK14. The gene expression of animals from GAK1 was similar to animals from PWS and animals from GAK4 were intermediate between outer stations and PWS. The authors interpret these results to indicate that the copepodid stage V *Neocalanus* in PWS and the inner shelf were advanced in their development through the molt cycle relative to *Neocalanus* on the outer shelf and in the Alaskan Stream, and the gene expression of animals on the outer end of the Seward Line indicated a prolonged period of stress due to low food conditions (Roncalli et al., in review). These studies provide additional evidence that *Neocalanus* transported onto the inner shelf and into the fjords are likely to encounter more favorable feeding conditions relative to animals retained in the iron-poor waters of the outer shelf and Alaskan Stream.

4.3 Productivity and climate cycles

The addition of varying C-Chl ratios made phytoplankton in the model more sensitive to light availability relative to earlier model runs, where the slope of the production curve was constant at values measured during summer along the Seward Line (Coyle et al., 2012). This change caused the model to generate earlier near-shore blooms off the Kenai Peninsula than is commonly observed in satellite measurements. The earlier blooms are at least partially due to the absence of surface wave mixing in the ROMS physical model. This lack of adequate surface mixing in the physical model is a particular problem in the GOA, where storms are a persistent phenomenon in winter and spring. Mixing by wind forcing in the GOA is an order of magnitude greater than tidal mixing (Henson, 2007) so this deficiency in the ROMS physical model is not trivial. Our method of introducing freshwater runoff (Section 2.2.1) was a modification required to prevent formation of a surface pool of freshwater across the shelf in February and March, which has never been observed in the field data. Based on a stability ratio model, chlorophyll maps from satellite data, tidal current amplitudes, QuikSCAT wind speed, freshwater flux and NCEP/NCAR heat flux data, Henson (2007) concluded that the water column stabilizes in April during periods of low wind speeds and neap tides, and remains stable until mid-September. The

simulated bloom at GAK1 and 2 in March (Fig. 11B, C) is therefore probably due to insufficient surface mixing in the physical model during March.

The GOA appears to undergo variations in climatic and oceanographic conditions on decadal and interdecadal time scales. A leading expression of the variation is the North Pacific Index in November-March (NPI), which is related to the strength and position of the Aleutian Low (Stabeno, 2004). A deepening of the Aleutian Low linked to a low NPI is associated with warmer wetter winters, and earlier more intense phytoplankton blooms (Henson, 2007). The NPI shifted from negative to positive between 2005 and 2006 (https://climatedataguide.ucar.edu/climate-data/north-pacific-np-index-trenberth-and-hurrell-monthly-and-winter), approximately when the simulated production anomalies shifted from positive to negative (Fig. 16A, B); the NPI shift implies that the blooms in 2000-2006 should be earlier and more intense than blooms from 2007-2013, consistent with our findings in this study. Changes in productivity affecting forage for larval pollock (*Gadus chalcogrammus*) can have a dramatic effect on larval survival and ultimate year class strength (Bailey et al., 1995). The climatology of the distribution of larval pollock and Pacific cod (*Gadus macrocephalus*) on the western GOA shelf in April and May (Doyle and Mier, 2016; see their Figs. 7 and 12) is similar to the geographic distribution of elevated primary production climatologies in the simulations (Fig. 15). The above relationships suggest that the model may prove useful for understanding processes affecting larval survival of some commercially important fisheries stocks on the western GOA shelf in annual and decadal time frames.

5. Conclusions

The GOANPZ model is necessarily a simplification of very complex physical, chemical and ecological systems in the Gulf of Alaska. These systems are subjected to stochastic processes that are not entirely captured by deterministic numerical models. Models are therefore unlikely to provide verifiable long-term predictions of the ecosystem response to climate change. Nevertheless, these models are the best current method of exploring the quantitative ramifications of processes believed to be affecting the GOA physical and biological environment, and they provide a formal mathematical method to extrapolate interpretations of field measurements beyond the space-time constraints imposed by sampling platforms. The following is a summary of what our modeling effort indicated about the GOA ecosystem:

1) Variable C-Chl ratios in response to light levels in the model produced initial slopes of PI curves similar to those from field measurements (Strom et al., 2016). The simulations produced a subsurface chlorophyll maximum at ~10 m depth.
2) Simulations produced chlorophyll peaks in March of some years. These early peaks are not observed in the satellite chlorophyll data and may be artifact due to insufficient surface mixing by the ROMS physical model.
3) Simulated mean primary production estimates on the GOA shelf for 2000 to 2013 were ~204 g C m^{-2} y^{-1} $\pm$ 36 g C m^{-2} y^{-1}, within the range of literature estimates. Simulated primary production in the basin adjacent to the shelf break was ~139 $\pm$ 26 g C m^{-2} y^{-1}.

Highest simulated primary production occurred north of Haida Gwaii, in lower Cook Inlet, off the Kenai Peninsula, in Shelikof Strait and west of Kodiak Island.

4) Approximately 55-65% of the interannual variance in the carbon biomass of large copepods from May net tows in the upper 20 m along the Seward Line from 2000 to 2013 could be explained by interannual differences in spring simulated primary production on the western shelf, suggesting bottom-up control of copepod biomass during spring. Copepod biomass from net tows in fall was unrelated to simulated production.
5) Interannual differences in simulations of shelf primary production during spring were modulated primarily by interannual differences in iron concentration on the GOA shelf. Simulations of shelf production in fall were not markedly influenced by iron concentration due to introduction of high amounts of iron with accelerating runoff in summer and fall.
6) Processes controlling the simulated concentration of iron on the GOA shelf varied by season and location. Interannual differences in iron concentration on the western shelf were influenced by flux of water and iron from the basin onto the shelf. Runoff in summer and fall influenced shelf iron concentrations in fall.
7) The only sources of iron in the simulations were iron injection with runoff and advection through the boundaries. Iron from aerosols and sediment was not modelled. The ability of the model to simulate interannual differences in primary production may be improved by developing reliable algorithms relating interannual differences in iron input from aerosols to atmospheric drivers, and iron input from bottom sediments to sediment type and oxygen concentration. Algorithms simulating removal processes such as sinking rates of detritus and scavenging might also improve model predictions of annual primary production.

Acknowledgements

Computer support was provided by the Research Computing Services at the University of Alaska. Aid in preparation of the modeling grids and physical model was provided by Kate Hedstrom (University of Alaska Fairbanks). FOCI nutrient data were provided by Sarah Hinckley (NOAA). Runoff data were provided by D. F. Hill (Oregon State University, Corvalis). Support for the LTOP was provided by National Science Foundation through the GLOPEC program and by North Pacific Research Board, Alaska Ocean Observing System and Exxon Valdez Oil Spill Trustee Council. This project was funded by the North Pacific Research Board through the Gulf of Alaska Integrated Environmental Research Program. We thank all of these individuals and organizations for their support of this research.

References

Aguilar-Islas, A. M., Seguret, M. J. M., Rember, R., Kuck, K. N., Proctor, P., Mordy, C. W., Kachel, N. B., 2016. Temporal variability of reactive iron over the Gulf of Alaska shelf. Deep-Sea Res. II. 132, 90-106.

Bailey, K. M., Canino, M. F., Napp, J. M., Spring, S. M., Brown, A. L. 1995. Contrasting years of prey levels, feeding conditions and mortality of larval walleye Pollock *Theragra chalcogramma* in the western Gulf of Alaska. Mar. Ecol. Prog. Ser., 119: 11-23.

Beamer, J. P., Hill, D. F., Arendt, A., Liston, G. E., 2016. High-resolution modeling of the coastal freshwater discharge and glacier mass balance in the Gulf of Alaska watershed. Water Resource Res. 52, 3888-3909.

Biller, D. V., Coale, T. H., Smith, G. J., Bruland, K. W., 2013. Coastal iron and nitrate distributions during the spring and summer upwelling season in the central California Current upwelling regime. Cont. Shelf Res. 66, 58-72.

Boyd, P. W., Ellwood, M. J., 2010. The biogeochemical cycle of iron in the ocean. Nature Geoscience. 3, 675-682.

Boyd, P. W., Strzepek, F., Takeda, S., Jackson, G., Wong, C. S., McKay, R. M., Law, C., Kiyasawa, H., Saito, H., Sherry, N., Johnson, K., Gower, J., Ramaiah, N. 2005. The evolution and termination of an iron-induced mesoscale bloom in the northeast subarctic Pacific. Limnol. Oceanogr. 50, 1872-1886.

Brown, M. T., Lippiatt. S. M., Lohan, M. C., Bruland, K. W., 2012. Trace metal distributions within a Sitka eddy in the northern Gulf of Alaska. Limnol. Oceanogr. 57, 503-518.

Bruland, K. W., Lohan, M. C. 2003. Controls of trace metals in seawater. In: Treatise on Geochemistry, Elsevier Ltd. Volume 6, pp. 23-47.

Burt, W. J., Westberry, T. K. Behrenfeld, M. J., Zeng, C., Izett, R. W., Tortell, P. D. 2018. Carbon:chlorophyll ratios and net primary productivity in the subarctic Pacific surface waters derived from autonomous shipboard sensors. Global Biogeochemi. Cycles, 32, 267-288.

Childers, A. R., Whitledge, T. E. and Stockwell, D. A., 2005. Seasonal and interannual variability in the distribution of nutrients and chlorophyll *a* across the Gulf of Alaska shelf: 1998 - 2002. Deep-Sea Res. II. 52, 193-216.

Coyle, K. O., Gibson, G. A., Hedstrom, K., Hermann, A. J., Hopcroft, R. R., 2013. Zooplankton biomass, advection and production on the northern Gulf of Alaska shelf from simulations and field observations. J. Mar Sys., 128, 185-207.

Coyle, K. O., Cheng, W., Hinckley, S. L., Lessard, E. J., Whitledge, T., Hermann, A. H, Hedstrom, K., 2012. Model and field observations of effects of circulation on the timing and

magnitude of nitrate utilization and production on the northern Gulf of Alaska shelf. Prog. Oceanogr. 103, 16-41.

Coyle, K. O., Pinchuk, A. I., 2005. Seasonal cross-shelf distribution of major zooplankton taxa on the northern Gulf of Alaska shelf relative to water mass properties, species depth preferences and vertical migration behavior. Deep-Sea Res. II. 52,193 – 216.

Coyle, K. O., Pinchuk, A. I., 2003. Annual cycle of zooplankton abundance, biomass and production on the northern Gulf of Alaska shelf, October 1997 through October 2000. Fish. Oceanogr. 12, 327-338.

Crawford, W. R., Brickley, P. J., Thomas, A. C. 2007. Mesoscale eddies dominate surface phytoplankton in the northern Gulf of Alaska. Prog. Oceanogr. 75, 287-303.

Cross, J. N., Mathis, J. M., Lomas, M. W., Moran, S. B., Baunmann, M. S., Shull, D. H., Mordy, C. W., Ostendorf, M. L. et al., 2014. Integrated assessment of the carbon budget in the southeastern Bering Sea. Deep-Sea Res. II. 109, 112-124.

Crusius, J., Schroth, A. W., Resing, J. A., Cullen, J., Campbell, R. W., 2017. Seasonal and spatial variabilities in the northern Gulf of Alaska surface water iron concentrations driven by shelf sediment resuspension, glacial meltwater, a Yakutat eddy, and dust. Glob. Biogeochem. Cyc. 32, 942-960.

Crusius, J., Schroth, A. W., Gasso, S., Moy, C. M., Levy, R. C., Gatica, M., 2011. Glacial flour dust storms in the Gulf of Alaska: hydrologic and meteorological controls and their importance as a source of bioavailable iron. Geophys. Res. Let. 38, L06602

Dagg, M. J., Liu, H., Thomas, A. C., 2006. Effects of mesoscale phytoplankton variability on the copepods *Neocalanus flemingeri* and *N. plumchrus* in the coastal Gulf of Alaska. Deep-Sea Res. I. 53, 321-332.

Dagg, M., Strom, S., Liu, H. 2009. High feeding rates on large particles by *Neocalanus flemingeri* and *N. plumchrus*, and consequences for phytoplankton community structure in the subarctic Pacific Ocean. Deep-Sea Res. I. 56, 716-726.

Dickson, D. M. S., Baker, M. R. 2016. Introduction to the North Pacific Research Board Gulf of Alaska Integrated Ecosystem Research Program (GAOIERP): Volume 1. Deep-Sea Res. II, 132, 1-5.

Dai, A., T. Qian, K. E. Trenberth, and J. D Milliman, 2009: Changes in continental freshwater discharge from 1948-2004. J. Climate. 22, 2773-2791.
http://www.cgd.ucar.edu/cas/catalog/surface/dai-runoff/index.html

Danielson, S. L., Dobbins, E. L., Jakobsson, M., Johnson, M. A., Weingartner, T. J., Williams, W. J., Zarayskaya, Y., 2016. Sounding the northern seas, Eos, 96, doi:10.1029/2015EO040975

Danielson, S., Curchitser, E., Hedstrom, K., Weingartner, T., Stabeno, P., 2011. On ocean and sea ice modes of variability in the Bering Sea. J. Geophys. Res. 116, C12034, doi:10.1029/2011JC007389.

Dobbins, E. L., Hermann, A. J., Stabeno, P. J., Bond, N. A., Steed, R. C., 2009. Modeled transport of freshwater from a line-source in the coastal Gulf of Alaska. Deep-Sea Res. II, 56, 2409-2426.

Doyle, M. J., Mier, K., 2016. Early life history pelagic exposure profiles of selected commercially important fish species in the Gulf of Alaska. Deep-Sea Res. II, 132, 162-193.

Egbert, G. D., and S. Y. Erofeeva., 2002. Efficient inverse modeling of barotropic ocean tides. J. Atm. Oceanic Tech. 19, 183-204.

Egbert, G. D., Bennett, A. F., Foreman, M. G. G., 1994. TOPEX/Poseidon tides estimated using a global inverse model. J. Geophys. Res. Oceans, 99, 24821-24852, https://doi.org/10.1029/94JC01894.

Fennel, K., Abbott, M. R., Spitz, Y, H., Richman, J. G., Nelson, D. M. 2003. Impacts of iron control on phytoplankton in the modern and glacial Southern Ocean. Deep-Sea Res. II, 50, 833-851.

Geider, R. J., MacIntyre, H. L., Kana, T. M., 1997. Dynamic model of phytoplankton growth and acclimation: responses of the balanced growth rate and the chlorophyll *a*:Carbon ratio to light, nutrient-limitation and temperature. Mar. Ecol. Prog. Ser. 148, 187-200.

Haidvogel, D.B., Arango, H., Budgell, W.P., Cornuelle, B.D., Curchitser, E., Di Lorenzo, E., Fennel, K., Geyer, W.R., Hermann, A.J., Lanerolle, L., Levin, J., McWilliams, J. C., Miller, A. J., Moore, A.M., Powell, T.M., Shchepetkin, A.F., Sherwood, C.R., Signell, R.P., Warner, J.C., Wilkin, J., 2008. Regional Ocean Forecasting in Terrain-following Coordinates: Model Formulation and Skill Assessment. J. Comput. Phys. 227, 3595-3624.

Haidvogel, D. B., Arango, H., Hedstrom, K., Beckmann, A., Malanotte-Rizzoli, P., and Shchepetkin, A., 2000. Model evaluation experiments in the North Atlantic Basin: Simulations in non-linear terrain-following coordinates. Dyn. Atm. Ocean. 32, 239-281.

Henson, S. A., 2007. Water column stability and spring bloom dynamics in the Gulf of Alaska. J. Mar. Res. 65, 715-736.

Hermann, A. J., Curchitser, E. N., Haidvogel, D. B., Dobbins, E. L., 2009a. A comparison of remote versus local influence of El Nino on the coastal circulation of the Northeast Pacific. Deep-Sea Res. II. 56, 2427-2443.

Hermann, A.J., Hinckley, S., Dobbins, E. L., Haidvogel, D. B., Bond, N. A., Mordy, C., Kachel, N., Stabeno, P. J., 2009b. Quantifying cross-shelf and vertical nutrient flux in the Gulf of Alaska with a spatially nested, coupled biophysical model. Deep-Sea Res. II. 56, 2474-2486.

Hermann, A. J., Stabeno, P. J., 1996. An eddy-resolving model of circulation ion the western Gulf of Alaska Shelf: 1. Model development and sensitivity analyses. J. Geophys. Res., 101 (C1), 1129-1149.

Hill, D. F., Bruhis, N., Calos, S. E., Arendt, A. Beamer, J., 2015. Spatial and temporal variability of freshwater discharge into the Gulf of Alaska. J. Geophys. Res. Oceans. 120, 634-646.

Hinckley, S., Coyle, K. O., Gibson, G., Hermann, A. J., Dobbins, E. L., 2009. A biophysical NPZ model with iron for the Gulf of Alaska: Reproducing the differences between an oceanic HNLC ecosystem and a classical northern temperate shelf ecosystem. Deep-Sea Res. II. 56, 2520-2536.

Jassby, A. D., Platt, T. 1976. Mathematical formulation of the relationship between photosynthesis and light for phytoplankton. Limnol. Oceanogr. 21, 540-547.

Kobari, T., Ikeda, T., 2001a. Ontogenetic vertical migration and life cycle of *Neocalanus plumchrus* (Crustacea: Copepoda) in the Oyashio region, with notes on regional variations in body sizes. J. Plankton Res. 23, 287-302.

Kobari, T., Ikeda, T., 2001b. Life cycle of *Neocalanus flemingeri* (Crustacea: Copepoda) in the Oyashio region, western subarctic Pacific, with notes on its regional variations. Mar. Ecol. Prog. Ser. 209, 243-506.

Ladd, C., Cheng, W., Salo, S., 2016. Gap winds and their effects on regional oceanography Part II: Kodiak Island, Alaska. Deep-Sea Res. II. 132, 54-67.

Ladd, C., Cheng, W., 2016. Gap winds and their effects on regional oceanography. Part I: Cross Sound, Alaska. Deep-Sea Res. II. 132, 42-53.

Ladd, C., Crawford, W. R., Harpold, C. E., Johnson, W. K., Kachel, N. B., Stabeno, P. J., Whitney, F., 2009. A synoptic survey of young mesoscale eddies in the Eastern Gulf of Alaska. Deep-Sea Res. II. 56, 2460-2473.

Lam, P., J., Bishop, J. K. M., 2008. The continental margin is a key source of iron to the HNLC North Pacific Ocean. Geophys. Res. Let. 35, L07608

Large, W. G., McWilliams, J. C., Doney, S. C., 1994. Ocean vertical mixing: a review and a model with nonlocal boundary layer parameterization. Rev. Geophys. 32, 363-403.

Large, W.G., Yeager, S.G., 2008. The global climatology of an interannually varying air-sea 1009 flux data set. Clim. Dyn. 33, 341-364

Lippiatt, S. M., Lohan, M. C., Bruland, K. W., 2010. The distribution of reactive iron in the northern Gulf of Alaska coastal waters. Mar. Chem. 121, 187-199.

Liu, H., Hopcroft, R. R., 2006a. Growth and development of *Metridia pacifica* (Copepoda, Calanoida) in the northern Gulf of Alaska. J. Plankton Res. 28, 769-781.

Liu, H., Hopcroft, R. R., 2006b. Growth and development of *Neocalanus flemingeri/plumchrus* in the northern Gulf of Alaska: validation of the artificial cohort method in cold waters. J. Plankton Res. 28, 87-101.

Mackas, D. L., Tsuda, A., 1999. Mesozooplankton in the eastern and western subarctic Pacific: community structure, seasonal life histories, and interannual variability. Prog. Oceanogr. 43, 335-363.

Martin, J. H., Gordon, R. M., Gitzwater, S., Broenkow, W. W., 1989. VERTEX: phytoplankton/iron studies in the Gulf of Alaska. Deep-Sea Res. 36, 649-680.

Moore, A. M., Arango, H.G., DiLorenzo, E., Cornuelle, B.D., Miller, A.J., Neilsen, D. J., 2004. A comprehensive ocean prediction and analysis system based on the tangent linear and adjoint of a regional ocean model. Ocean Modeling **7**, 227-258.

Morel, A., 1988. Optical modeling of the upper ocean in relation to its biogenous matter content (case 1 water). J. Geophys. Res., C. Oceans. 93(C9), 10749-10768.

Morel, F. M. M., Milligan, A. J., Saito, M. A., 2003. Marine Bioinorganic Chemistry: the role of trace metals in the oceanic cycles of major nutrients. In: Treatise on Geochemistry, Elsevier Ltd. Volume 6, pp. 113-143.

Neilands, J. B., 1995. Siderophores: structure and function of microbial iron transport compounds. J. Biol. Chem. 270, 26723-26726.

Okkonen, S. R., Weingartner, T. J., Danielson, S. L., Musgrave, D. L., Schmidt, G. M., 2003. Satellite and hydrographic observations of eddy-induced shelf-slope exchange in the northwestern Gulf of Alaska. J. Geophys. Res. 108(C2), 3033, doi:10.1029/2002JC001342

Parsons, T. R., Takahashi, M., Hargrave, B., 1988. Biological Oceanographic Processes, 3rd edition. Pergamon Press, Inc., Maxwell House, Fairview Park, Elmsform, New York 10523 USA (330 pp.)

Perry, M. J., Bolger, J. P., English, D. C., 1989. Primary production in Washington coastal waters. In: Landry, M. R., Hickey, B. M. (eds), Coastal Oceanography of Washington and Oregon. Elsevier Press, New York, pp. 117-138.

Pikitch, E.K., Santora, C., Babcock, E.A., Bakun, A., Bonfil, R., Conover, D.O., Dayton, P., Doukakis, P., Fluharty, D., Heneman, B., Houde, E.D., Link, J., Livingston, P.A., Mangel, M., McAllister, M.K., Pope, J., Sainsbury, K.J., 2004. Ecosystem-based fishery management. Science, 305, 346–347. doi:10.1126/science.1098222. PMID:15256658.

Reed, R. K., 1984. Flow of the Alaskan Stream and its variations. Deep-Sea Res. 31, 369-386.

Roncalli, V., Cieslak, M. C., Sommer, S. A., Hopcroft, R. R., Lenz, P. H., 2018. *De no*vo transcriptome assembly of the calanoid copepod *Neocalanus flemingeri*: a new resource for emergence from diapause. Mar. Genomics 37, 114-119.

Roncalli, V., Cieslak, M., Hopcroft, R., Lenz, P. Cost of reproduction: physiological trade-offs in the subarctic copepod *Neocalanus flemingeri* after diapause. Proc. Royal Soc. B. In review.

Royer, T. C., 1998. Coastal processes in the northern North Pacific. In: Robinson, A. R., Brink, K. H. (Eds.). The Sea. Ideas and observations on progress in the study of the seas. Vol. 11. The Global Ocean: Regional Studies and Synthesis. Wiley, New York, pp. 395-414.

Royer, T. C., 2019. NPRB Project Report 734**,** http://projects.nprb.org/#metadata/3825fa51-deae-4069-99b3-1f29e13a66bd/project

Saha, S. and coauthors, 2010. The NCEP Climate Forecast System Reanalysis. Bull. Amer. Meteor. Soc. 91, 1015.1057. doi: 10.1175/2010BAMS3001.1

Sambrotto, R, N., Lorenzen, C. J., 1986. Phytoplankton and primary production. In: Hood, W. D., Zimmerman, S. T. (eds). The Gulf of Alaska. US Department of Commerce, USA, pp. 249-282.

Schroth, A. W., Crusius, J., Hoyer, I., Campbell, R. 2014. Estuarine removal of flacial iron and implications for iron fluxes to the ocean. Geophys. Res. Let. 41, 3951-3958.

Shchepetkin, A.F., McWilliams, J.C., 2004. The Regional Ocean Modeling System: A split-explicit, free-surface, topography-following coordinate ocean model. Ocean Modeling 9, 347-404.

Stabeno, P. J., Bond, N. A., Hermann, A. J., Kachel, N. B., Mordy, C. W., Overland, J. E., 2004. Meteorology and oceanography of the Northern Gulf of Alaska. Cont. Shelf Res. 24, 859-897.

Strom, S. L., Fredrickson, K. A., Bright, K. J., 2016. Spring phytoplankton in the eastern coastal Gulf of Alaska: photosynthesis and production during high and low bloom years. Deep-Sea Res. II. 132, 107-121.

Strom, S. L., Olson, M. B., Macri, E. L., Mordy, C. W., 2006. Cross-shelf gradients in phytoplankton community structure, nutrient utilization and growth rate in the coastal Gulf of Alaska. Mar. Ecol. Prog. Ser. 328, 75- 92.

Strom, S. L., Macri, E. L., Fredrickson, K. A., 2010. Light limitation of the summer primary production in the coastal Gulf of Alaska: physiological and environmental causes. Mar. Ecol. Prog. Ser. 402, 45-57.

Styles, R., Glenn, S.M., 2002. An optimized combined wave and current algorithm for arbitrary bed roughness. Technical Report R829424E02, Coastal Physical Oceanography Laboratory, Department of Geological Science, University of South Carolina, Columbia.

Sunda, W. G., 1997. Control of dissolved iron concentration in the world ocean: a comment. Mar. Chem. 57, 169-172.

Tsuda, A., Saito, H., Kasai, H., 1999. Life histories of *Eucalanus bungii* and *Neocalanus cristatus* (Copepoda: Calanoida) in the western subarctic Pacific. Mar. Biol. 135, 533-544.

Vaz, R. A. N., Simpson, J. H., 1994. Turbulence closure modeling of estuarine stratification. J. Geophys. Res. Oceans 99, 16143-16160.

Waite, J. N., Mueter, F. J., 2013. Spatial and temporal variability of chlorophyll-*a* concentrations in the coastal Gulf of Alaska, 1998-2011, using cloud-free reconstructions of SeaWiFS and MODIS-Aqua data. Prog. Oceanogr. 116, 179-192.

Walsh, J. J., McRoy, C. P., 1986. Ecosystem analysis in the southeastern Bering Sea. Cont. Shelf Res. 5, 259-299.

Wang, Y., Xue, H., Chai, F., Chao, Y., Farrara, J., 2014. A model study of the Copper river plume and its effect on the northern Gulf of Alaska. Ocean Dyn. 64, 241-258.

Weingartner, T. J., Coyle, K., Finney, B., Hopcroft, R., Whitledge, T., Brodeur, R., Dagg, M., Farley, M., Haidvogel, D., Haldorson, L., Hermann, A., Hinkley, S., Napp, J., Stabeno, P., Kline, T., Lee, C., Lessard, E., Royer, T., Strom, S., 2002. The Northeast Pacific GLOBEC Program: Coastal Gulf of Alaska. Oceanography 15, 48-63.

Weingartner, T. J., Danielson, S., Royer, T. C., 2005. Freshwater variability and predictability in the Alaska Coastal Current. Deep-Sea Res. II. 52, 169-191.

Westbury, T. K., Schultz, P., Behrenfeld, M. J., Dunne, J. P., Hiscock, M. R., Maritorena, S., Sarmiento, J. L., Siegel, D. A., 2016. Annual cycles of phytoplankton biomass in the subarctic Atlantic and Pacific Ocean. Global Biogeochem. Cycles, 30, 175-190.

World Ocean Atlas, 2013. https://www.nodc.noaa.gov/cgi-bin/OC5/woa13fv2/woa13oxnufv2.pl

Wu, J., Aguila-Islas, A., Rember, R., 2009. Size-fractionated iron distribution on the northern Gulf of Alaska. Geophys. Res. Let. 36, L11606, doi:10.1029/2009GL038304

Table 1. Parameter setting for computation of carbon chlorophyll ratios. PhS = small phyto component, PhL = large phytoplankton component.

Parameter	PhS	PhL	Description	Units
θ_m	0.024	0.0555	Maximum chlorophyll:carbon ratio	None
P_m^C	2.24e-5	3.27e-5	Carbon specific light saturated photosynthetic rate	s^{-1}
α^{chl}	0.83e-5	0.58e-5	Chlorophyll-*a* specific initial slope of the phytosynthesis-light curve	g C g^{-1} chl m^2 μmol^{-1} photons

Table 2. ANOVA comparing variables by season and year group (2000-2006 and 2007 – 2013): primary production (g C m^{-2} (time period)$^{-1}$), iron concentration (nM), iron area (fraction of total polygon area), omega to 100 m (m^3 s^{-1} e-5); P1-P7 refers to Polygons 1 through 7, respectively. Significant P values are bolded.

Variable	2000-2006 mean	2007-2013 mean	P
A: Primary production			
P1, Primary Production, March - May	69.6	59.3	**0.00003**
P1, Primary Production, September - October	51.9	47.3	0.08
P2, Primary production, March - May	38.9	32.9	**0.00001**
P2, Primary production, September - October	33.9	29.7	0.09
P4, Primary production, March - May	79.4	71.1	**0.03**
P4, Primary production, September - October	52.1	44.6	**0.02**
P5, Primary production, March - May	43.3	36.9	**0.002**
P5, Primary production, September - October	32.0	28.9	0.211
P7, Primary production, March - May	59.9	51.7	**0.0000**
P7, Primary production, September - October	52.1	45.1	**0.02**
B: Iron Concentration			
P1, Iron Concentration, March - May	2.966	2.754	**0.036**
P1, Iron Concentration, September - October	3.807	3.453	**0.001**
P2, Iron Concentration, March - May	0.459	0.414	**0.035**
P2, Iron Concentration, September - October	0.380	0.335	0.059
P4, Iron Concentration, March - May	0.961	0.892	0.095
P4, Iron Concentration, September - October	2.76	2.91	0.416
P5, Iron Concentration, March - May	0.451	0.399	**0.020**
P5, Iron Concentration, September - October	0.452	0.418	0.373
P7, Iron Concentration, March - May	0.964	0.833	**0.0007**
P7, Iron Concentration, September - October	1.897	1.597	**0.027**
C: Iron Area			
P1, Iron Area, March - May	0.840	0.732	**0.003**
P1, Iron Area, September - October	0.805	0.695	**0.001**
P2, Iron Area, March - May	0.197	0.072	**0.02**
P2, Iron Area, September - October	0.139	0.059	0.086
P4, Iron Area, March - May	0.687	0.572	**0.023**
P4, Iron Area, September - October	0.915	0.925	0.636
P5, Iron Area, March - May	0.262	0.123	**0.034**
P5, Iron Area, September - October	0.315	0.245	0.271
P7, Iron Area, March - May	0.668	0.465	**0.001**
P7, Iron Area, September - October	0.694	0.526	**0.003**

Table 2 (continued)			
Variable	**2000-2006 mean**	**2007-2013 mean**	**P**
D: Omega			
P1, Omega, March - May	-4.00	-5.71	0.281
P1, Omega, September - October	0.563	-2.284	**0.047**
P2, Omega, March - May	0.130	-0.741	0.340
P2, Omega, September - October	2.463	3.138	0.538
P4, Omega, March - May	-0.657	-0.763	0.413
P4, Omega, September - October	-3.954	-4.682	0.523
P5, Omega, March - May	-2.252	-0.007	0.747
P5, Omega, September - October	1.464	-0.224	0.149
P7, Omega, March - May	-5.236	-5.838	0.351
P7, Omega, September - October	2.347	0.704	0.118

Table 3. Iterative multiple regressions of simulated dissolved iron concentration in Polygons 1 and 4 during March-May and September-October. Om = omega (vertical momentum flux), HR is Hill Runoff; P1 and P4 are Polygons 1 and 4 respectively; MM, JF, Fl and Su are March-May, January-February, September-October and June-August, respectively. R_a^2 = adjusted R^2, P is the regression P value, C = correlation coefficient (bolded values are significant).

A: March-May

Variable	**P1**			**Variable**	**P4**		
	R_a^2	**P**	**C**		R_a^2	**P**	**C**
OmP1MM	-0.082	0.925	-0.028	OmP4MM	0.033	0.252	0.328
OmP1JF	-0.105	0.697	0.249	OmP4JF	-0.040	0.495	-0.059
HRP1MM	-0.207	0.854	0.005	HRP4MM	**0.345**	0.067	**0.587**
HRP1JF	-0.017	0.480	0.339	HRP4JF	**0.485**	**0.038**	0.368
OmP2MM	0.032	0.435	0.292	OmP5MM	0.432	0.082	-0.359
OmP2JF	-0.103	0.601	0.093	OmP5JF	0.366	0.155	0.228
HRP1Fl	-0.277	0.744	-0.016	HRP4Fl	0.279	0.234	-0.036
HRP1Su	-0.251	0.705	0.387	HRP4Su	**0.526**	0.135	-0.212
OmP1Fl	0.038	0.520	0.467	OmP4Fl	0.446	0.238	0.294
OmP1Su	-0.001	0.568	0.244	OmP4Su	0.263	0.418	0.234
OmP2Fl	-0.448	0.750	-0.372	OmP5Fl	**0.933**	0.054	**0.645**
OmP2Su	-1.889	0.911	0.098	OmP5Su	0.892	0.243	0.054

B: Seasonal comparison, spring (March-May)

Variable	**P1**			**Variable**	**P4**		
	R_a^2	**P**	**C**		R_a^2	**P**	**C**
FeP1JF	**0.963**	**0.000**	**0.983**	FeP4JF	**0.313**	**0.022**	**0.605**
FeP1Fl	**0.961**	**0.000**	**0.872**	FeP4Fl	0.270	0.070	-0.082
FeP1Su	**0.967**	**0.000**	**0.696**	FeP4Su	**0.630**	**0.004**	0.486

C: September-October

Variable	**P1**			**Variable**	**P4**		
	R_a^2	**P**	**C**		R_a^2	**P**	**C**
OmP1Fl	0.179	0.074	-0.492	OmP4Fl	**0.269**	**0.033**	**0.570**
OmP1Su	0.105	0.216	-0.231	OmP4Su	0.214	0.106	-0.239
HRP1Fl	0.034	0.374	-0.156	HRP4Fl	**0.738**	**0.001**	-0.387
HRP1Su	0.001	0.453	-0.117	HRP4Su	**0.779**	**0.001**	**0.578**
OmP2Fl	**0.374**	0.114	0.492	OmP5Fl	0.770	**0.003**	0.008
OmP2Su	0.317	0.193	0.231	OmP5Su	0.743	**0.010**	0.265
HRP1MM	0.283	0.260	0.334	HRP4MM	0.701	**0.029**	-0.052
HRP1JF	0.202	0.300	0.357	HRP4JF	**0.745**	**0.035**	-0.358
OmP1MM	0.155	0.440	0.035	OmP4MM	0.698	0.086	0.064
OmP1JF	**0.557**	0.230	0.194	OmP4JF	**0.960**	**0.022**	0.214
OmP2MM	0.286	0.421	0.383	OmP5MM	0.919	0.067	-0.114
OmP2JF	-0.162	0.701	-0.184	OmP5JF	0.858	0.278	0.126

D: Seasonal comparison; September-October

Variable	**P1**	**Variable**	**P4**

	R_a^2	P	C		R_a^2	P	C
FeP1-4Su	**0.786**	**0.000**	**0.895**	FeP4Su	0.212	0.055	0.523
FeP1-4MM	**0.801**	**0.000**	**0.696**	FeP4MM	**0.316**	**0.049**	-0.082
FeP1-4JF	**0.824**	**0.000**	**0.539**	FeP4JF	**0.406**	**0.042**	0.076

Table 4. Iterative multiple regressions of simulated iron concentration in Polygon 7 during March-May and September-October. Om = omega (vertical momentum flux); Hr = Hill runoff; Flx = advection into Polygon 7 from the adjacent basin; FeHor = horizontal iron flux into P7; FeDif = vertical diffusion of iron through the pycnocline; MM, JF, Fl and Su are March-May, January-February, September-October and June-August, respectively. R_a^2 = adjusted R^2, P is the regression P value, C = correlation coefficient (bolded values are significant).

A. Multiple Regression and Correlation

Variable	March-May			Variable	September-October		
	R_a^2	P	C		R_a^2	P	C
OmP7MM	0.002	0.33	0.28	OmP7Fl	**0.491**	**0.003**	**0.73**
OmP7JF	-0.03	0.46	0.24	OmP7Su	0.484	**0.010**	0.40
HRP7MM	-0.12	0.66	0.02	HRP7Fl	**0.579**	**0.01**	-0.29
HRP7JF	**0.09**	0.33	0.33	HRP7Su	**0.633**	**0.01**	0.25
OmP2MM	**0.26**	0.20	0.25	OmP2Fl	**0.66**	**0.01**	-0.45
OmP2JF	0.16	0.33	0.24	OmP2Su	0.62	**0.03**	-0.13
HRP7Fl	0.14	0.38	0.32	HRP7MM	**0.65**	**0.04**	0.42
HRP7Su	0.03	0.50	0.13	HRP7JF	0.59	0.10	0.21
OmP2Fl	-0.17	0.65	-0.49	FlxFl	0.57	0.16	-0.43
FlxFl	**0.912**	**0.025**	**-0.66**	FeHorFl	**0.98**	**0.00**	**-0.62**
FeHorMM	**0.999**	**0.003**	**0.72**	FeDifFl	0.98	**0.02**	**0.57**

B. Comparisons Between Seasons

Variable	March-May			Variable	September-October		
	R_a^2	P	C		R_a^2	P	C
FeP7JF	**0.389**	**0.010**	**0.660**	FeP7Su	0.222	0.051	0.531
FeP7Fl	**0.455**	**0.014**	**0.828**	FeP7MM	**0.413**	0.053	**0.623**
FeP7Su	**0.884**	**0.000**	**0.623**	FeP7JF	**0.794**	**0.000**	**0.802**

Table 5. Iterative multiple regressions of simulated iron concentration in oceanic Polygons 2 during March-May and September-October. Om = omega (vertical momentum flux); Flx = advection into Polygon 7 from the adjacent basin; Fe = Iron concentration; P2 and P5 are Polygons 2 and 5 respectively; MM, JF, Fl and Su are March-May, January-February, September-October and June-August, respectively. R_a^2 = adjusted R^2, P is the regression P value, C = correlation coefficient (bolded values are significant).

A: March-May				**C: September-October**			
Variable	R_a^2	**P**	**C**	**Variable**	R_a^2	**P**	**C**
OmP2MM	-0.080	0.851	0.055	OmP2Fl	-0.079	0.830	0.063
OmP2JF	-0.123	0.757	0.221	OmP2Su	0.162	0.151	-0.522
OmP1MM	0.009	0.415	0.470	OmP1Fl	0.201	0.165	0.281
OmP1JF	**0.798**	**0.001**	**0.729**	OmP1Su	0.116	0.301	-0.051
OmP2Fl	**0.804**	**0.002**	0.247	OmP2MM	0.025	0.445	-0.137
OmP1Fl	0.776	**0.006**	0.493	OmP1MM	-0.109	0.607	0.164
OmP2Su	**0.891**	**0.002**	-0.310	OmP2JF	0.218	0.314	-0.430
OmP1Su	0.884	**0.005**	0.182	OmP1JF	**0.607**	0.091	0.433
FlxP7MM	**0.889**	**0.013**	**-0.606**	FlxP7Su	**0.659**	0.106	-0.398
FlxP7Fl	**0.912**	**0.025**	-0.330	FlxP7MM	**0.932**	**0.017**	-0.492
FlxP7Su	**0.981**	**0.015**	-0.141	-	-	-	**-**
B: Seasonal comparison, March-May				**D: Seasonal comparison, September - October**			
Variable	R_a^2	**P**	**C**	**Variable**	R_a^2	**P**	**C**
FeP2-5JF	**0.900**	**0.000**	**0.953**	FeP2Su	**0.447**	**0.005**	**0.700**
FeP2-5Fl	**0.892**	**0.000**	**0.645**	FeP2MM	0.428	**0.018**	**0.645**
FeP2-5Su	**0.939**	**0.000**	**0.775**	FeP2JF	**0.476**	**0.023**	**0.640**

Table 6. Iterative multiple regressions of simulated iron concentration in oceanic Polygons 5 during March-May and September-October. Om = omega (vertical momentum flux); Fe = Iron concentration; P2 and P5 are Polygons 2 and 5 respectively; MM, JF, Fl and Su are March-May, January-February, September-October and June-August, respectively. R_a^2 = adjusted R^2, P is the regression P value, C = correlation coefficient (bolded values are significant).

A: March-May				**C: September-October**			
Variable	R_a^2	**P**	**C**	**Variable**	R_a^2	**P**	**C**
OmP5MM	-0.041	0.497	0.198	OmP2Fl	0.107	0.135	0.419
OmP5JF	**0.227**	0.242	0.405	OmP2Su	0.035	0.328	0.094
OmP4MM	**0.268**	0.111	0.443	OmP1Fl	0.099	0.280	0.128
OmP4JF	0.228	0.185	0.211	OmP1Su	**0.238**	0.176	0.149
OmP5Fl	**0.241**	0.214	0.205	OmP2MM	0.171	0.280	-0.226
OmP4Fl	**0.321**	0.119	0.529	OmP1MM	0.313	0.195	0.290
OmP5Su	0.235	0.299	0.256	OmP2JF	0.199	0.330	0.174
OmP4Su	0.087	0.467	**-0.647**	OmP1JF	0.134	0.420	-0.127
B: Seasonal comparison, March-May				**D: Seasonal comparison, September - October**			
Variable	R_a^2	**P**	**C**	**Variable**	R_a^2	**P**	**C**
FeP5JF	**0.607**	**0.001**	**0.799**	FeP5Su	**0.238**	**0.044**	**0.545**
FeP5Fl	0.578	**0.003**	0.195	FeP5MM	0.218	0.103	0.195
FeP5Su	0.539	**0.013**	-0.012	FeP5JF	0.189	0.177	0.328

Table 7. Simulated and measured chlorophyll concentration, C-Chl ratios, growth rate, carbon biomass and productivity from the northern Gulf of Alaska; simulation outputs are means and medians from Polygon 1. Measured values are from the southwestern, southeastern and south-central Alaskan shelf.

Variable	Simulated Value	Measured Value	Source
A. Chlorophyll concentration at depth of chlorophyll maximum (mg m^{-3})	0.8-2.2 @ ~10 m depth; April-May	0.63-1.33 @ 15-25 m depth	Strom et al. (2006)
B. Maximum chlorophyll concentrations (mg m^{-3}).	Maximum water column averages 0 - 10	<2 to 10	2011 and 2013, from Strom et al. (2016)
C. C-Chl ratios on Seward Line	19 - 73	19 - 110; Mar - Dec; 2001 & 2002	Coyle et al. (2012)
D. Median C-Chl ratios, large cells	26 (range: 19-33) March-May	April Median 2013: 41 Range 2011 & 2013: 15-311 (median: 54)	Strom et al. (2016)
E. Median C-Chl ratios, small cells	59 (range: 42-73) March-May	May Median 2011: 76	Strom et al. (2016)
F. Maximum integrated Chl to 50 m depth (mg m^{-2})	Median: 25.5, range: 86 – 2568; March-May	11-302	Strom et al. (2016)
G. Carbon biomass; small cells (mg C m^{-3})	4-11 (mean in upper 25 m); March-May	48-74; range: 17-181; April-May	Strom et al. (2016)
H. Median growth rate (d^{-1})	0.33 – 1.43	0.18 – 1.3	Strom et al. (2016)
I. Productivity (g C m^{-2} d^{-1})	March-May Maximum: 0.6-14.8; Median: 0.43	May 2011 Median: 0.9 Apr 2013 Median: 2.5 Range: 0.36 – 4.87	Strom et al. (2016)

Table 8. Chlorophyll concentrations from satellite measurements (Waite and Mueter, 2013) and mean simulated chlorophyll concentration in the upper 10 m (mg m^{-3}). Simulated means are the maximum and minimum mean daily values for the whole polygon for the time period during 2000 and 2013. Simulated ranges are the maximum and minimum values for any point in the polygon for any day in 2000 and 2013.

	May (bloom peak)		**Summer**		**Fall (bloom peak)**	
	Satellite	**Simulation**	**Satellite**	**Simulation**	**Satellite**	**Simulation**
Polygon 4 mean	1.62	4.8-17.9	0.69	0.21-1.5	1.10	0.21-1.9
Range	± 1.36	0.02-32.0	± 0.16	0.01-45.6	± 1.15	0.01-18.6
Polygon 1 mean	2.74	0.47-1.28	0.97	0.45-2.61	1.86	0.49-1.13
Range	± 1.41	0.00-39.9	± 0.11	0.00-30.0	± 1.18	0-26.8
Polygon 2 mean	1.32	3.2-5.3	0.37	0.33-0.94	0.8	0.43-0.85
Range	± 1.57	0.1-23.5	± 0.09	0.1-28.1	± 1.25	0.23-10.2

Table 10. Iterative multiple regressions of simulated primary production for basin polygons during March-May and September-October. Variable symbols: FeA, Fe, Par and NO_3 are iron area, iron concentration, PAR and nitrate concentration respectively; P followed by a digit is the polygon number; MM and Fl designate March-May and September-October respectively; R_a^2 is the adjusted R^2; P is the regression probability; C is the correlation coefficient of primary production to the variable (bolded values are significant).

A: March-May

Variable	**P2**			**Variable**	**P5**		
	R_a^2	**P**	**C**		R_a^2	**P**	**C**
FeAMM	**0.650**	**0.000**	**0.823**	FeAMM	**0.666**	**0.000**	**0.832**
FeMM	0.619	**0.002**	**0.760**	FeMM	0.652	**0.001**	**0.809**
ParMM	**0.737**	**0.001**	**0.634**	ParMM	**0.926**	**0.000**	0.362
NO_3MM	**0.884**	**0.001**	-0.0727	NO_3MM	0.925	**0.000**	-0.269

B: September-October

Variable	**P2**			**Variable**	**P5**		
	R_a^2	**P**	**C**		R_a^2	**P**	**C**
FeAFl	**0.669**	**0.000**	**0.833**	FeAFl	**0.703**	**0.000**	**0.852**
FeFl	**0.809**	**0.000**	**0.912**	FeFl	0.695	**0.001**	**0.837**
ParFl	0.797	**0.000**	0.211	ParFl	**0.842**	**0.000**	0.473
NO_3Fl	**0.865**	**0.000**	**-0.682**	NO_3Fl	0.823	**0.001**	**-0.646**

Table 11. Statistical analyses by year group of carbon biomass of net-caught copepods along the Seward Line in May (A, B) and September-October (C, D), 2000-2013. Group 1 = 2000-2006; Group 2 = 2007 – 2013. (A, C) Mann-Whitney nonparametric test; (B, D) Analysis of variance, parametric test. DF is degrees of freedom. Bolded = significant, P < 0.05.

A. Mann-Whitney	Species	Adjusted Z	p-level	Valid N Group 1	Valid N Group 2
	Neocalanus	1.5972	0.112	7	7
	Calanoida	2.4916	**0.013**	7	7
B. ANOVA	Species	SS	p-level	DF	F
	Neocalanus	0.213	**0.0296**	12	6.090
	Calanoida	0.250	**0.009**	12	9.843
C. Mann-Whitney	Species	Adjusted Z	p-level	Valid N Group 1	Valid N Group 2
	Calanoida	-0.319	0.749	7	7
	Cyclopoida	-1.980	0.050	7	7
D. ANOVA	Species	SS	p-level	DF	F
	Calanoida	4.037	0.386	12	12
	Cyclopoida	0.230	0.065	12	12

Table 12. Regression analysis comparing copepod carbon biomass (mg m^{-3}) from net tows along the Seward Line in May 2000 - 2013 and simulated production (g C m^{-2}) for March-May 2000 - 2013 in Polygon 7. The P value is the regression probability; P ≤ 0.05 is considered significant and is set in boldface type.

Analysis Description	**R**	**R^2**	**Adjusted R^2**	**P**
Primary Production vs Calanoid Carbon Biomass	0.805	0.647	0.615	**0.001**
Copepod Production vs Calanoid Carbon Biomass	0.715	0.511	0.466	**0.006**
Primary Production vs Neocalanus Carbon Biomass	0.660	0.436	0.385	**0.014**
Copepod Production vs Neocalanus Carbon Biomass	0.551	0.304	0.240	0.051

Table 13. Regression analysis comparing copepod carbon biomass from net tows along the Seward Line in September-October 2000 - 2013 and simulated production for August-October 2000 - 2013 in Polygon 7. The P value is the regression probability; P ≤ 0.05 is considered significant and is set in boldface type.

Analysis Description	**R**	**R^2**	**Adjusted R^2**	**P**
Primary Production vs Total Copepod Biomass	0.161	0.026	-0.055	0.581
Copepod Production vs Total Copepod Biomass	0.022	0.001	-0.082	0.939

Figure Captions

Fig. 1. Model grids for the CGOA simulations (A). Diagram of the GOANPZ model (B). Stations along the Seward Line routinely sampled for the Long Term Observation program (C).

Fig. 2. Analysis polygons: western GOA shelf including Polygon 7 east to 147°W (Polygon 1), western GOA off the shelf break (Polygon 2), the southeastern shelf to 147°W (Polygon 4), oceanic region off Polygon 4 (Polygon 5) , western shelf from 156°W to 145°W, overlapping Polygon 1 (Polygon 7, gray boundary). PWS = Prince William Sound. Shelf break is the southern boundary of Polygons 1, 4 and 7.

Fig. 3. Photosynthetic response curves to light from field measurements by Strom et al. (2016) (A), and as computed from Geider et al (1997) (B). P_{max} is the maximum photosynthetic rate at light saturation. Upper axis is equivalent light intensity in model units.

Fig. 4. Daily Runoff on the western Gulf of Alaska shelf from 2000 to 2013 according to the Hill model (Hill et al. 2015). Red line: daily runoff; point values: mean monthly runoff for April and May. The amount of fresh water flowing onto the western shelf in $m^3\ s^{-1}$ is ~1.15e8 X plotted values.

Fig. 5. Mean simulated salinity in the upper 25 m at the inner Seward Line stations. Climatology (A), for a late runoff year (B), for an early runoff year (C). Dots are mean salinity in the upper 25 m from CTD casts. Simulated dissolved iron concentration in the upper 25 m: Climatology (D), for a late runoff year (E), for an early runoff year (F).

Fig. 6. Mean simulated salinity in the upper 25 m at the outer Seward Line stations. Climatology (A), for individual years (B, C). Dots are mean salinity in the upper 25 m from CTD casts. Simulated iron concentration in the upper 25 m: Climatology (D), for individual runoff years (E, F).

Fig. 7. Flow through Shelikof Strait for model runs using the Hill and Royer runoff.

Fig. 8. Climatology of the seasonal distribution of simulated iron concentration (nM) in the upper 25 m for 2000-2013. January-February (A); March-May (B); June-August (C); October-September (D).

Fig. 9. Climatology of the seasonal distribution of simulated nitrate concentration (μM) in the upper 25 m for 2000-2013. January-February (A); March-May (B); June-August (C); October-September (D).

Fig. 10. Comparison of nitrate concentration from FOCI data and model output. FOCI station locations (A); Regression of FOCI nitrate concentration against simulated concentration (B); Map of the climatology (2000 – 2013) of simulated nitrate concentration (μM) in the upper 25 m

for August (C); Climatology of mean nitrate concentration (μM) in the upper 25 m from the World Ocean Atlas for August (D).

Fig. 11. Simulated primary productivity integrated to 30 m depth at Seward Line stations; climatology for 2000-2013 (A), single year for 2006 (B) and for 2010 (C). Boxes list annual simulated production (g C m^{-2} for the plot period) for five stations on the Seward Line; Chlorophyll concentration integrated to 30 m depth; Climatology for 2000-2013 (D); for 2006 (E) and for 2010 (F).

Fig. 12. Total simulated chlorophyll concentration versus the fraction of the large phytoplankton component for a year of high (A and B) and low (C and D) chlorophyll concentration.

Fig. 13. Simulated chlorophyll (A) and phytoplankton carbon (B) depth profile climatologies for April-May in Polygon 1 between 2000 and 2013.

Fig. 14. Climatology (2000-2013) of the seasonal distribution of simulated chlorophyll concentration (mg m^{-2}) in the upper 50 m; January-February (A), March-May (B), June-August (C), September-October (D).

Fig. 15. Climatology of the seasonal distribution of simulated primary production (g C m^{-2}) in the upper 25 m: January February (A); March May (B); June-August (C); September-October (D). Note: color bar in A is 0-15, color bar in B-D is 0-150.

Fig. 16. Simulated mean primary production (A) and calanoid production (B) in Polygon 7 during March and April; calanoid copepod carbon biomass (C), *Neocalanus plumchrus-flemingeri* carbon biomass (D) from net tows taken along the Seward Line in May, red line is the climatology, error bars are 95% confidence intervals.

Fig. 17. Simulated climatology of integrated chlorophyll (solid line) and biomass of *Neocalanus* (bold line) in the upper 25 m in Polygon 1 (A) and Polygon 4 (B). Mean of carbon biomass of *Neocalanus* from net tows in the upper 20 m along the Seward Line during early May from 2000 to 2013 (gray bar, A).

Fig. 18. Simulated mean primary production (A) and calanoid production (B) in Polygon 7 during August-October; calanoid copepod carbon biomass (C), cyclopoid carbon biomass (D) from net tows taken along the Seward Line in August-October, red line is the climatology, error bars are 95% confidence intervals.

Appendix Tables

Table 1. GOANPZ model equations. Advection and diffusion terms are not included.

State Variable	Equation
1) Light Limitation	$Light_{Lim} = \tanh\left(\frac{\alpha' \cdot PAR}{P_{\max}}\right)\left(\frac{\mathrm{Fe}}{k_{feP(i)} + \mathrm{Fe}}\right)$
2) Iron Limitation	$Iron_{Lim} = \frac{\mathrm{Fe}}{k_{feP(i)} + \mathrm{Fe}}$ where i = PS or PL
3) Nitrate Limitation	$NO_{3-Lim} = \frac{\mathrm{NO_3} e^{-\Psi_{PS}\mathrm{NH_4}}}{d_{1PS} + \mathrm{NO_3}}$
4) Nitrate Uptake	$\mathrm{NO}_{3-uptake} = Ph_{(i)} P_{\max} \min\left(\mathrm{Light}_{\mathrm{Lim}}, \left(NO_{3-Lim} Iron_{Lim}\right)\right)$
5) Ammonium Limitation	$NH_{4-\mathrm{lim}} = \frac{\mathrm{NH_4}}{k_{NH_4 P_{(i)}} + \mathrm{NH_4}}$
6) Ammonium Uptake	$NH_{4-uptake} = Ph_{(i)} P_{\max} \min\left(Light_{Lim}, NH_{4-Lim}\right)$
7) Phyto-plankton(i) where i = PS or PL	$\frac{\partial Ph_{(i)}}{\partial t} = Ph_{(i)} + \left(NO_{3-uptake} + NH_{4-uptake}\right)$ $-\sum_{j=1}^{Tot_{P(i)}} \left(e_{Z_{(i,j)}} \left(Q_{10}^{\frac{T - Q10_{Z(i,j)}T}{10}} \right) \left(\frac{f_{pZ_{(i,j)}} Ph_{(i)}}{f_{Z(i)} + \sum_{k=1}^{Tot_{P(j)}} fp_{Pr_{(j,k)}} Pr_{(j,k)}} \right) Z_{(j)} \right)$ $-MAX\left(m_{Ph_{(i)\min}}, m_{Ph_{(i)\max}} - \left(m_{Ph_{(i)\max}} - m_{Ph_{(i)\min}}\right)\right)\left(\frac{\mathrm{NO_3}}{NO_{critPh_{(i)}}}\right) Ph_{(i)}$ $-w_{Ph_{(i)}} Ph_{(i)} - R_{(i)}$ $Ph_{(i)}$ is the phytoplankton component, $Tot_{P_{(i)}}$ is the total number of predators taking $Ph_{(i)}$, $Z_{(j)}$ is predator$_{(j)}$ feeding on $Ph_{(i)}$, $Tot_{P_{(j)}}$ is the total number of prey species for $Z_{(j)}$, j = predator species j of phytoplankton i k = prey species k of predator j.
8) Nitrate	$\frac{\partial \mathrm{NO_3}}{\partial t} = -\xi NO_{3-uptake} + nitr$
9) Ammonium	$\frac{\partial \mathrm{NH_4}}{\partial t} = -\xi\left[NH_{4-uptake} + regen \cdot degrad \cdot D\right] - nitr + E_i$

State Variable	Equation
10) Zooplankton$_{(i)}$ where *i* = MZS, MZL, C, NC or Eup.	$$\frac{\partial Z_{(i)}}{\partial t} = \gamma_{(i)} e_{Z_{(i)}} \left(Q_{10Z_{(i)}}^{\frac{T-Q10_{Z_{(i)}T}}{10}} \right) \left(\frac{\sum_{j=1}^{Tot_P} \left(f_{pZ_{(i,j)}} Pr_{(j)} \right)}{f_{Z(i)} + \sum_{j=1}^{Tot_{P_{(j)}}} fp_{Pr_{(j,k)}} Pr_{(j,k)}} \right) Z_{(i)}$$ $$- \sum_{j=1}^{Tot_{P_{(i)}}} \left(e_{Z_{(j)}} \left(Q_{10Z_{(j)}}^{\frac{T-Q10_{Z_{(i,j)}T}}{10}} \right) \left(\frac{f_{pZ_{(i,j)}} Z_{(i)}}{f_{Z(j)} + \sum_{k=1}^{Tot_{P_{(j)}}} fp_{Pr_{(j,k)}} Pr_{(j,k)}} \right) Z_{(j)} \right) - R_{(i)} - M_{(}
11) Detritus	$$\frac{\partial D}{\partial t} = (1-\gamma_{MZS}) e_{MZS} \left(Q_{10MZS}^{\frac{Temp-Q_{10MZST}}{10}} \right) \left(\frac{fp_{PSMZS} PS}{f_{MZS} + fp_{PSMZS} PS} \right) MZS$$ $$+(1-\gamma_{MZL}) e_{MZL} \left(Q_{10MZL}^{\frac{Temp-Q_{10MZLT}}{10}} \right) \left(\frac{fp_{PSMZS} PS + fp_{PLMZL} PL}{f_{MZL} + fp_{PSMZS} PS + fp_{PLMZL} PL} \right) MZL$$ $$+(1-\gamma_{C}) e_{C} \left(Q_{10C}^{\frac{Temp-Q_{10CT}}{10}} \right) \left(\frac{fp_{PSMZS} PS + fp_{PLC} PL + fp_{MZSC} MZS + fp_{MZLC} MZL}{f_{C} + fp_{PSMZS} PS + fp_{PLC} PL + fp_{MZSC} MZS + fp_{MZLC} MZL} \right)$$ $$+(1-\gamma_{NC}) e_{NC} \left(Q_{10NC}^{\frac{Temp-Q_{10NCT}}{10}} \right) \left(\frac{fp_{PSMZS} PS + fp_{PLNC} PL + fp_{MZSNC} MZS + fp_{MZLNC} M}{f_{NC} + fp_{PSMZS} PS + fp_{PLNC} PL + fp_{MZSNC} MZS + fp_{MZLN}} \right.$$ $$+(1-\gamma_{Eup}) e_{Eup} \left(Q_{10Eup}^{\frac{Temp-Q_{10NCT}}{10}} \right) \left(\frac{fp_{PLEup} PL + fp_{MZSEup} MZS + fp_{MZLEup} MZL + fp_{CE}}{f_{Eup} + fp_{PLEup} PL + fp_{MZSEup} MZS + fp_{MZLEup} MZL + fp} \right.$$ $$+MAX\left(mPS_{\min}, mPS_{\max} - \left(mPS_{\max} - mPS_{\min}\right)\right) \left(\frac{NO_3}{NO_{critPS}} \right) PS$$ $$+MAX\left(mPL_{\min}, mPL_{\max} - \left(mPL_{\max} - mPL_{\min}\right)\right) \left(\frac{NO_3}{NO_{critPL}} \right) PL$$ $$+m_{predC} C^2 + m_{predNC} NC^2 + m_{predEup} Eup^2 - degrad \cdot D - wD \cdot D$$
12) Iron	$$\frac{\partial \mathrm{Fe}}{\partial t} = -f_{ec} \left[\sum_{i=1}^{2} \frac{\partial Ph_{(i)}}{dt} + degrad \cdot D \right]$$

	SubEquations
1) Maximum carbon-specific photosynthetic rate (mg C/mg C/day)	$P_{\max} = (2^D - 1)$
2) Doubling Rate (D)	$D = Di_{(i)}(10)^{0.0275T}$
3) Sinking Rate (w)	$Sinking = (wX)\frac{\partial X}{\partial z}$ where, X = PS, PL or D
4) Senescence of Small and Large Phytoplankton	$mX = MAX(\min mX, \max mX - (\max mX - \min mX) * \frac{NO_3}{NcritX})$ where X = PhS or PhL
5) Nitrification	$nitr = \left(k_{N_0} \exp(k_{N_T} T)\mathrm{NH}_4\right)\left(\frac{I - I_0}{k_I + I - I_0}\right)$ where I = irradiance at depth (W m^{-2}), I_0 = irradiance of threshold inhibition (W m^{-2}), k_I = irradiance where inhibition is half (W m^{-2}), k_{N_0} = nitrification rate at 0^{o}C (μM d^{-1}), k_{N_T} = temperature correction coefficient for nitrification, T = temperature (^{o}C) and NH_4 = ammonium concentration (μM)
6) Respiration	$R_i = \left(bm_{(i)} e^{\left(k_{tbm(i)} T - T_{ref(i)}\right)}\right) B_i$ where R_i is the respiration rate of species i (mg C m^{-3} d^{-1}), $bm_{(i)}$ = basal metabolism, $k_{tbm(i)}$ = temperature coefficient and $T_{ref(i)}$ = reference temperature (^{o}C) for species i and T = ambient temperature (^{o}C), B_i = biomass of species i, (mg C m^{-3}).
7) Excretion	$E_i = R_i \xi$ where R_i = respiration for species i and ξ = nitrogen carbon ratio
8) C-Chl ratio	$\theta = \frac{\theta_m}{1 + \left(\frac{\theta_m \alpha^{chl} I}{2P_m^C}\right)} = \frac{\theta_m}{1 + \left(\frac{I}{2K_I}\right)}$ where $K_I = \frac{P_m^C}{\alpha^{chl}\theta_m}$ = irradiance at which growth is light saturated; I is the incident radiation in (E m^{-2}) d^{-1}; P_m^C is the light-saturated rate of photosynthesis normalized to carbon, α^{chl} is the initial slope of the PI curve normalized to chlorophyll a (mg C (mg chl)$^{-1}$ (E m^{-2})$^{-1}$) and θ_m is the maximum Chl-C ratio for the phytoplankton components; equations and variables as defined in (Geider et al., 1997)
9) Alpha'	$\alpha' = \frac{\alpha^{chl}}{\theta}$ Where α^{chl} is the initial slope of the PI curves taken from Geider et al. (1997)

Table 2. Parameters for the biological model.

Parameter	Description	Value
dt	Time step (d^{-1}) 1D simulations	0.0093
dt	Time step (d^{-1}) 3D simulations	0.0017
k_{ext}	Extinction coefficient (due to seawater) (m^{-1})	0.080
k_p	Extinction coefficient (due to phytoplankton) (m^{-1})	0.045
DiS	Doubling rate parameter for PS	0.849
DiL	Doubling rate parameter for PL	1.55
DpS	Doubling rate exponent for PS	0.0275
DpL	Doubling rate exponent for PL	0.0275
ξ	Nitrogen:carbon ratio (mmol N/mg C)	0.0126
α_{PS}^{chl}	Slope of P-I curve for PS (g C/g chl-a/µM photons)	0.83e-5
$\theta_{m_{PhS}}$	Maximum Chl-C ratio for PS	0.024
$P_{C_{PhS}}^{M}$	Light saturated photosynthetic rate normalized to C for small phytoplankton (s^{-1})	2.24e-5
d_{fePS}	Half-saturation constant for iron limitation by PS (µmol Fe/m^3)	0.8
Ψ_{PS}	Coefficient of NO_3 limitation for PS	3.0
d_{1PS}	Half-saturation constant for NO_3 limitation for PS (mmol N/ m^3)	0.8
d_{2PS}	Half-saturation constant for NH_4 limitation for PS (mmol N/ m^3)	0.2
α_{PL}^{chl}	Slope of P-I curve for PL (g C/g chl-a/µM photons)	0.58e-5
$\theta_{m_{PhL}}$	Maximum Chl-C ratio for PS	0.0555
$P_{C_{PhL}}^{M}$	Light saturated photosynthetic rate normalized to C for small phytoplankton (s^{-1})	3.27e-5
d_{fePL}	Half-saturation constant for iron limitation for PL ((µmol Fe/m^3))	1.8
Ψ_{PL}	Coefficient of NO_3 limitation for PL	0.3
d_{1PL}	Half-saturation constant for NO_3 limitation for PL (mmol N/ m^3)	0.5
d_{2PL}	Half-saturation constant for NH_4 limitation for PL (mmol N/ m^3)	0.8
e_{MZS}	MZS maximum specific ingestion rate (mg C/mg C/d)	2.0
e_{MZL}	MZL maximum specific ingestion rate (mg C/mg C/d)	5.0
e_C	C maximum specific ingestion rate (mg C/mg C/d)	0.5
e_{NC}	NC maximum specific ingestion rate (mg C/mg C/d)	0.5
e_{Eup}	Eup maximum specific ingestion rate (mg C/mg C/d)	0.234
Q_{10MZS}	Q_{10} for MZS growth rate	2.3
Q_{10MZL}	Q_{10} for MZL growth rate	2.0
Q_{10C}	Q_{10} for C growth rate	1.37

Parameter	Description	Value
Q_{10NC}	Q_{10} for NC growth rate	1.75
Q_{10Eup}	Q_{10} for Eup growth rate	2.25
Q_{10MZST}	Temperature coefficient for Q_{10} for MZS growth rate (°C)	5.0
Q_{10MZLT}	Temperature coefficient for Q_{10} for MZL growth rate (°C)	5.0
Q_{10CT}	Temperature coefficient for Q_{10} for C growth rate (°C)	5.0
Q_{10NCT}	Temperature coefficient for Q_{10} for NC growth rate (°C)	5.0
Q_{10EupT}	Temperature coefficient for Q_{10} for Eup growth rate (°C)	8.0
f_{MZS}	Half-saturation constant for MZS grazing (mg C m^{-3})	20.0
f_{MZL}	Half-saturation constant for MZL grazing (mg C m^{-3})	40.0
f_C	Half-saturation constant for C grazing (mg C m^{-3})	40.4
f_{NC}	Half-saturation constant for NC grazing (mg C m^{-3})	55.0
f_{Eup}	Half-saturation constant for Eup grazing (mg C m^{-3})	45.0
fp_{PSMZS}	Feeding preference of MZS for PS	1.0
fp_{PLMZL}	Feeding preference of MZL for PL	1.0
fp_{PSMZL}	Feeding preference of MZL for PS	1.0
fp_{MZSMZL}	Feeding preference of MZL for MZS	1.0
fp_{PSC}	Feeding preference of C for PS	0.5
fp_{PLC}	Feeding preference of C for PL	1.0
fp_{MZSC}	Feeding preference of C for MZS	0.5
fp_{MZLC}	Feeding preference of C for MZL	1.0
fp_{PSNC}	Feeding preference of NC for PS	0.5
fp_{PLNC}	Feeding preference of NC for PL	1.0
fp_{MZSNC}	Feeding preference of NC for MZS	0.5
fp_{MZLNC}	Feeding preference of NC for MZL	1.0
fp_{PLEup}	Feeding preference of Eup for PL	1.0
fp_{MZLEup}	Feeding preference of Eup for MZL	0.5
fp_{CEup}	Feeding preference of EUP for C	0.5
mPS_{min}	Minimum daily linear mortality rate for PS (d^{-1})	0.01
mPS_{max}	Maximum daily linear mortality rate for PS (d^{-1})	0.085
NO_{critPS}	Critical NO_3 for PS mortality (mg C/m^{-3})	0.6
mPL_{min}	Minimum daily (linear) mortality rate for PL (d^{-1})	0.01
mPL_{max}	Maximum daily (linear) mortality rate for PL (d^{-1})	0.085
NO_{critPL}	Critical NO_3 for PL mortality (mg C/m^{-3})	0.6
$mpred_{MZS}$	Daily (nonlinear) mortality for MZS (d^{-1})	0.001
$mpred_{MZL}$	Daily (nonlinear) mortality for MZL (d^{-1})	0.001
$mpred_C$	Daily (nonlinear) mortality for C (d^{-1})	0.00075
$mpred_{NC}$	Daily (nonlinear) mortality for NC (d^{-1})	0.00075
γ_{MZS}	Growth efficiency for MZS	0.7
γ_{MZL}	Growth efficiency for MZL	0.7
γ_C	Growth efficiency for C	0.7
γ_{NC}	Growth efficiency for NC	0.7
wPS	Sinking rate for PS (m/s)	0.0
$respPS$	Basal metabolic rate (d^{-1}) for PS	0.08
$respPL$	Basal metabolic rate (d^{-1}) for PL	0.1
$respMZS$	Basal metabolic rate (d^{-1}) for MZS	0.6

Parameter	Description	Value
respMZL	Basal metabolic rate (d^{-1}) for MZL	1.4
respC	Basal metabolic rate (d^{-1}) for C	0.03
respN	Basal metabolic rate (d^{-1}) for N	0.03
respEup	Basal metabolic rate (d^{-1}) for Eup	0.02
wPL	Sinking rate for PL (m/s)	0.1
wD	Sinking rate for D (m/s)	5.0
regen	Regeneration rate for ammonium	0.4
degrad	Degradation rate for detritus	0.10
ccr_{PS}	Carbon-to-Chlorophyll Ratio for PS (mg C/mg Chl)	40.0
ccr_{PL}	Carbon-to-Chlorophyll Ratio for PL (mg C/mg Chl)	20.0
f_{ec}	Iron to Carbon Ratio (nmol Fe/mg C)	1.667d-4

Fig. 1

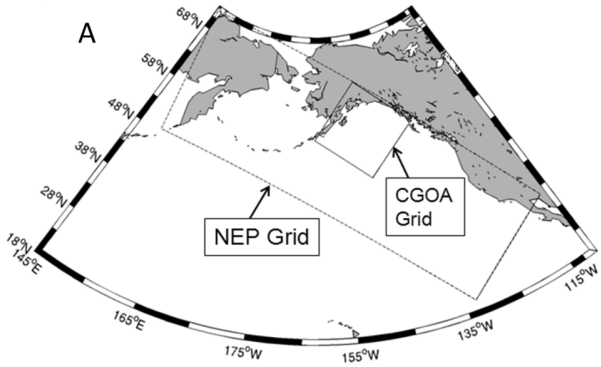
A
68°N
58°N
48°N
38°N
28°N
18°N
145°E
165°E
175°W
155°W
135°W
115°W
CGOA Grid
NEP Grid

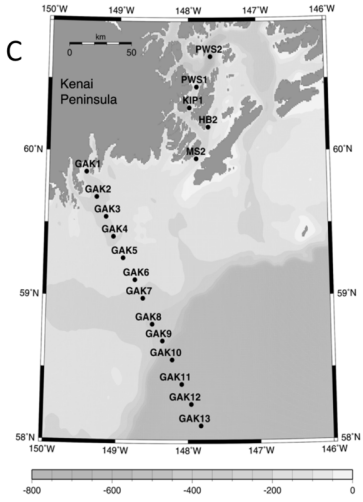
C
150°W
149°W
148°W
147°W
146°W
km
0
50
Kenai Peninsula
PWS2
PWS1
KIP1
HB2
MS2
GAK1
GAK2
GAK3
GAK4
GAK5
GAK6
GAK7
GAK8
GAK9
GAK10
GAK11
GAK12
GAK13
60°N
59°N
58°N
-800
-600
-400
-200
0

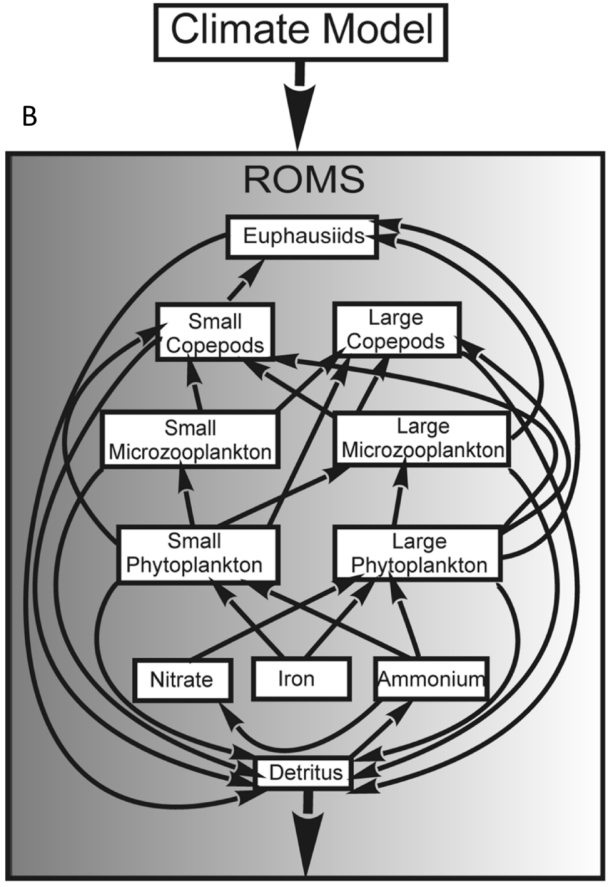
Climate Model
B
ROMS
Euphausiids
Small Copepods
Large Copepods
Small Microzooplankton
Large Microzooplankton
Small Phytoplankton
Large Phytoplankton
Nitrate
Iron
Ammonium
Detritus

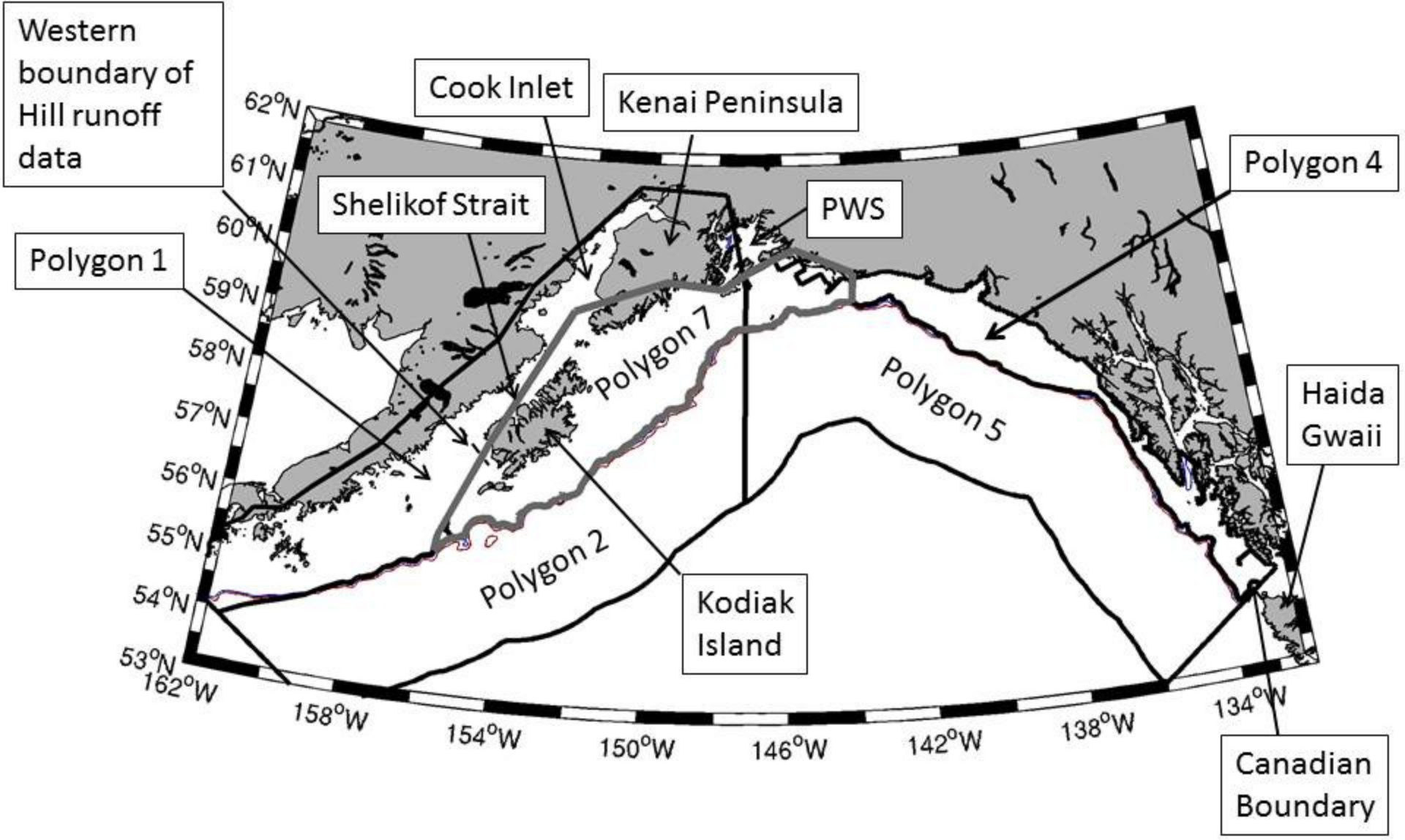
Western boundary of Hill runoff data
Cook Inlet
Kenai Peninsula
Polygon 4
Shelikof Strait
PWS
Polygon 1
Polygon 7
Polygon 5
Haida Gwaii
Polygon 2
Kodiak Island
Canadian Boundary
62°N
61°N
60°N
59°N
58°N
57°N
56°N
55°N
54°N
53°N
162°W
158°W
154°W
150°W
146°W
142°W
138°W
134°W

Fig 2.

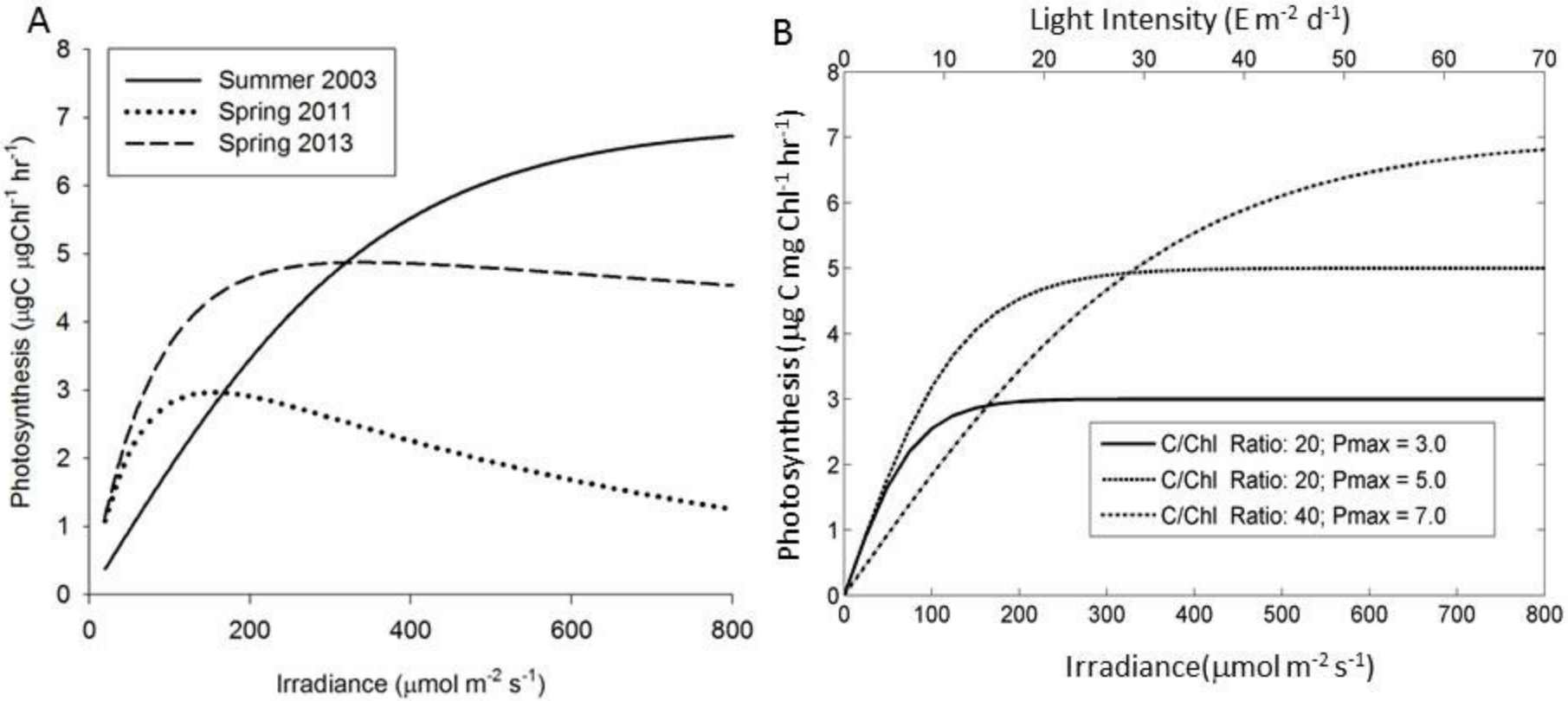
A
Summer 2003
Spring 2011
Spring 2013
Photosynthesis (μgC μgChl-1 hr-1)
Irradiance (μmol m-2 s-1)
B
Light Intensity (E m-2 d-1)
Photosynthesis (μg C mg Chl-1 hr-1)
C/Chl Ratio: 20; Pmax = 3.0
C/Chl Ratio: 20; Pmax = 5.0
C/Chl Ratio: 40; Pmax = 7.0
Irradiance(μmol m-2 s-1)

Fig. 3

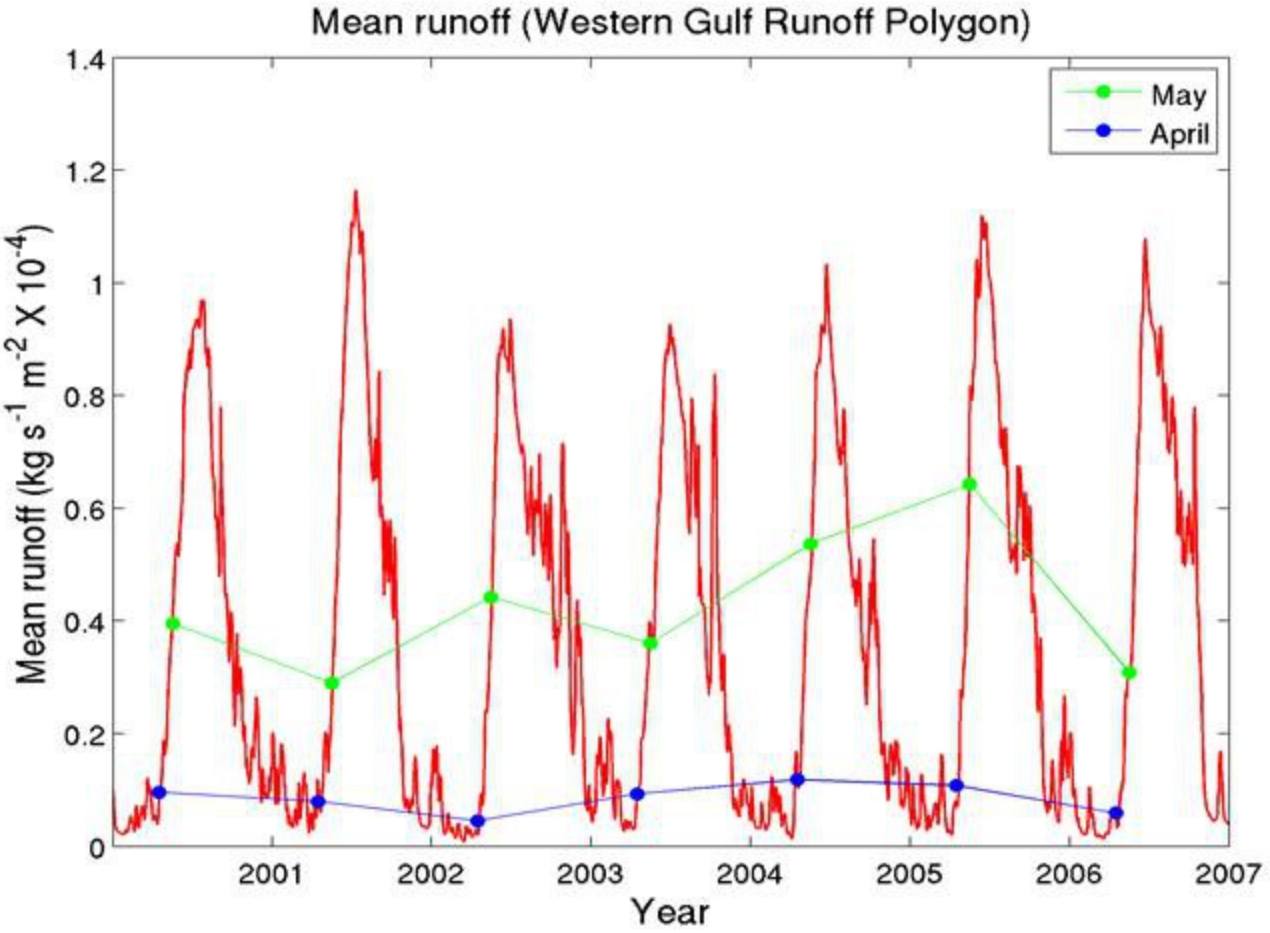
Mean runoff (Western Gulf Runoff Polygon)
May
April
Mean runoff (kg s-1 m-2 X 10-4)
Year
0
0.2
0.4
0.6
0.8
1
1.2
1.4
2001
2002
2003
2004
2005
2006
2007

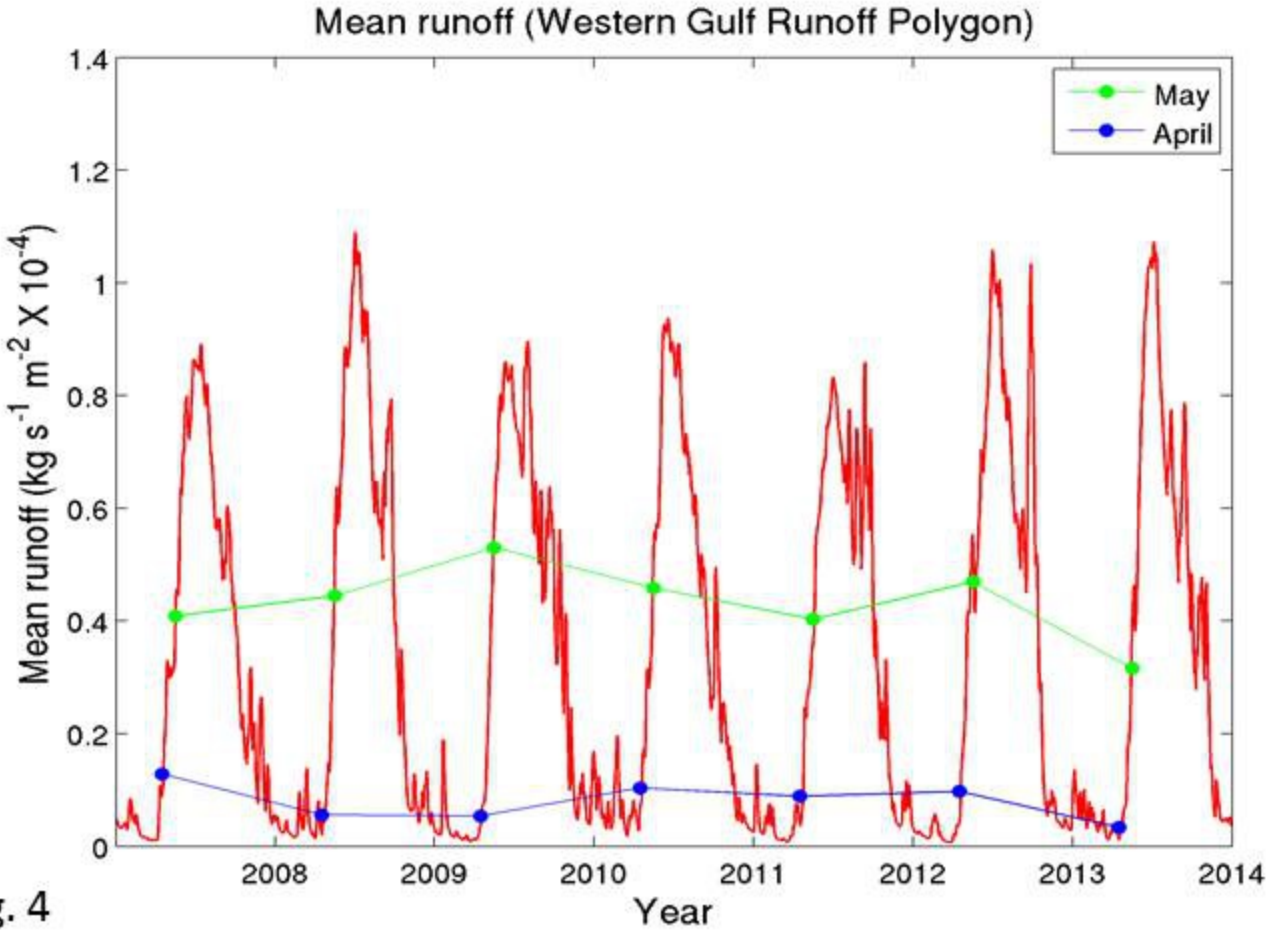
Mean runoff (Western Gulf Runoff Polygon)
May
April
Mean runoff (kg s-1 m-2 X 10-4)
Year
0
0.2
0.4
0.6
0.8
1
1.2
1.4
2008
2009
2010
2011
2012
2013
2014

Fig. 4

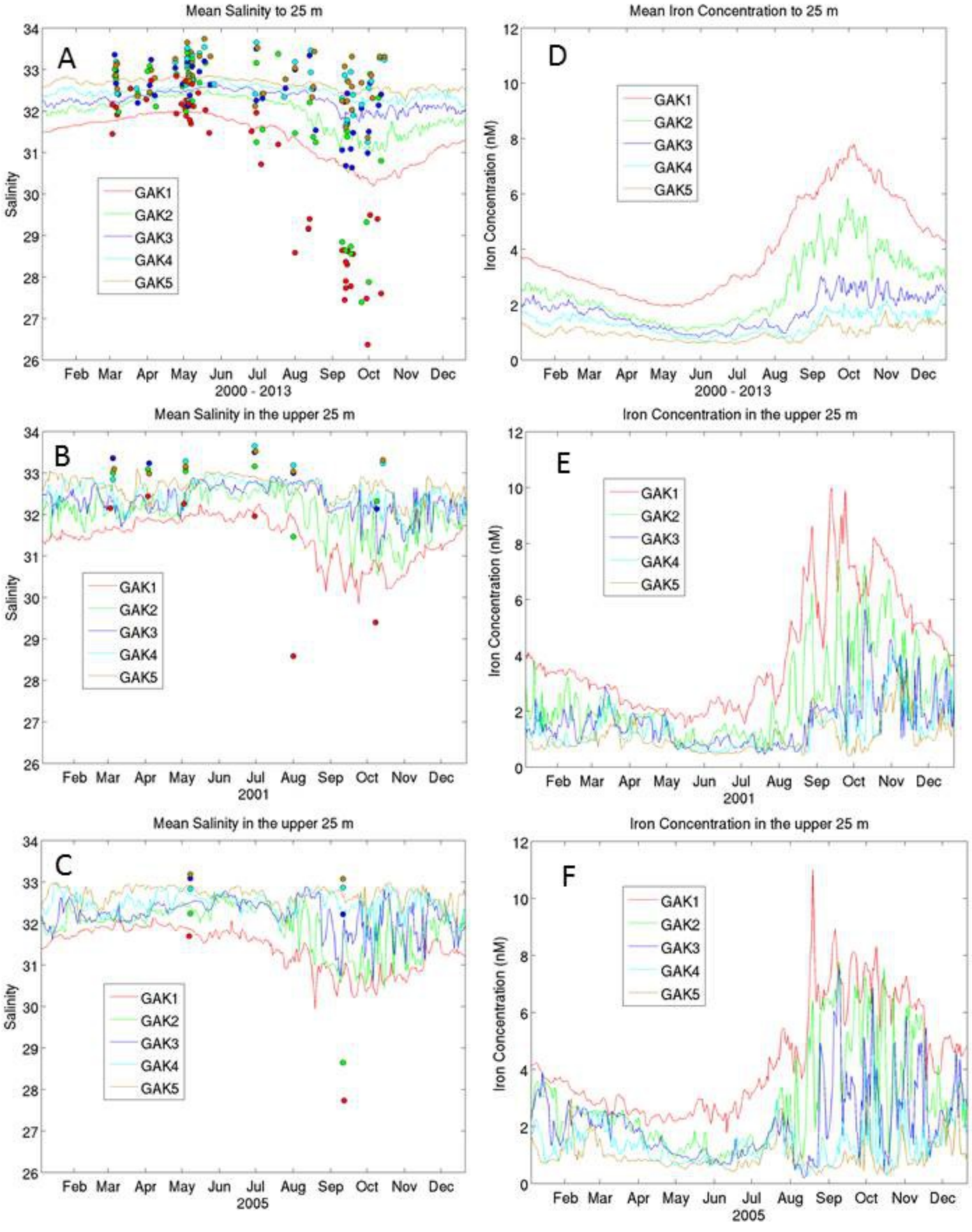
Mean Salinity to 25 m
A
Salinity
GAK1
GAK2
GAK3
GAK4
GAK5
Feb Mar Apr May Jun Jul Aug Sep Oct Nov Dec
2000 - 2013
Mean Iron Concentration to 25 m
D
Iron Concentration (nM)
2000 - 2013
Mean Salinity in the upper 25 m
B
2001
Iron Concentration in the upper 25 m
E
2001
Mean Salinity in the upper 25 m
C
2005
Iron Concentration in the upper 25 m
F
2005

Fig. 5

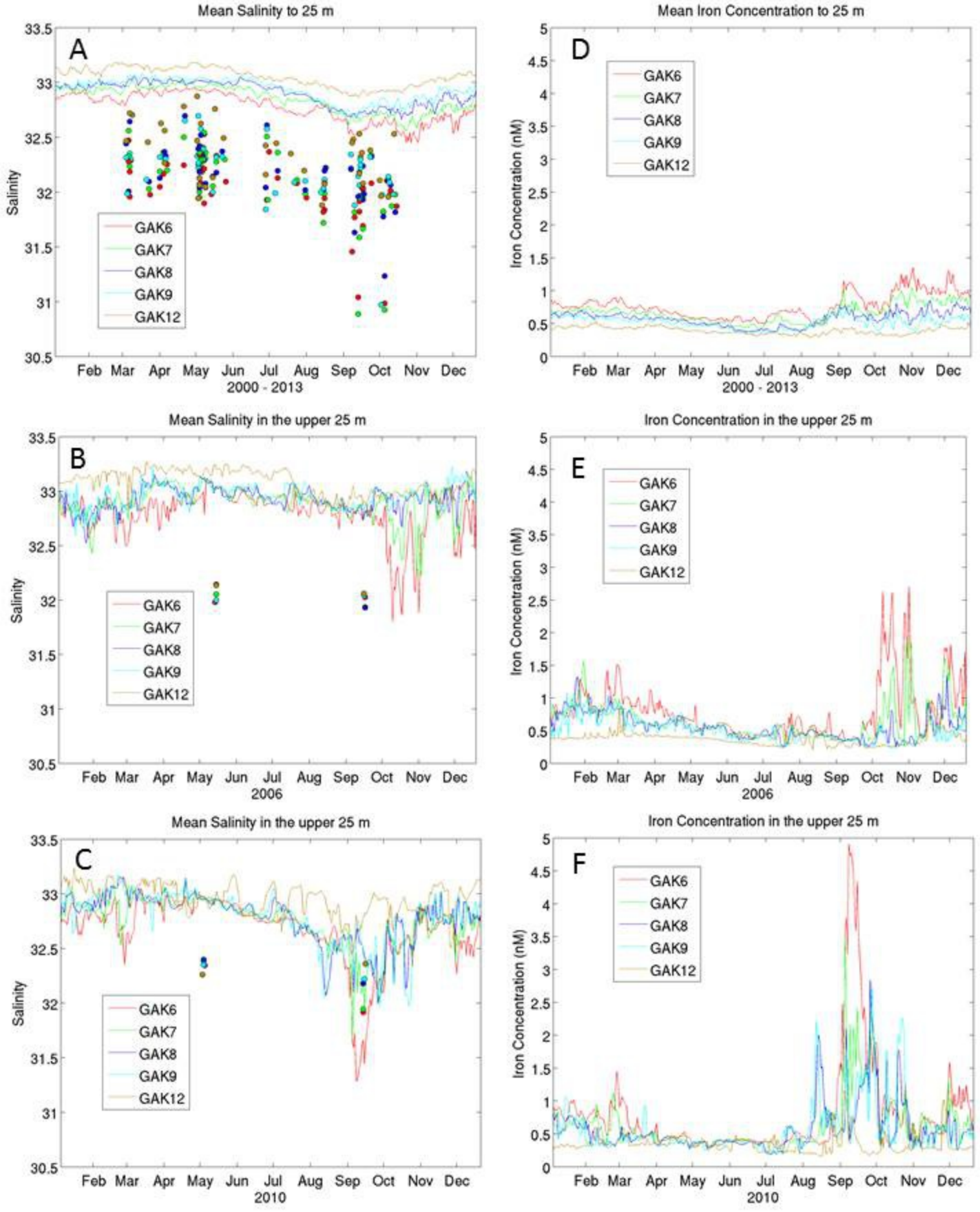
Mean Salinity to 25 m
A
Salinity
GAK6
GAK7
GAK8
GAK9
GAK12
Feb Mar Apr May Jun Jul Aug Sep Oct Nov Dec
2000 - 2013
Mean Iron Concentration to 25 m
D
Iron Concentration (nM)
Mean Salinity in the upper 25 m
B
2006
Iron Concentration in the upper 25 m
E
Mean Salinity in the upper 25 m
C
2010
Iron Concentration in the upper 25 m
F

Fig. 6

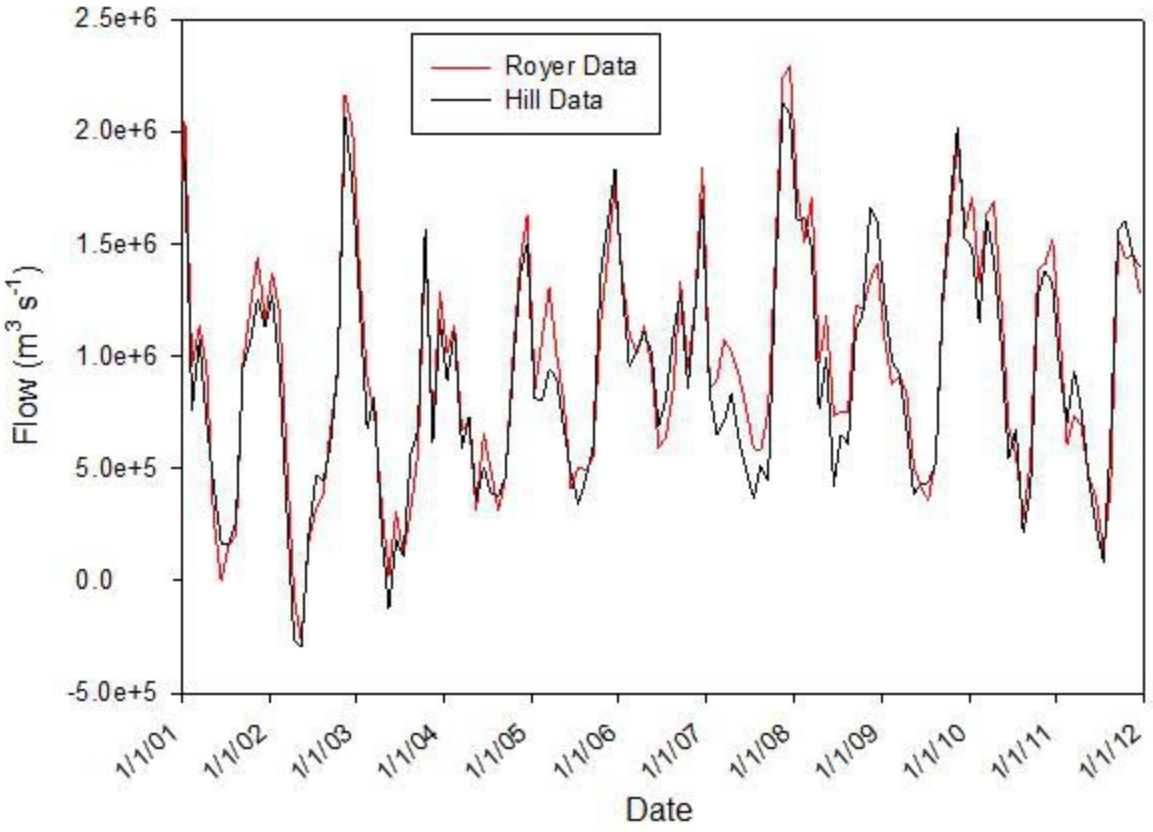
Royer Data
Hill Data
2.5e+6
2.0e+6
1.5e+6
1.0e+6
5.0e+5
0.0
-5.0e+5
Flow (m3 s-1)
1/1/01
1/1/02
1/1/03
1/1/04
1/1/05
1/1/06
1/1/07
1/1/08
1/1/09
1/1/10
1/1/11
1/1/12
Date

Fig. 7.

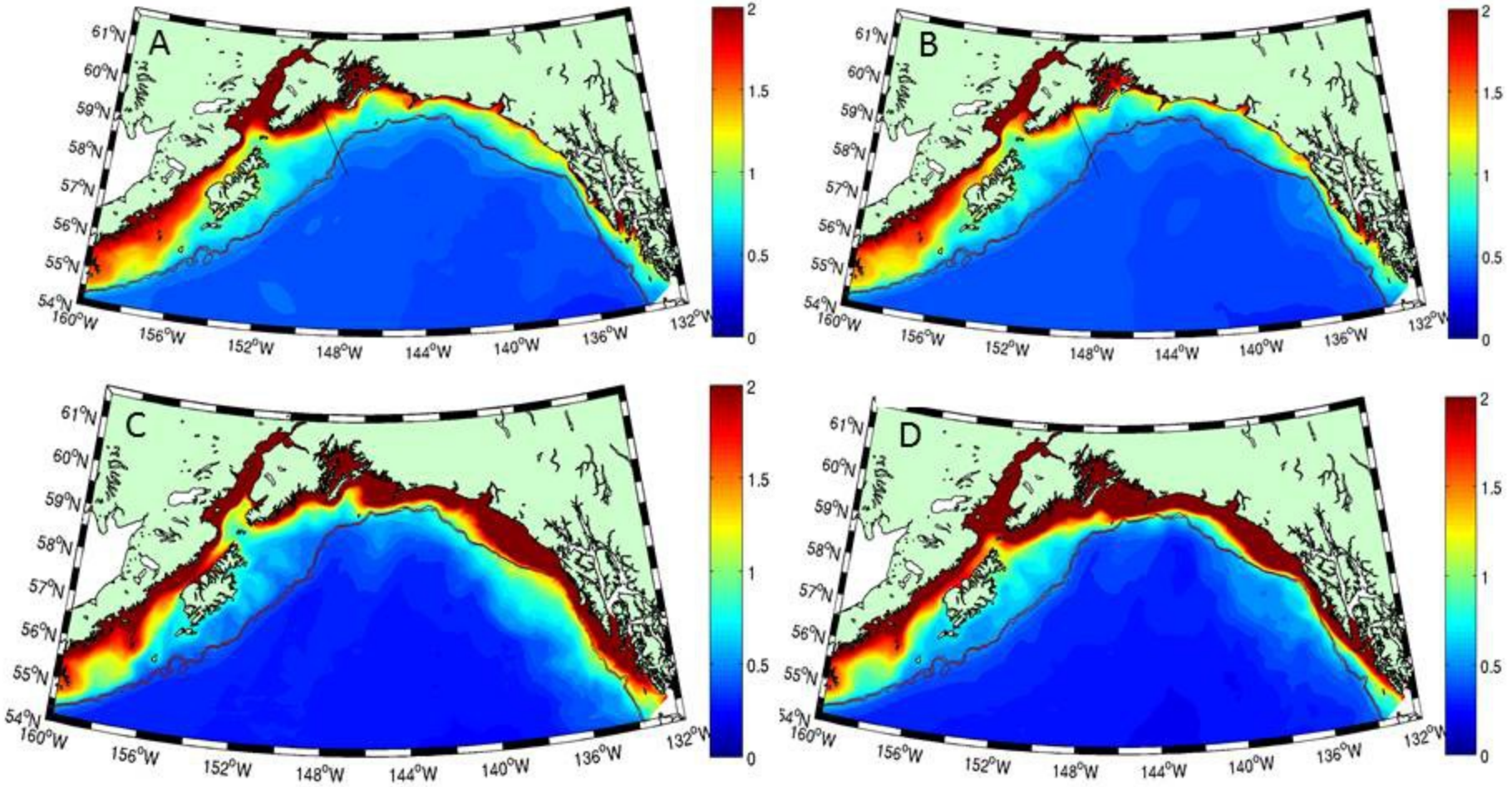
A
B
C
D
61°N
60°N
59°N
58°N
57°N
56°N
55°N
54°N
160°W
156°W
152°W
148°W
144°W
140°W
136°W
132°W
2
1.5
1
0.5
0

Fig. 8

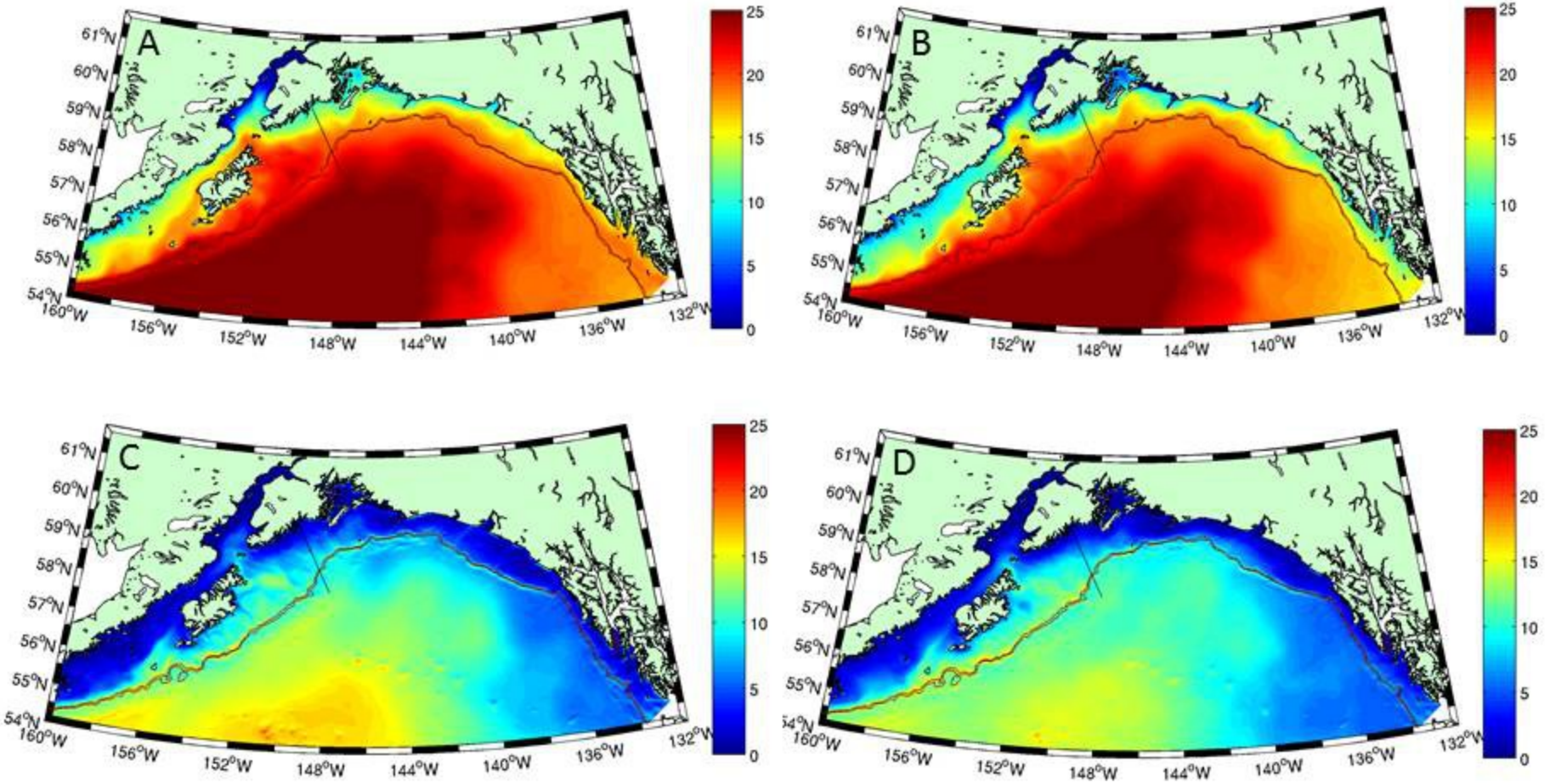
A
B
C
D
61°N
60°N
59°N
58°N
57°N
56°N
55°N
54°N
160°W
156°W
152°W
148°W
144°W
140°W
136°W
132°W
25
20
15
10
5
0

Fig. 9.

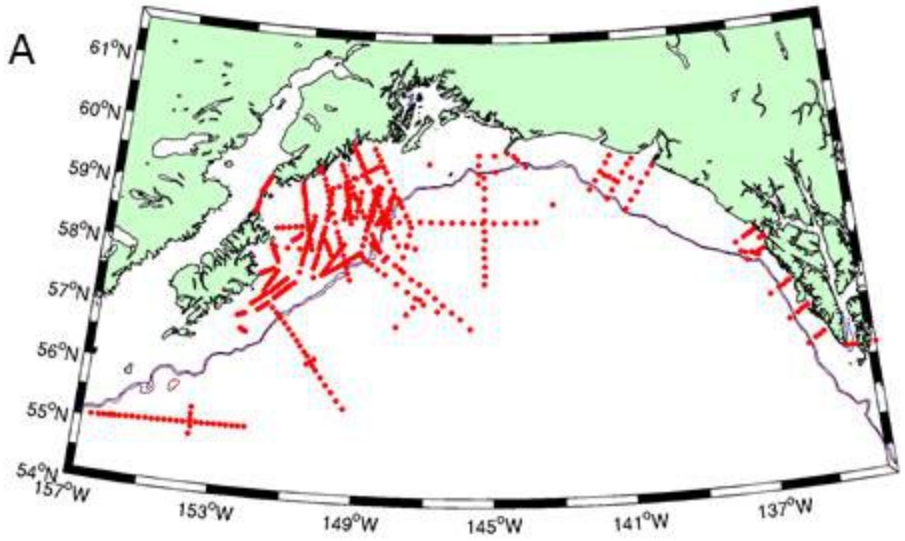
A
61°N
60°N
59°N
58°N
57°N
56°N
55°N
54°N
157°W
153°W
149°W
145°W
141°W
137°W

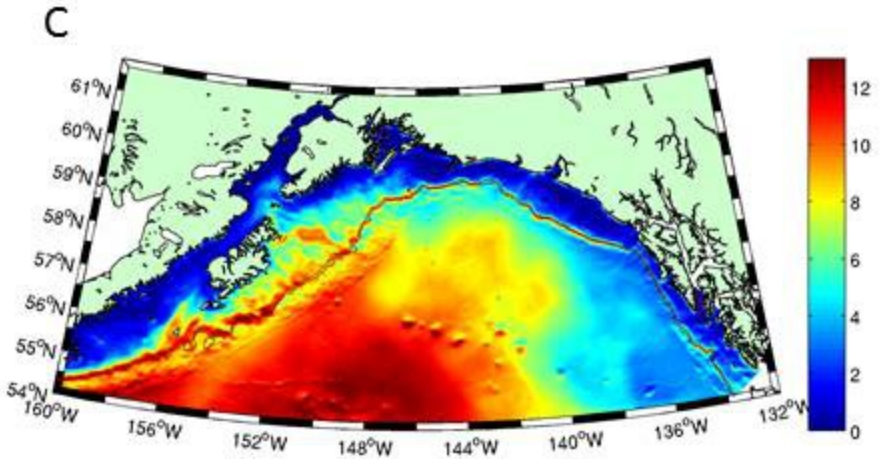
C
61°N
60°N
59°N
58°N
57°N
56°N
55°N
54°N
160°W
156°W
152°W
148°W
144°W
140°W
136°W
132°W
12
10
8
6
4
2
0

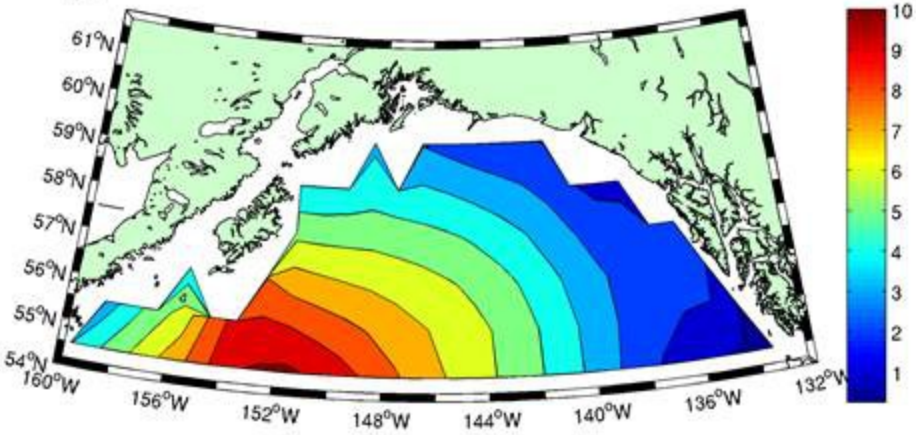
D
61°N
60°N
59°N
58°N
57°N
56°N
55°N
54°N
160°W
156°W
152°W
148°W
144°W
140°W
136°W
132°W
10
9
8
7
6
5
4
3
2
1

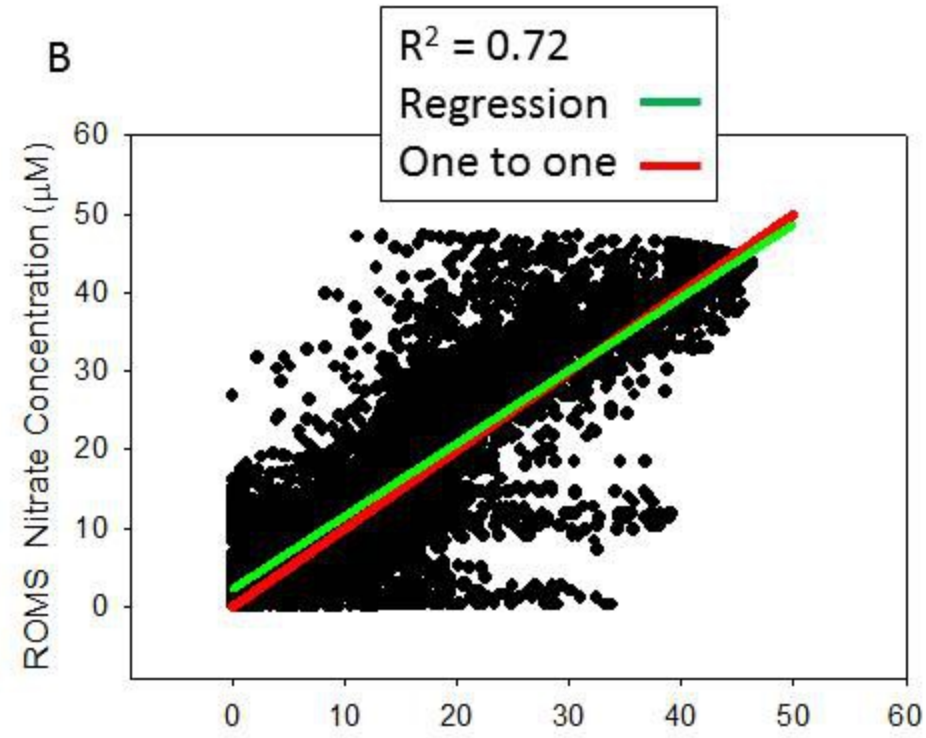
B
R² = 0.72
Regression
One to one
ROMS Nitrate Concentration (μM)
FOCI Nitrate Concentration (μM)
0
10
20
30
40
50
60

Fig. 10

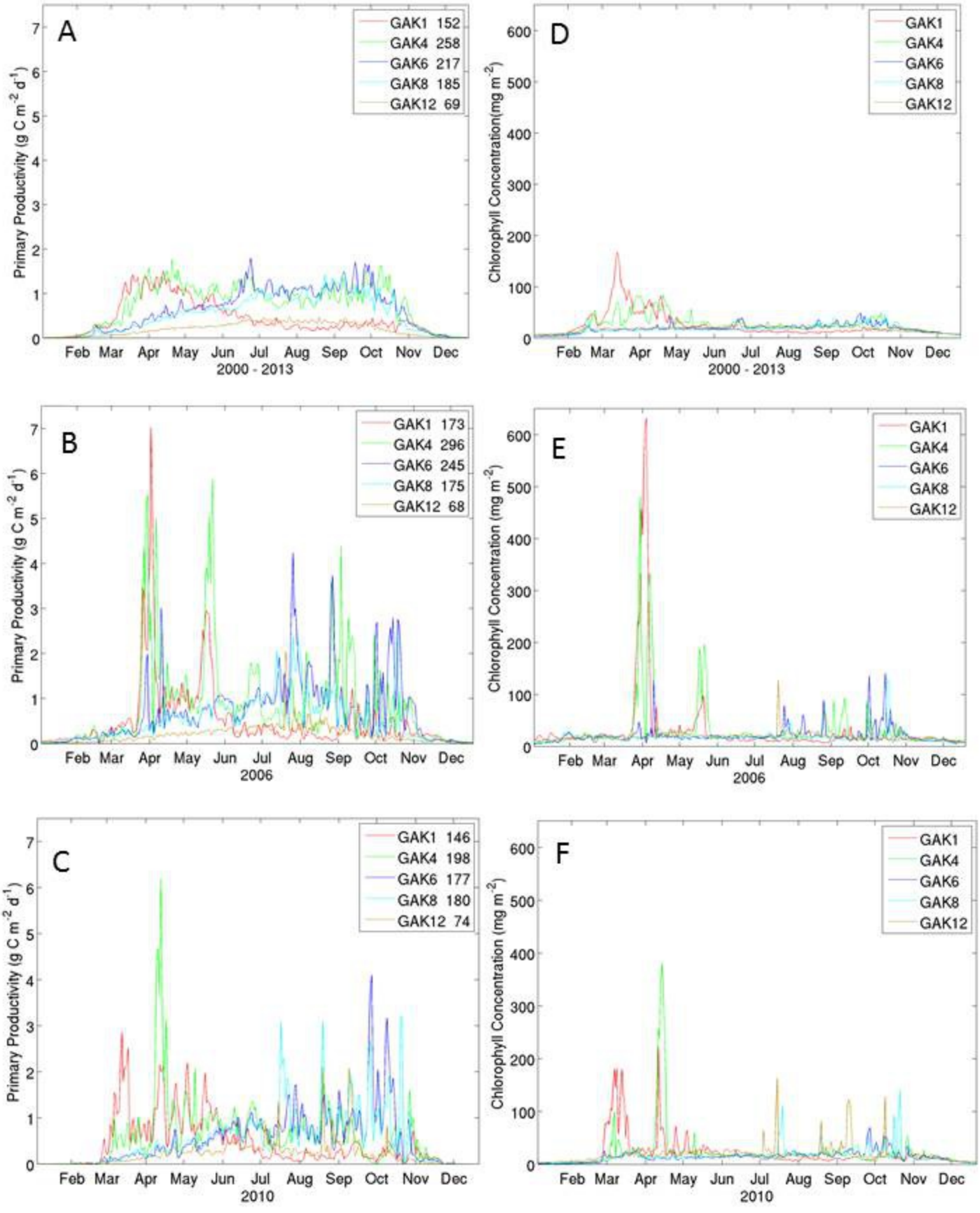
A
GAK1 152
GAK4 258
GAK6 217
GAK8 185
GAK12 69
Primary Productivity (g C m-2 d-1)
Feb Mar Apr May Jun Jul Aug Sep Oct Nov Dec
2000 - 2013
D
GAK1
GAK4
GAK6
GAK8
GAK12
Chlorophyll Concentration(mg m-2)
Feb Mar Apr May Jun Jul Aug Sep Oct Nov Dec
2000 - 2013
B
GAK1 173
GAK4 296
GAK6 245
GAK8 175
GAK12 68
Primary Productivity (g C m-2 d-1)
Feb Mar Apr May Jun Jul Aug Sep Oct Nov Dec
2006
E
GAK1
GAK4
GAK6
GAK8
GAK12
Chlorophyll Concentration (mg m-2)
Feb Mar Apr May Jun Jul Aug Sep Oct Nov Dec
2006
C
GAK1 146
GAK4 198
GAK6 177
GAK8 180
GAK12 74
Primary Productivity (g C m-2 d-1)
Feb Mar Apr May Jun Jul Aug Sep Oct Nov Dec
2010
F
GAK1
GAK4
GAK6
GAK8
GAK12
Chlorophyll Concentration (mg m-2)
Feb Mar Apr May Jun Jul Aug Sep Oct Nov Dec
2010

Fig. 11

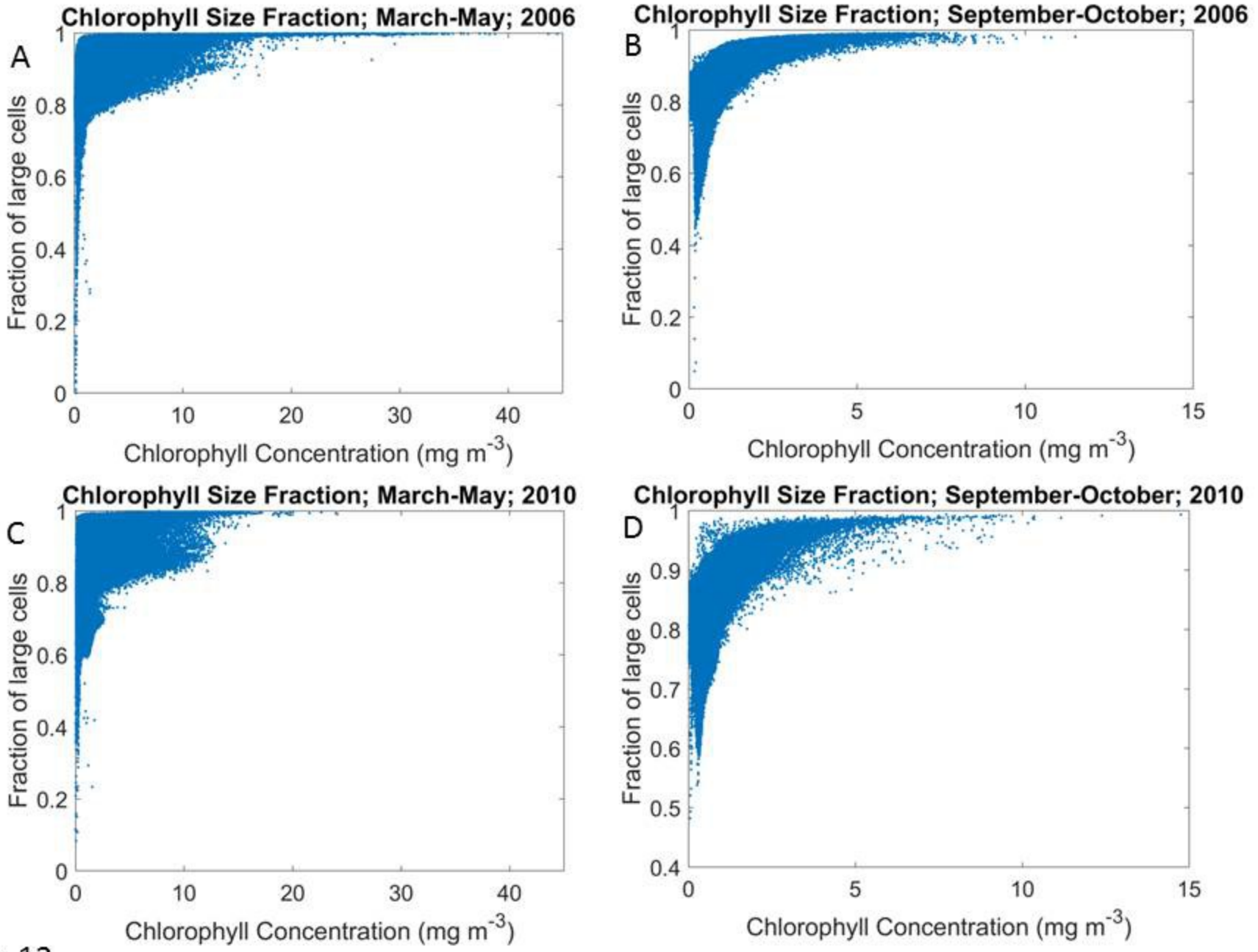
Chlorophyll Size Fraction; March-May; 2006
A
Fraction of large cells
Chlorophyll Concentration (mg m-3)
Chlorophyll Size Fraction; September-October; 2006
B
Fraction of large cells
Chlorophyll Concentration (mg m-3)
Chlorophyll Size Fraction; March-May; 2010
C
Fraction of large cells
Chlorophyll Concentration (mg m-3)
Chlorophyll Size Fraction; September-October; 2010
D
Fraction of large cells
Chlorophyll Concentration (mg m-3)

Fig. 12

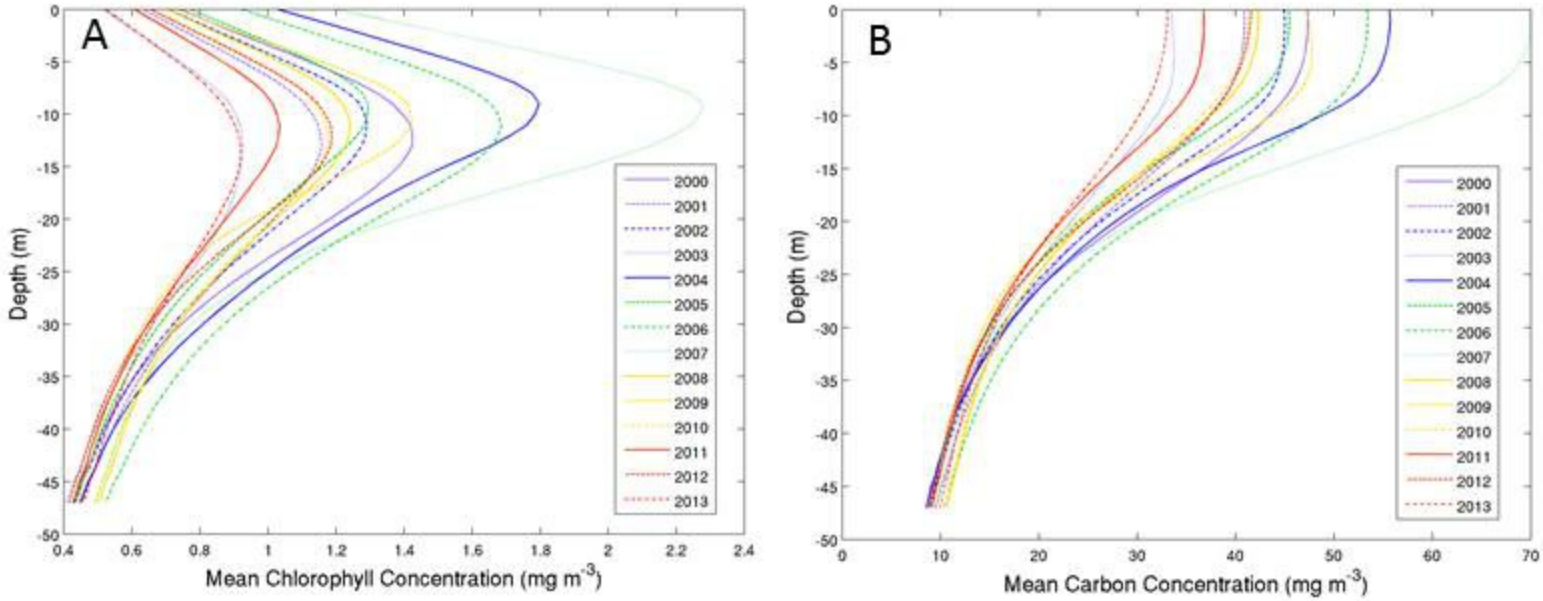
A
B
Depth (m)
Mean Chlorophyll Concentration (mg m-3)
Mean Carbon Concentration (mg m-3)
2000
2001
2002
2003
2004
2005
2006
2007
2008
2009
2010
2011
2012
2013

Fig. 13

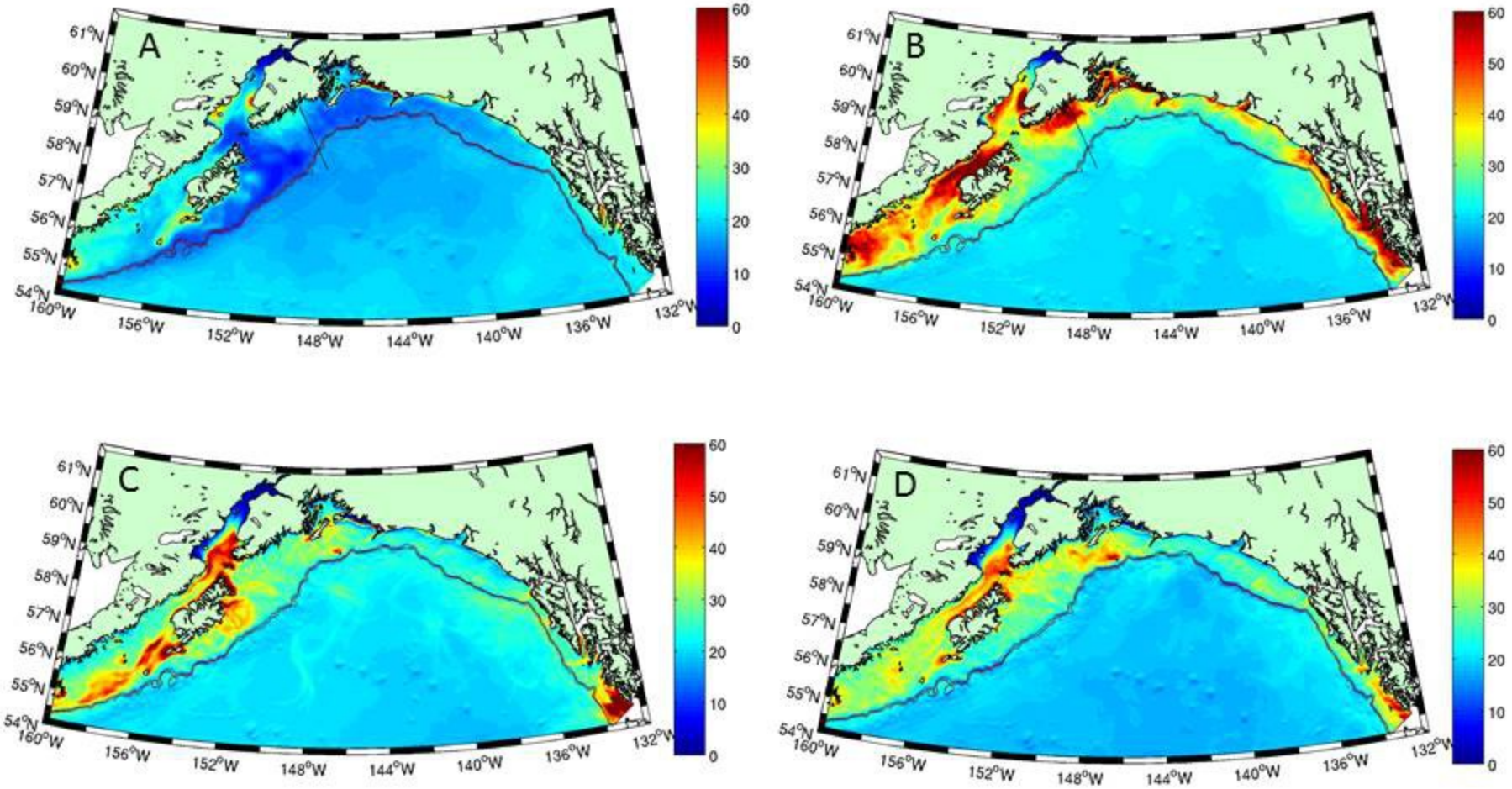
A
B
C
D
61°N
60°N
59°N
58°N
57°N
56°N
55°N
54°N
160°W
156°W
152°W
148°W
144°W
140°W
136°W
132°W
60
50
40
30
20
10
0

Fig. 14

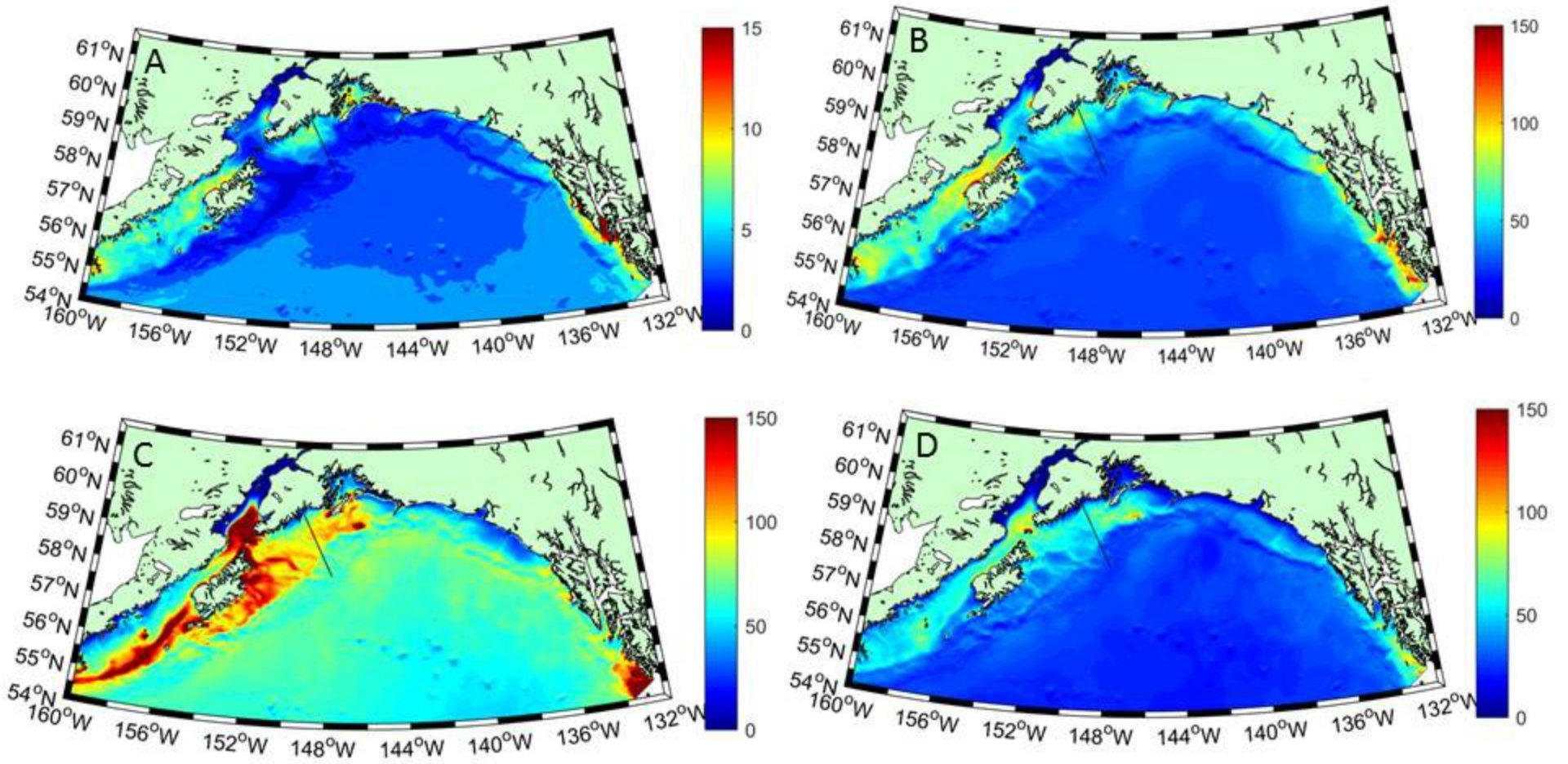
A
B
C
D
61°N
60°N
59°N
58°N
57°N
56°N
55°N
54°N
160°W
156°W
152°W
148°W
144°W
140°W
136°W
132°W
15
10
5
0
150
100
50
0

Fig. 15

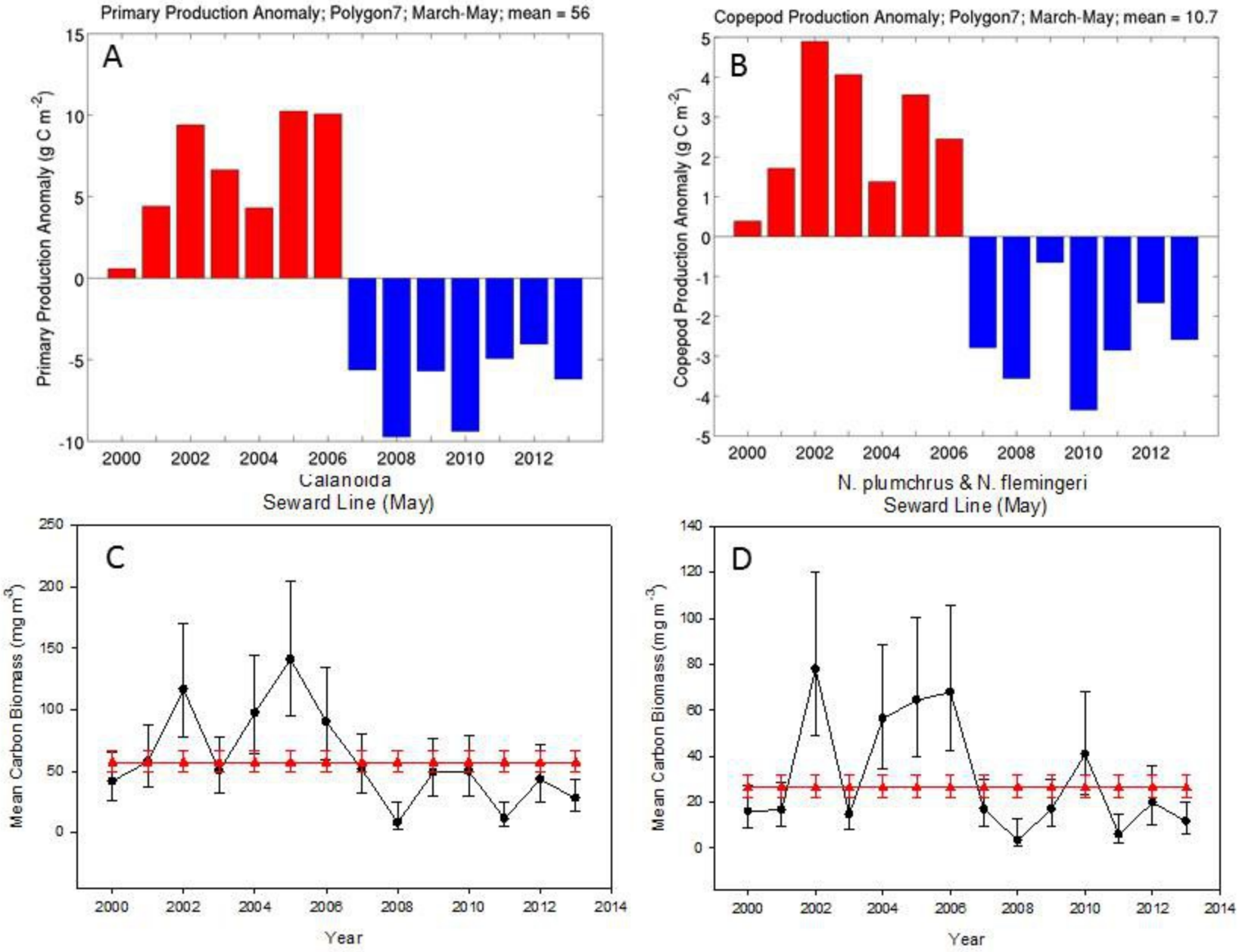
Primary Production Anomaly; Polygon7; March-May; mean = 56
A
Primary Production Anomaly (g C m-2)
15
10
5
0
-5
-10
2000
2002
2004
2006
2008
2010
2012
Calanoida
Seward Line (May)
Copepod Production Anomaly; Polygon7; March-May; mean = 10.7
B
Copepod Production Anomaly (g C m-2)
5
4
3
2
1
0
-1
-2
-3
-4
-5
N. plumchrus & N. flemingeri
Seward Line (May)
C
Mean Carbon Biomass (mg m-3)
250
200
150
100
50
0
Year
D
140
120
100
80
60
40
20
2014

Fig. 16

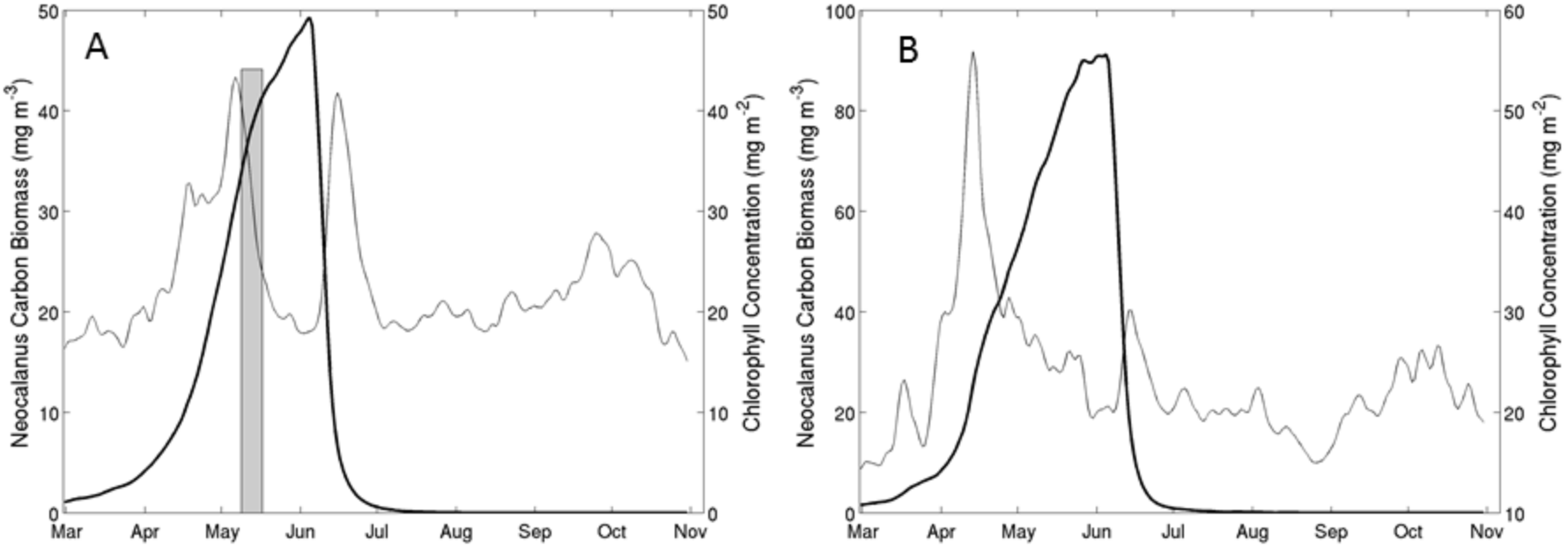
A
B
Neocalanus Carbon Biomass (mg m-3)
Chlorophyll Concentration (mg m-2)
Mar
Apr
May
Jun
Jul
Aug
Sep
Oct
Nov

Fig. 17

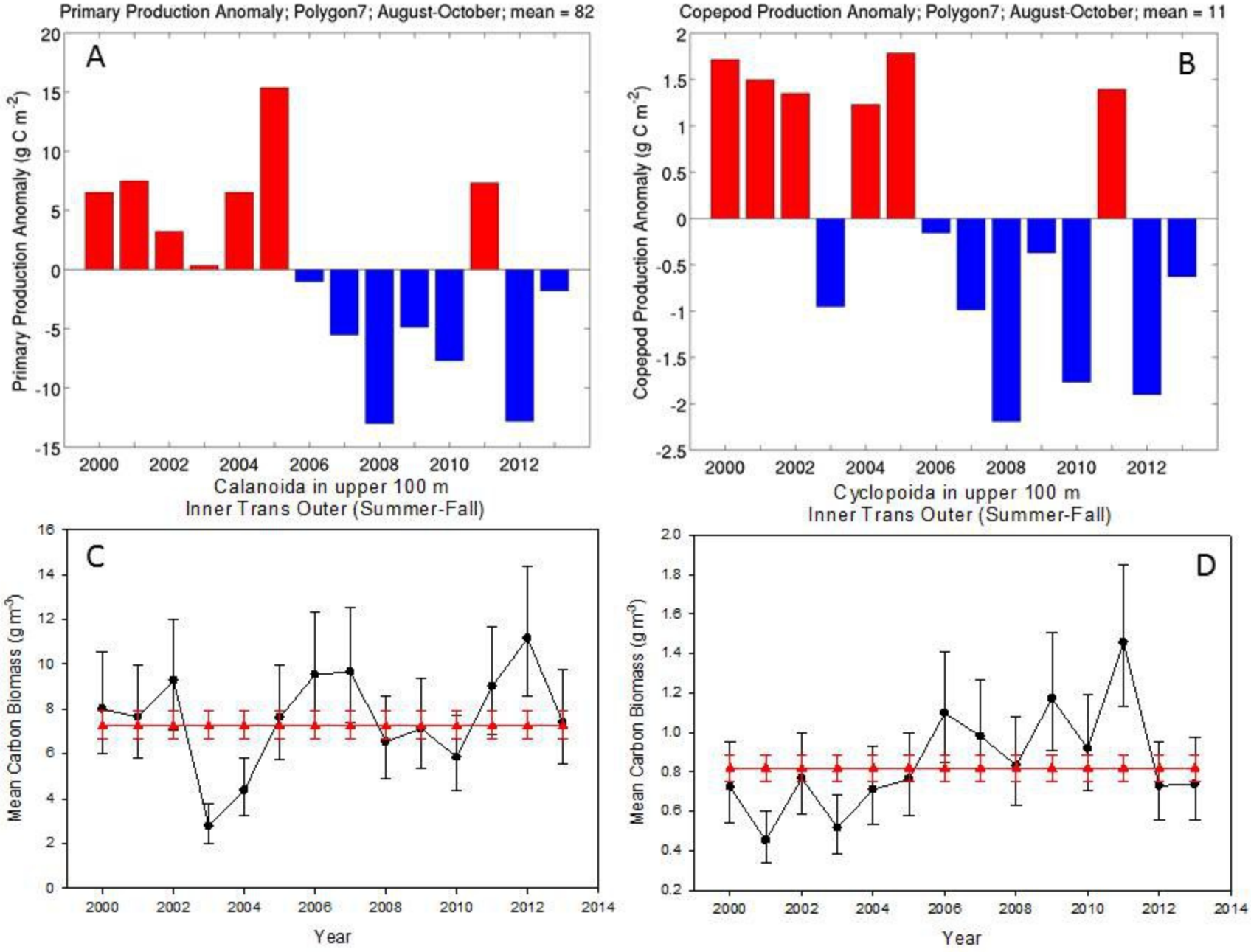
Primary Production Anomaly; Polygon7; August-October; mean = 82
A
Primary Production Anomaly (g C m-2)
Calanoida in upper 100 m
Inner Trans Outer (Summer-Fall)
Copepod Production Anomaly; Polygon7; August-October; mean = 11
B
Copepod Production Anomaly (g C m-2)
Cyclopoida in upper 100 m
Inner Trans Outer (Summer-Fall)
C
Mean Carbon Biomass (g m-3)
Year
D
Mean Carbon Biomass (g m-3)
Year

Fig. 18